Distribution Agreement

In presenting this thesis or dissertation as a partial fulfillment of the requirements for an advanced degree from Emory University, I hereby grant to Emory University and its agents the non-exclusive license to archive, make accessible, and display my thesis or dissertation in whole or in part in all forms of media, now or hereafter known, including display on the world wide web. I understand that I may select some access restrictions as part of the online submission of this thesis or dissertation. I retain all ownership rights to the copyright of the thesis or dissertation. I also retain the right to use in future works (such as articles or books) all or part of this thesis or dissertation.

Signature:

______________________________ _______________

Damon Lamb Date

Correlated Conductance Parameters in Leech Heart Motor Neurons Contribute to Motor Pattern Formation

By
Damon G. Lamb
Doctor of Philosophy

Graduate Division of Biological and Biomedical Sciences
Neuroscience
James T. Laney Graduate School

____
Ronald L. Calabrese
Advisor

____
Robert J. Butera
Committee Member

____
Dieter Jaeger
Committee Member

____
Astrid A. Prinz
Committee Member

____
Donald Rainnie
Committee Member

Accepted:
____
Lisa A. Tedesco, Ph.D.
Dean of the James T. Laney School of Graduate Studies

____________________ Date

Correlated Conductance Parameters in Leech Heart Motor Neurons Contribute to Motor Pattern Formation

By

Damon G. Lamb
M.S., University of Chicago 2005
B.S., University of Maryland, College Park 2003
B.S., University of Maryland, College Park 2003

Advisor: Ronald L. Calabrese

An abstract of
A dissertation submitted to the Faculty of the
James T. Laney School of Graduate Studies of Emory University
in partial fulfillment of the requirements for the degree of
Doctor of Philosophy in Neuroscience
2013

Abstract

Neurons can have widely differing intrinsic membrane properties, in particular the density of specific ionic conductances, but how these contribute to intrinsic neural properties and characteristic neuronal activity or pattern formation is not well understood. To explore the relationships between conductances, and in particular how they influence the activity of motor neurons in the well characterized leech heartbeat system, we developed a new multi-compartmental Hodgkin-Huxley style leech heart motor neuron model. To do so, we evolved a population of model instances, which differed in the density of specific conductances, capable of achieving specific output activity targets given an associated input pattern. We then examined the sensitivity of measures of output activity to conductances and how the model instances responded to hyperpolarizing current injections. We found that the strengths of many conductances, including those with differing dynamics, had strong partial correlations and that these relationships appeared to be linked by their influence on heart motor neuron activity. Conductances that had positive correlations opposed one another and had the opposite effects on activity metrics when perturbed whereas conductances that had negative correlations could compensate for one another and had similar effects on activity metrics.

Correlated Conductance Parameters in Leech Heart Motor Neurons Contribute to Motor Pattern Formation

By

Damon G. Lamb
M.S., University of Chicago 2005
B.S., University of Maryland, College Park 2003
B.S., University of Maryland, College Park 2003

Advisor: Ronald L. Calabrese

A dissertation submitted to the Faculty of the
James T. Laney School of Graduate Studies of Emory University
in partial fulfillment of the requirements for the degree of
Doctor of Philosophy in Neuroscience
2013

Acknowledgments

Before we get into the juicy core of this thesis, I would like to take a moment to acknowledge and thank the people who made this possible. Although I’d like to list everyone who has contributed support, guidance and advice, the unbearable length of such a list would inevitably bore everyone who actually bothers to read this section. As such, I will be brief. To all my teachers, friends, family, acquaintances, colleagues, and especially mentors who have guided my development and trajectory up until this point, I am most grateful for the time and effort you have given me, the direction you have provided, and for sharing the occasional dram when the night so required.

To you all I am ever indebted.

Let us think the unthinkable,
let us do the undoable.
Let us prepare to grapple with the ineffable itself,
and see if we may not eff it after all.
–Douglas Adams

Table of Contents

Table of Figures

Table of Tables

Chapter 1: General introduction

The brain is a fascinating organ. We ascribe to it the seat of our mind and thus that which is the essence of our self. As is to be expected for something capable of producing multifaceted and diverse thoughts and behaviors, it is staggeringly complicated. Even with the frenetic increases in understanding we have collectively achieved in the past decade, our understanding of the brain is still woefully sparse. In this dissertation we extend our understanding with a bottom-up approach, beginning not quite at the level of individual ion channels or molecules, but individual neurons and a small, well defined and generally tractable class of neuronal networks: central pattern generators (CPGs). These small neuronal networks are capable of producing their characteristic neuronal activity in the absence of sensory input or extrinsic timing information, in particular when isolated and placed *in vitro* (Marder and Calabrese, 1996). The best studied CPGs are those that are found in the stereotyped nervous systems of invertebrates (Marder et al., 2005, Sattelle and Buckingham, 2006, Clarac and Pearlstein, 2007), and in particular those which produce the rhythmic motor patterns that underlie walking, breathing, food processing, swimming, and, in the system we focus on, the medicinal leech (*hirudo*, spp.), heartbeat.

The motor neurons driven by these CPG networks are generally considered followers of the CPG's output, and so less interesting. Indeed, the neural basis of rhythmic pattern formation and coordinated timing between oscillating sub-networks is a fascinating and vibrant research area. Some classes of motor neurons themselves are known to exhibit properties which can influence the patterns they produce. For example, in the mammalian spinal cord certain motor neurons can produce stable motor rhythms through gap junction interconnectivity in the absence of premotor interneuron activity (Tresch and Kiehn, 2000). Also in the mammalian spinal cord, a hyperpolarization-activated inward cation current (I_h) was found to phase-advance activity during rhythmic activity (Kiehn et al., 2000). On the other hand, certain body-wall motor neurons in the leech have been shown to be predominantly under the control of their inputs (Bernardo Perez-Etchegoyen et al., 2012). Intrinsic properties do appear to play an important role in phasing of leech heart (HE) motor neurons, however (Wright and Calabrese, 2011a). The HE motor neurons are electrically coupled within each ganglion, likely through a gap junction synapse—the leech genome codes for many innexin proteins (Kandarian et al., 2012)—but there is no evidence for I_h in them. Previous leech heart motor neuron modeling and experimental work suggested that the electrical coupling could play an important role through the synchronization of activity between the coupled pairs (Garcia et al., 2008, Wright and Calabrese, 2011a, b). That model was capable of producing many of the characteristic features of the leech heart motor neurons, but was unable to quantitatively achieve the relative phasing observed in the living system, suggesting that the properties of motor neurons not present in the model contribute meaningfully to the output patterns they produce (Garcia et al., 2008, Wright and Calabrese, 2011a, b). This model was a single compartment model and also did not contain I_{KCa}, a current known to be present in leech heart motor neurons that should be capable of influencing relative phasing, although via a different mechanism than I_h. Thus, we developed a new HE motor neuron model which was multi-compartmental and contained all the currents known to be present. We optimized this model through the use of an evolutionary algorithm, and we generated a population of model instances with wide ranges of underlying parameter values to better evaluate the role those parameters had in motor pattern formation by the HE motor neurons.

The leech heartbeat system

The leech nervous system is composed of 34 ganglia, with 21 segmental ganglia indexed by segment number, 6 fused ganglia in the anterior end (the head brain), and 7 fused ganglia in the posterior end (the tail brain), with each segmental ganglion connected via two parallel fused nerve cords. The entire nerve cord is contained within the ventral sinus as shown in Figure 1.1. The core leech heartbeat CPG comprises seven bilateral pairs of identified heart interneurons (HNs) that occur in the first seven ganglia, HN(1) through HN(7), with additional pairs in ganglia 15 and 16, HN(15) and HN(16) (Kristan et al., 2005, Wenning et al., 2008, Wenning et al., 2011) (see Figure 1.1). Six pairs of HNs are premotor, making ipsilateral inhibitory connections with a subset of the HE motor neurons. These premotor interneurons are grouped into front or oscillator premotor interneurons (HN(3) and HN(4)), middle premotor interneurons (HN(6) and HN(7)) and rear premotor interneurons (HN(15) and HN(16)). The latter, HN(15) and HN(16), were predicted by an earlier leech heart motor neuron model (Garcia et al., 2008) and subsequently found in the living system (Wenning et al., 2008, Wenning et al., 2011). As they were recently discovered, they have not been as extensively investigated, but they appear to receive excitatory electrical input from HN(6) and HN(7) and provide inhibitory input onto the rear heart motor neurons (Wenning et al., 2008, Wenning et al., 2011). The premotor heart interneurons control the activity of heart (HE) motor neurons in ganglia 3-18, with one coupled pair of HE neurons present in each ganglion, by sculpting bursts with rhythmic inhibitory input (see Figure 2.1B).

Figure 1.1 Leech nervous system and leech heartbeat system

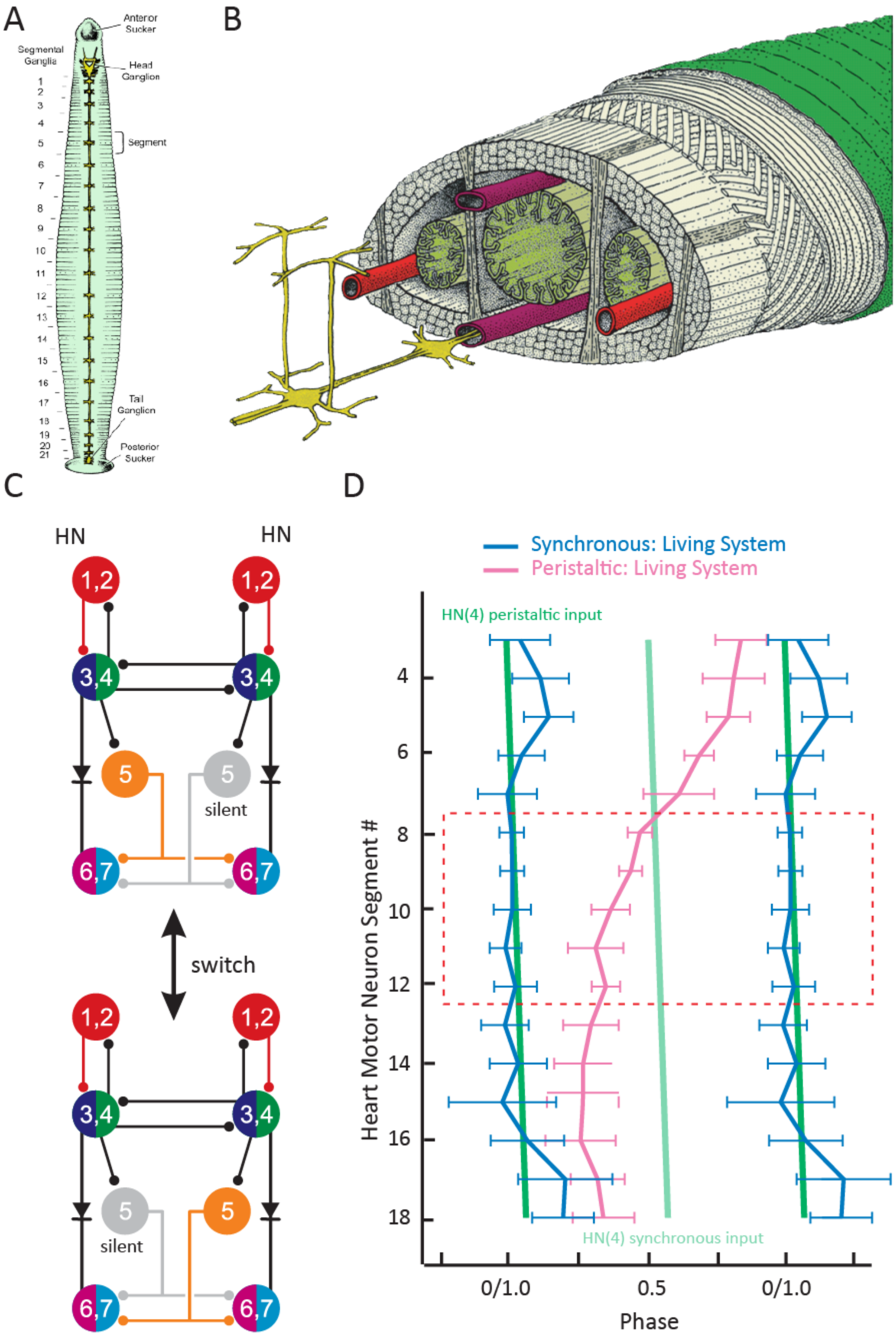

Figure 1.1 Leech nervous system and leech heartbeat system

A. Ventral view schematic of *hirudo*, sp. The nervous system is composed of 34 ganglia, with 21 segmental ganglia indexed by segment number, 6 fused ganglia in the anterior end (the head brain), 7 fused ganglia in the posterior end (the tail brain). Each segmental ganglion is connected via two parallel fused nerve cords. The entire ventral nerve cord is contained within the ventral sinus as shown in B. Adapted from (Kuffler and Martin, 1984)

B. Cut-away oblique view of the of the leech showing key anatomical features, in particular the nervous system, which is located in the ventral blood sinus, and the two lateral sinuses (longitudinal heart tubes). The dorsal and ventral blood sinus are passive, whereas the lateral heart tubes are active. Adapted from (Kuffler and Martin, 1984)

C. Schematic of the leech heart central pattern generator. The leech heart central pattern generator exhibits bilaterally asymmetric rhythmic activity composed of two unilateral modes, peristaltic and synchronous, that reciprocally switches every 20-40 cycles. Adapted from (Norris et al., 2006)

D. Phase diagram of the bilaterally asymmetric fictive motor pattern produced by the leech heart motor neurons for all heart motor neurons, located in ganglia 3-18 averaged across multiple animals. Pink and blue lines indicate mean phase. Green lines indicate phase of heart interneuron in ganglion 4 in the indicated mode (HN) inclusive of propagation delay. Midbody motor neurons modeled in this dissertation are highlighted with broken red box. Error bars indicate standard deviation. Adapted from (Garcia et al., 2008)

At any point in time, each side of the heartbeat system, inclusive of CPG, HE motor neurons, and heart tubes, will express one of two patterns while the other expresses the other: A rear-to-front peristaltic (peri or p) mode in which the heart tube pumps a bolus of blood from the rear to the front of the animal and a synchronous (sync or s) mode in which the heart tube contracts in a nearly simultaneous front to rear progression (Thompson and Stent, 1976, Calabrese, 1977, Krahl and Zerbst-Boroffka, 1983), see Figure 1.1D. Every 20 to 40 heartbeat cycles, generally 6 to 10 seconds each, the two sides reciprocally switch coordination modes. The exact cause for this switch is not yet known, but it is effected through a change in activity of the HN(5) interneuron (see Figure 1.1C). As this motor neuron is not premotor, we set aside the great mystery of what causes the switch. The heart motor neurons are coordinated by inhibitory synaptic input from the premotor interneurons, and the mid-body heart motor neurons, HE(8)-HE(15), receive input from the same complement of ipsilateral premotor interneurons, HN(3), HN(4), HN(6), HN(7), an attribute we use in development of our model.

The leech heartbeat system presents a unique opportunity for modeling: we have a complete complement of spike times and the relative synaptic strengths of premotor HN input and the associated output pattern for HE(8) and HE(12) in 12 animals (Norris et al., 2007b, Norris et al., 2011). In that series of extremely challenging experiments, ipsilateral HN(3), HN(4), HN(6) and HN(7) premotor interneurons as well as HE(8) and HE(12) were recorded simultaneously in both the peristaltic and synchronous mode. The relative phasing of the first, middle, and last spikes were extracted and their phasing relative to the HN(4) neuron was calculated. The mean spike frequency and the duty cycle for the HE motor neurons were also calculated. The HE motor neurons were also voltage clamped to measure the strength of the synaptic inputs. In total, this produced a complete input (spike times and synaptic weights) and output pattern (phase, duty cycle, spike frequency) with which we could constrain a HE motor neuron model.

Variability and co-regulation

Neurons are a varied class of cells, but within even a single neuron type, including identifiable neurons in stereotyped nervous systems, they can express a wide range of underlying parameter values, in particular the maximal conductance density of ion channels (Prinz et al., 2004, Norris et al., 2011, Roffman et al., 2012). There are many reasons that this may be the case. If a neuron is insensitive to perturbation of a parameter, then a wide range of values for that parameter has little to no effect on its characteristic activity or the input-output transformation it performs. Alternately, two or more parameters may compensate for or oppose one another, producing a complicated area of support in parameter space in which neurons produce the correct activity (See Figure 1.2A). In some cases the resulting distribution of parameter values is complex, and a mean derived from samples drawn from within this area of support falls outside of it (Golowasch et al., 2002). Models constructed based on average values can thus misrepresent the system they seek to model. It is thus important to make multiple measurements in individual animals when we seek to understand the functional implications of different parameter values or interactions between them (Goaillard et al., 2009, Taylor et al., 2009). In the leech heartbeat system the strength of synapses has been extensively investigated and they have been found to vary extensively from animal to animal (Weaver et al., 2010, Norris et al., 2011, Roffman et al., 2012). In particular, the synapses from premotor interneurons onto heart motor neurons follows a pattern which, when averaged across animals, is consistent with our general idea of how the heart motor neuron pattern is formed. In the peristaltic mode, HN(3) and HN(4) burst later than HN(6) and HN(7), and we would expect the motor neurons which fire later to have stronger synaptic strengths with the later bursting interneurons, and vice versa. On average, this is the case. When one considers individual animals, however, the situation becomes more complicated. In many animals the HE(8) motor neuron, in which we would expect to find the strongest synaptic strengths from the HN(3) and HN(4) motor neurons, had strong, sometimes the strongest, inputs from HN(6) and HN(7) (see Figure 1.2B).

When such multidimensional measurements have been made in living neuronal networks by measuring mRNA levels correlations have been found, for example between two opposing currents, I_A and I_h (Schulz et al., 2006, Schulz et al., 2007, Tobin et al., 2009). Furthermore, manipulations of one of these through mRNA injection resulted in increased expression of the other in a homeostatic manner, maintaining normal activity (MacLean et al., 2003, MacLean et al., 2005).

We used an evolutionary algorithm to generate and improve model instances with the goal of finding many acceptable instances as opposed to a single optimal instance. Evolutionary algorithms are effective tools for optimization (minimization of error), including for the refinement and generation of model neurons (Bower et al., 1998, Achard and De Schutter, 2006, Tobin et al., 2006, Hendrickson et al., 2011b, a). Evolutionary algorithms require no assumptions about the underlying problems – no requirement for differentiability or local monotonicity, for example, as is required by many standard optimization approaches. The basic evolutionary algorithm is a discretization of the basic ideas of biological evolution: the present population is evaluated and the fittest individuals are used to generate the next generation through crossover of the vectors which define the parent individuals and typically some form of sporadic random mutation. Because they inherently operate through the use of populations, evolutionary algorithms are also a useful tool for the generation of populations of neural models. The individual model instances in these populations have a range of values for each parameter, much as has been found in the living system. We thus seek to capture some aspects of this variability in our modeling approach itself.

Figure 1.2 Failure of averaging and synaptic weight variability

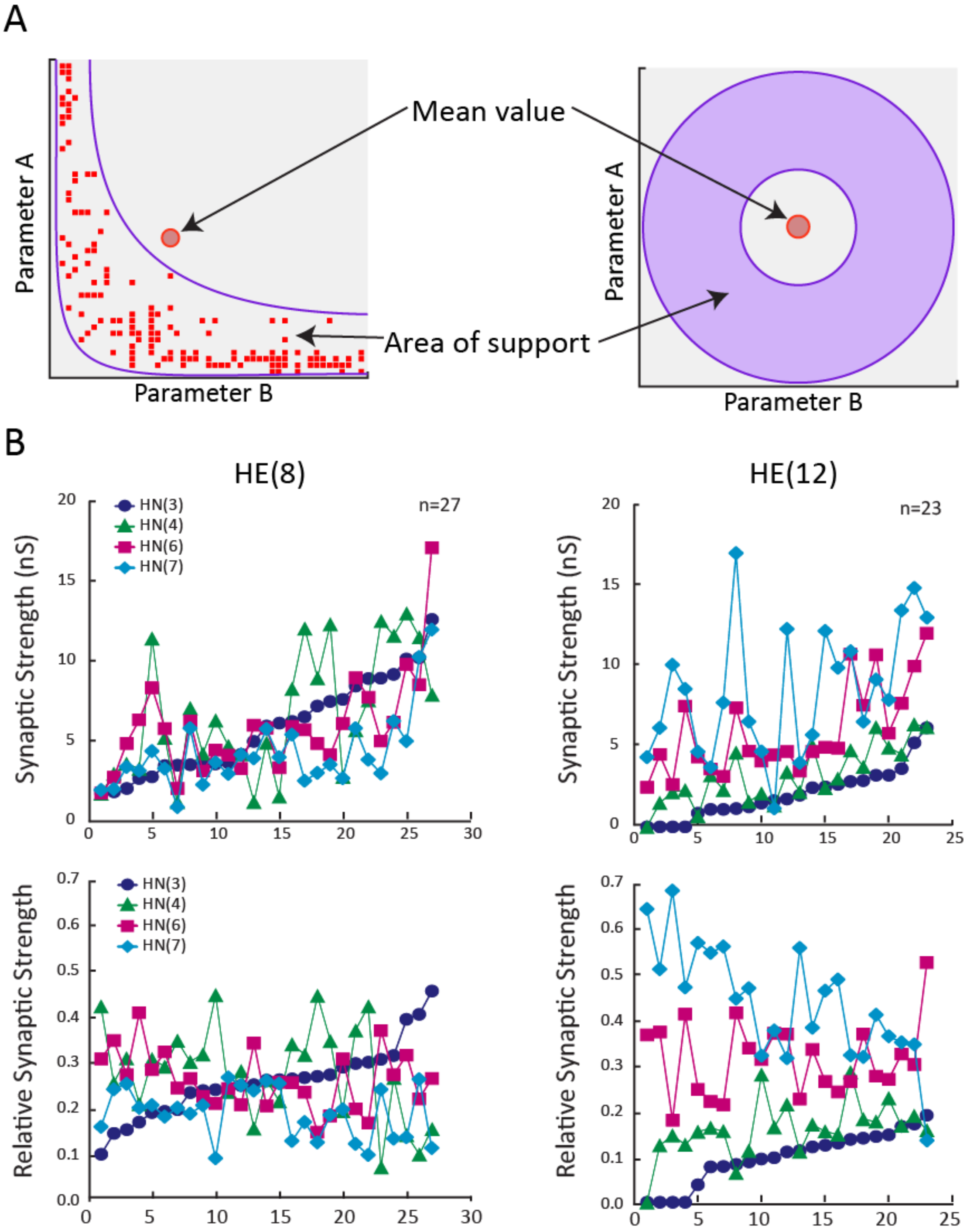

Figure 1.2 Failure of averaging and synaptic weight variability

A. The area of support, or the region of parameter space in which models produce functional output patterns, can be convex or convoluted. Where this is the case, averaged parameter values across many experiments can lead to model instances which do not produce the desired behavior as they fall outside of this area of support.

B. Raw and normalized synaptic heart interneuron to motorneuron synaptic strengths ordered by HN(3) strength in individual animals. The synaptic weights from the interneurons onto the motor neurons show wide variability.

Chapter 2: Model construction and framework

Input/output dataset

The HE motor neurons produce rhythmic bursts of activity that are coordinated between segments, and these bursts are sculpted by inhibitory input from the premotor interneurons. Because they require input to produce their characteristic activity, HE motor neuron models cannot be meaningfully simulated in isolation. Furthermore, since we wished our model to produce activity replicating that found in the living system, we required some measures of output corresponding to the inputs we delivered to it. We chose a specific input/output dataset from those extensively described in previous reports (Norris et al., 2006, Norris et al., 2007b, Wright and Calabrese, 2011b).

These datasets consisted of simultaneous extracellular (loose cell-attached patch) recordings from all ipsilateral premotor heart interneurons (HN(3), HN(4), HN(6), and HN(7)) in addition to HE(8) and HE(12) motor neurons, see Figure 2.1. These extracellular recordings were long enough to include the peristaltic and synchronous modes, so we had an input and an output pattern for ipsilateral HE(8) and HE(12) for both modes. Spikes were detected in these recordings and then the relative phase of the first, middle and last spikes was calculated. The duty cycle, the difference in phase between the last and first spike, as well as the average spike frequency for the HE motor neurons were also calculated, giving us targets for most of the fitness metrics used in the present study. The HE motor neurons were then penetrated with intracellular electrodes and the strength of the HN to HE synaptic weights were measured in dSEVC (dynamic single electrode voltage clamp) while still recording from the 4 ipsilateral interneurons, see Figure 2.2. The voltage clamp traces were smoothed with a Gaussian filter and then averaged with spike triggered averaging triggered by the spikes of each of the four HN cells, to yield a measure of the relative synaptic strength. This process was successfully completed in 12 individual animals, and we chose one of these input/output datasets to develop the present model. Since we simulated the neurons as electrically coupled pairs, one peristaltic and one synchronous, we required bilateral rather than unilateral input patterns. To achieve this, the two coordination modes were aligned to produce a complete bilateral input spike time pattern with experimentally observed phasing between the two sides (0.51) (Norris et al., 2006) by aligning the 12 synchronous and 12 peristaltic bursts. The output targets for phase, duty cycle and spike frequency were measured in the recorded output pattern averaged across the bursts. Slow wave height and spike height require unclamped intracellular recordings which were not available for every motor neuron, so these targets were taken from established average values from leech heart motor neurons recorded in other experiments. In aggregate, each individual animal input/output dataset consisted of spiketimes and synaptic weight profiles for the 4 premotor interneurons in each coordination mode (8 total) and fitness targets for the spike height (15mV), slow wave height (10mV), spike frequency (7.368Hz), peristaltic phase (HE(8):0.556, HE(12):0.475), peristaltic duty cycle (HE(8):0.337, HE(12):0.462), synchronous phase (HE(8):0.077, HE(12):0.113), and synchronous duty cycle (HE(8):0.436, HE(12):0.462).

Figure 2.1 Input/Output dataset: Phase, duty, spike frequency

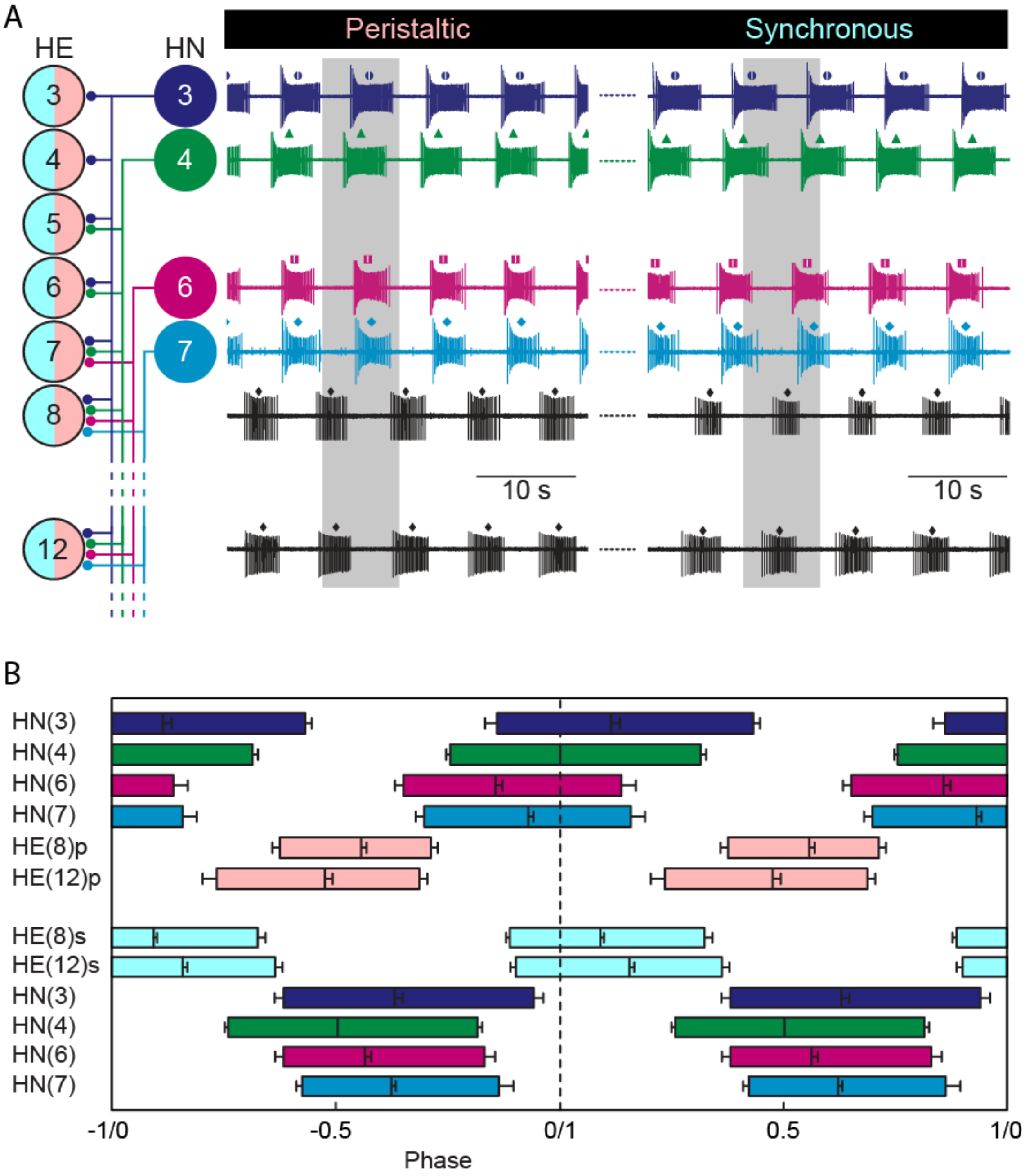

Figure 2.1 Input/Output dataset: Phase, duty, spike frequency

A. Schematic and representative raw input/output dataset used to develop the present leech heart motor neuron model. All premotor interneurons and two heart motor neurons on one side of the animal were recorded with extracellular electrodes through both peristaltic and synchronous modes (snapshot of one animal's data shown). Detected spiketimes for premotor interneurons used as input to model and phase, duty cycle, and spike frequency of heart motor neurons used as fitness target for model. Middle spike indicated with symbol above each trace. Data from (Norris et al., 2011)

B. Phase diagram showing relative phasing of premotor interneurons and HE(8) and HE(12) motor neurons for a single animal. Leading edge of each bar indicates first spike, middle line indicates middle spike, and trailing edge indicates last spike. Synchronous mode is aligned with peristaltic mode according to established side-to-side relative phase (0.51) to produce input spike times. Error bars indicate standard deviation. Data from (Norris et al., 2011)

Figure 2.2 Input/Output dataset: Synaptic weights

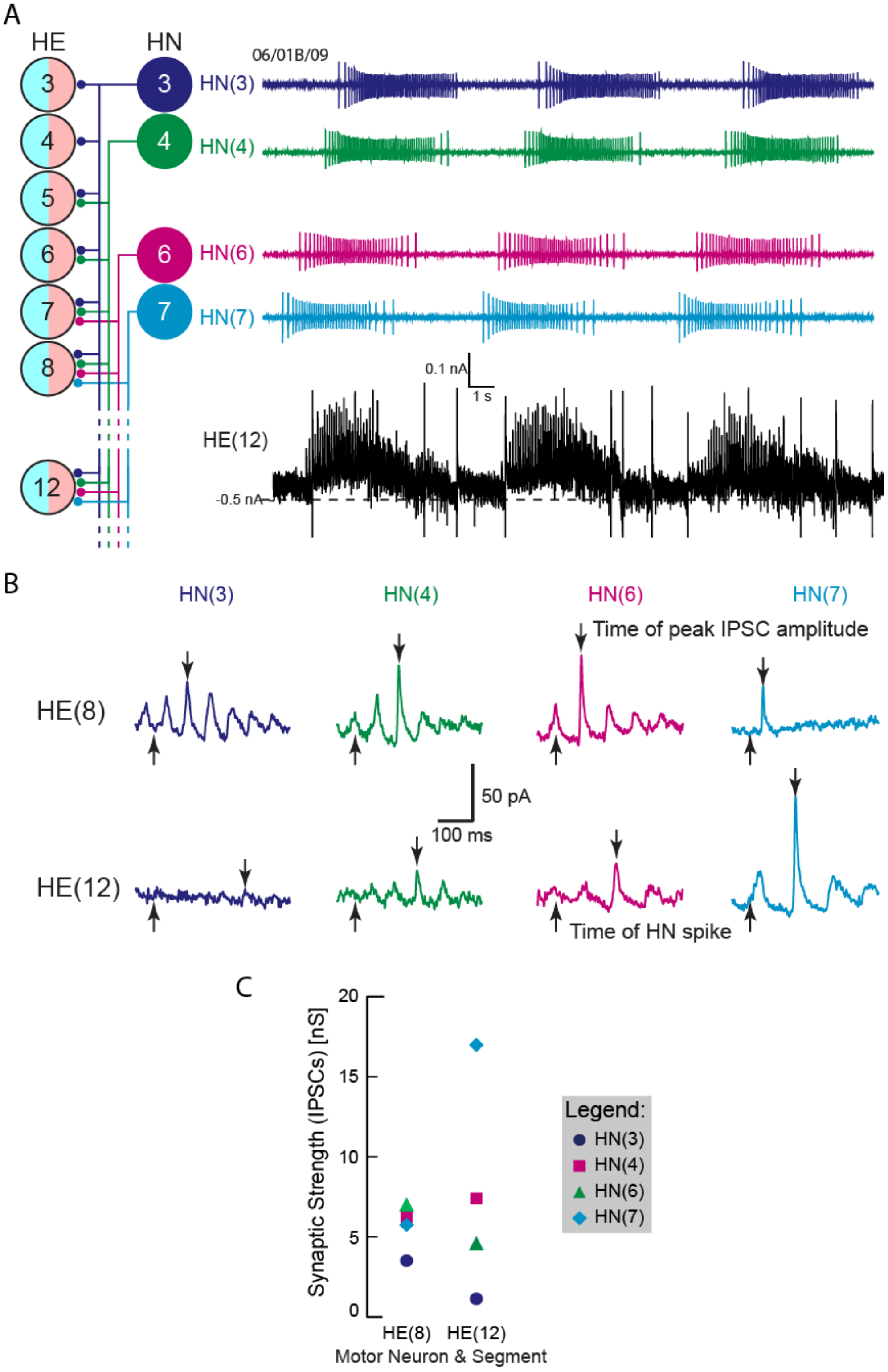

Figure 2.2 Input/Output dataset: Synaptic weights

A. Schematic and representative data used to generate synaptic weight portion of input/output dataset used to develop the present heart motor neuron model. Premotor interneurons were recorded with extracellular electrodes while leech heart motor neurons were recorded with intracellular electrodes and placed in voltage clamp to record inhibitory post synaptic currents. Adapted from (Norris et al., 2011)

B. Spike triggered averages from the voltage clamped trace triggered off of each premotor interneuron's spikes for HE(8) and HE(12). Arrows indicate the time of the indicated HN interneuron spike and IPSC amplitude, demonstrating conduction delay. Maximal IPSC amplitude was measured and used in input/output dataset. Adapted from (Norris et al., 2011)

C. Measured synaptic strengths for the spike triggered traces in B. These relative synaptic strengths were used in the input/output dataset for the present model. Adapted from (Norris et al., 2011)

Evolution and simulation framework

Multi-objective evolutionary algorithms (MOEA) are a class of optimization algorithm that is especially well suited to the development of neuronal models. Evolutionary algorithms have been successfully used to generate and optimize many neuronal models (Vanier and Bower, 1999, Tobin et al., 2006, Hendrickson et al., 2011b), but MOEAs obviate a common concern in the use of evolutionary algorithms, the selection of a weighting or scalar function to aggregate the many fitness metrics used. In most evolutionary algorithms, some direct comparison has to be made between fitness metrics which are inherently orthogonal. In MOEAs, this evaluation is kept separate, see Figure 2.3. The best model instances, as evaluated on each fitness metric independently, are those used to produce the subsequent generation. When successful, the eventual result is a diverse population of model instances which achieve the targets for all metrics. Because evolutionary algorithms are inherently stochastic, they are not guaranteed to find any solution (good model instances), let alone an optimal one, but they are routinely successful, even in cases where most standard optimization algorithms fail.

The MOEA we used (Smolinski and Prinz, 2009b) was unaltered except for its interface. The MOEA was adapted to run on Emory University's High Performance Computing cluster Ellipse, which ran the Sun Grid Engine queuing system, by adjusting the interface to run on the master node and submit jobs to the queuing system. The interface was also adjusted to create the appropriate HE model definition files and to submit each generation as a batch to the execution queue. After submission, the algorithm entered a loop in which it slept for several minutes before checking whether all simulations had been completed. In some cases, problems with the cluster impeded proper completion of simulations, with jobs either stalling or unaccountably disappearing from the queue. As such, the algorithm also ensured that there were pending simulations in the queue and, if not, it resubmitted a new batch job for the missing simulations.

For each run, the MOEA created an initial generation with random parameter values and then submitted those model instances for simulation, see Figure 2.3. The resulting fitness values were read into and used by the MOEA to select the best model instances, which were used to produce the next generation, and the process was repeated. On each node there were separate simulation (in the GENESIS framework) and analysis (custom Matlab code) modules, see Figure 2.4. The simulation comprised an input module and two coupled motor neuron model pairs (HE(8)p, HE(8)2, HE(12)p and HE(12s). The model instances were loaded from the cell definition file produced by the MOEA. The input module was the same for all model instances and was drawn from the input dataset that contained the predetermined HN spike times, the modulation waveform, and the synaptic weights for each synapse. The 4 motor neuron model instances each contained a delay buffer for the spike times and the modulation waveforms that delayed that input by 20ms/ganglion. Alternatively, the delays could have been added to the output during analysis, as the ganglia are independent, or there might have been separate sets of modulation waveform for each ganglion, as in the previous single compartment model. We opted to use a delay table because the resulting output waveforms would be properly timed without further processing and because the delay buffers added a negligible amount of computation during the simulation and only required that a single set of modulation waveforms had to be loaded, improving the total simulation runtime. The synaptic weights are set according to the input module and remained fixed throughout the simulation. When executed, the simulations loaded the input data and the model instance defined by the MOEA and then simulated it, producing a soma compartment membrane voltage for each HE motor neuron modeled. The resulting waveforms were then analyzed and deleted, and the fitness values and all intermediate data used to calculate the fitness were copied back to the master node.

Figure 2.3 Multi Objective Evolutionary Algorithm

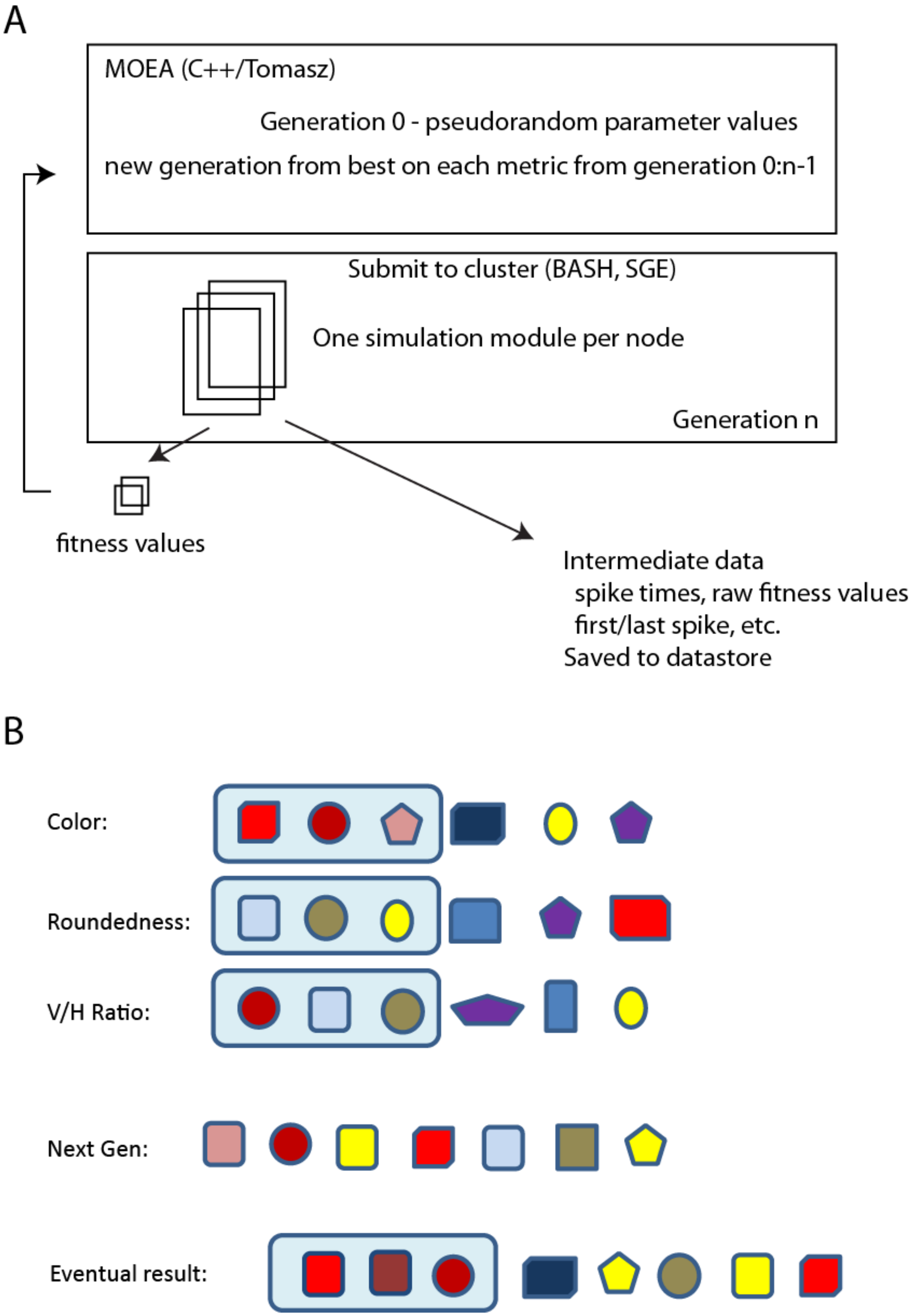

Figure 2.3 Multi Objective Evolutionary Algorithm

A. Flowchart for Multi Objective Evolutionary Algorithm (MOEA) execution on the cluster. The MOEA generated each generation based on the best model instances from all prior generations as measured independently on each fitness metric. All novel instances, those which had not already been simulated, were submitted to the cluster to be simulated. After each generation, fitness values are loaded and used to generate the subsequent generation. Intermediate data, that which is necessary to calculate the fitness metrics, is saved whereas the raw soma compartment membrane voltage is discarded.

B. Simplified example of the function of a MOEA. Each metric (color, roundedness, vertical/horizontal ratio) is independently assessed for the present generation. Those shapes, representing model instances, closest to the target on each individual metric (i.e/, red, rounded, and aspect ratio), highlighted, are used to generate the next generation. The new generation is then analyzed in the same manner, and eventually, a final generation will contain exemplar model instances.

Figure 2.4 Single node modules

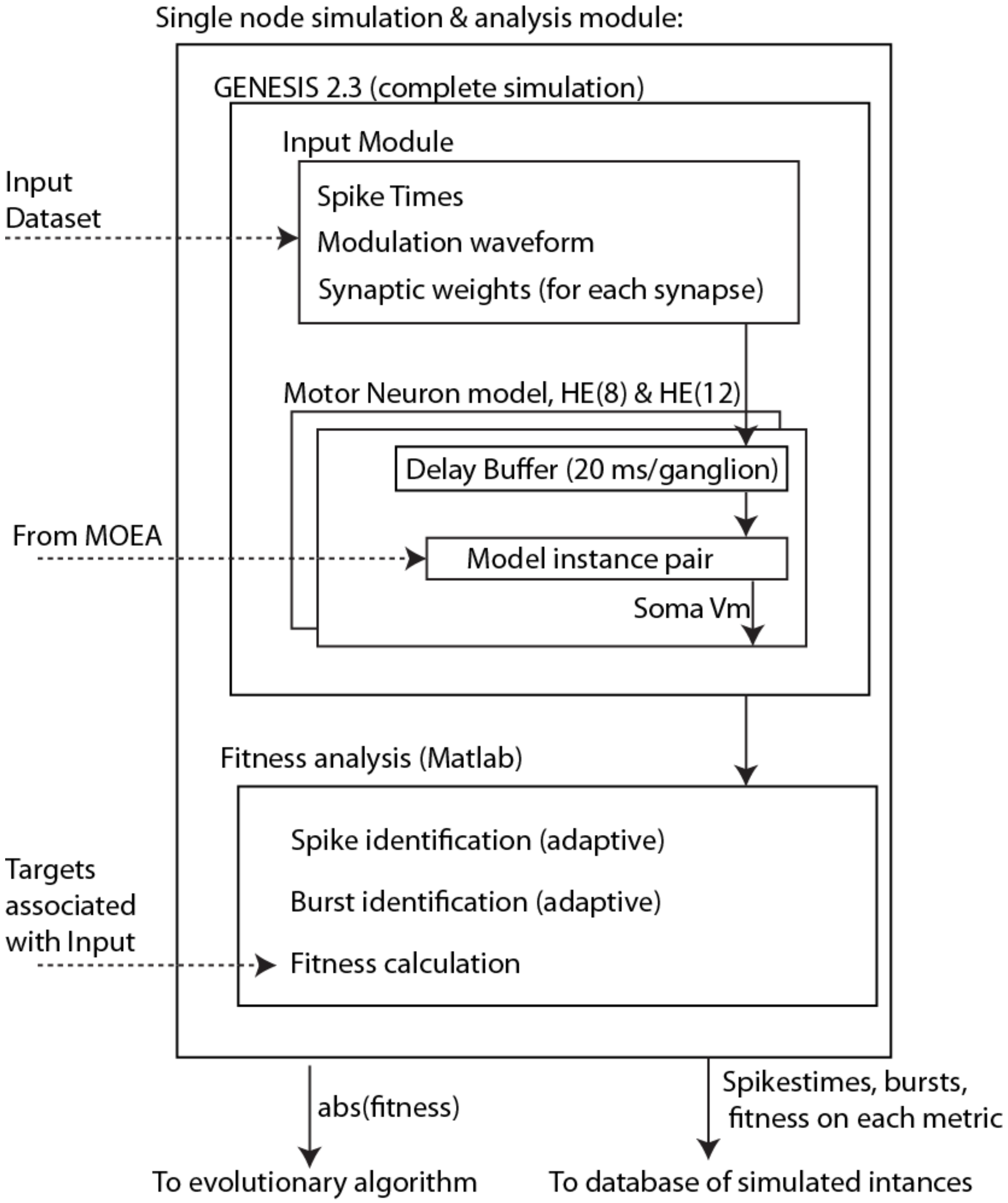

Figure 2.4 Single node modules

Flowchart schematic for model execution and analysis on each node. Each node on the cluster independently simulates a model instance for four identical model motor neurons, HE(8) and HE(12) in both modes, with an individual animal's input pattern (spike times, modulation waveform, synaptic weights). Soma compartment membrane voltage is saved and analyzed by a matlab function to calculate the fitness metrics. Both the resulting fitness values, calculated against the associated target values, and intermediate data, including spike times, burst parameters, raw fitness metric values, etc., are copied to the master node. Soma membrane voltage is discarded after analysis due to space constraints.

Updated synapse model

We now turn our attention to the synaptic input. The previous single compartment HE model used a standard double exponential model of a spike mediated synaptic channel with a rising time constant (τ_{rise}) of 4ms and a falling time constant (τ_{fall}) of 150ms. This resulted in a broad inhibitory post synaptic current (IPSC) for each presynaptic spike that summated and produced robust slow wave of inhibition. In the present multi-compartmental model, this results in a soma compartment membrane voltage that is qualitatively too smooth during bouts of inhibition. Furthermore, the IPSP shape recorded to produce the input patterns used in the present model appeared sharper than those used to develop the previous model. To better replicate the waveform observed in the living system, which has both spike mediated and graded components (Norris et al., 2007a), the new synapse model consisted of two spike triggered double exponentials that together captured the observed electrophysiology, one with a shorter fall time (τ_{fall}= 12.5ms, τ_{rise}=4ms) and the other with a longer fall time (τ_{fall}=150ms, τ_{rise}=4ms), with the slower component's maximum conductance set to 0.33 times the faster component ($\bar{g}_{slow} = 0.33\ \bar{g}_{fast}$), resulting in a combined waveform which approximated the shape of inhibitory post-synaptic currents (IPSCs) observed in the living system, see Figure 2.5A.

In the living system, the inhibitory input synapses exhibit intraburst synaptic plasticity. The IPSCs are initially quite small and then increase to a stable level before declining towards the end of each presynaptic burst (Norris et al., 2007a). To achieve this, the individual HN to HE synapses were modulated (their maximal conductance was multiplied by a factor between 0 and 1) by a predetermined modulation waveform generated for each set of spiketimes. The modeled modulation waveform approximated this rising and falling behavior with an exponential rise from a factor of 0.01 to 1 for 90% of the burst duration and then an exponential decay for the final 10%, similar to previous leech heart motor neuron models (Garcia et al., 2008, Wright and Calabrese, 2011a, b). For each prerecorded input, we calculated the appropriate rise and fall time constants from the average time for the first and final 5 spikes in each burst, for rise and fall time constants, respectively, for each premotor interneuron. Thus the complete input pattern delivered to each model instance consisted of a modulation waveform and a train of spikes for each premotor interneuron. The net result was that the model qualitatively resembled the living system more closely, see Figure 2.5B.

Figure 2.5 Synapse model

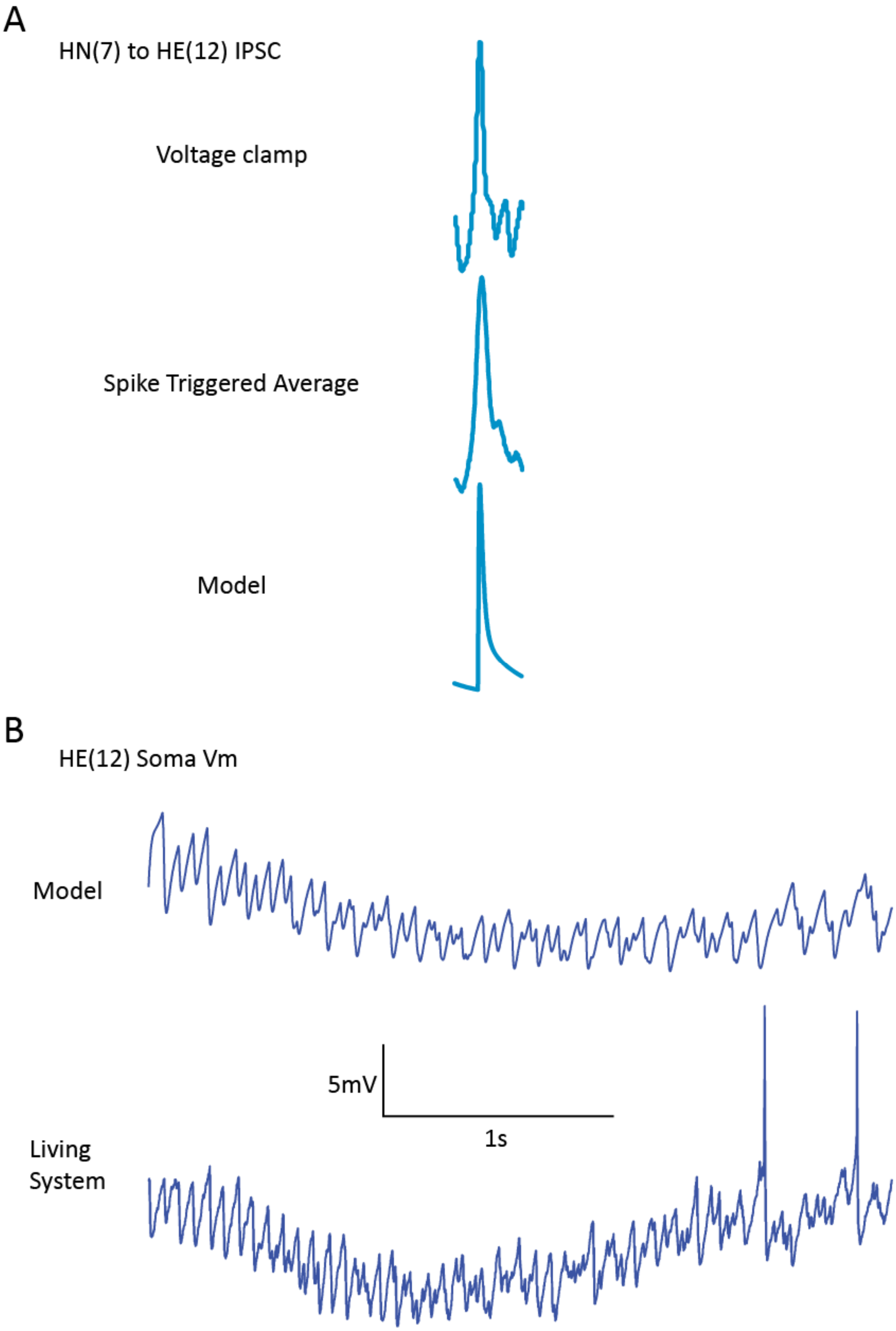

Figure 2.5 Synapse model

A. Comparison of living system inhibitory post synaptic current (IPSC) as measured in voltage clamp and model synaptic conductance. The new model is a combination of a faster and a slower component to better match the shape observed in the living system. Living system traces are filtered with a Gaussian filter. Living system data courtesy of A. Wenning.

B. Comparison of inhibitory post synaptic potential in the living system and a model instance. Note that the premotor interneuron spike times and synaptic strengths differ between the two traces. Living system data courtesy of A. Wenning.

Calcium sensitive potassium channel model

The previous HE models did not contain two currents present in the living system, slow calcium I_{CaS} and calcium sensitive potassium I_{KCa}. We used an established model for I_{CaS}, however there is not an established model leech I_{KCa}, so we developed a simple one based on previously published measurements (Opdyke and Calabrese, 1995), see Figure 2.6Figure 2.5. We started with the established I_{K2} model and then adjusted the half activation and slope to more closely match that estimated from the living system for I_{KCa}. We then added a linear calcium gate and set the range over which it was active from calcium imaging measurements in leech heart interneurons (Ivanov and Calabrese, 2000). To couple this calcium gate to the calcium fluxed through I_{CaS}, we added a simple calcium pool (exponential decay of $\tau = 1.5s$). The net result is that I_{KCa} increases throughout each burst towards a steady state. High levels of I_{KCa} can abbreviate bursts, radically shifting their phase and reducing their duty cycle.

Figure 2.6 Calcium-sensitive potassium conductance

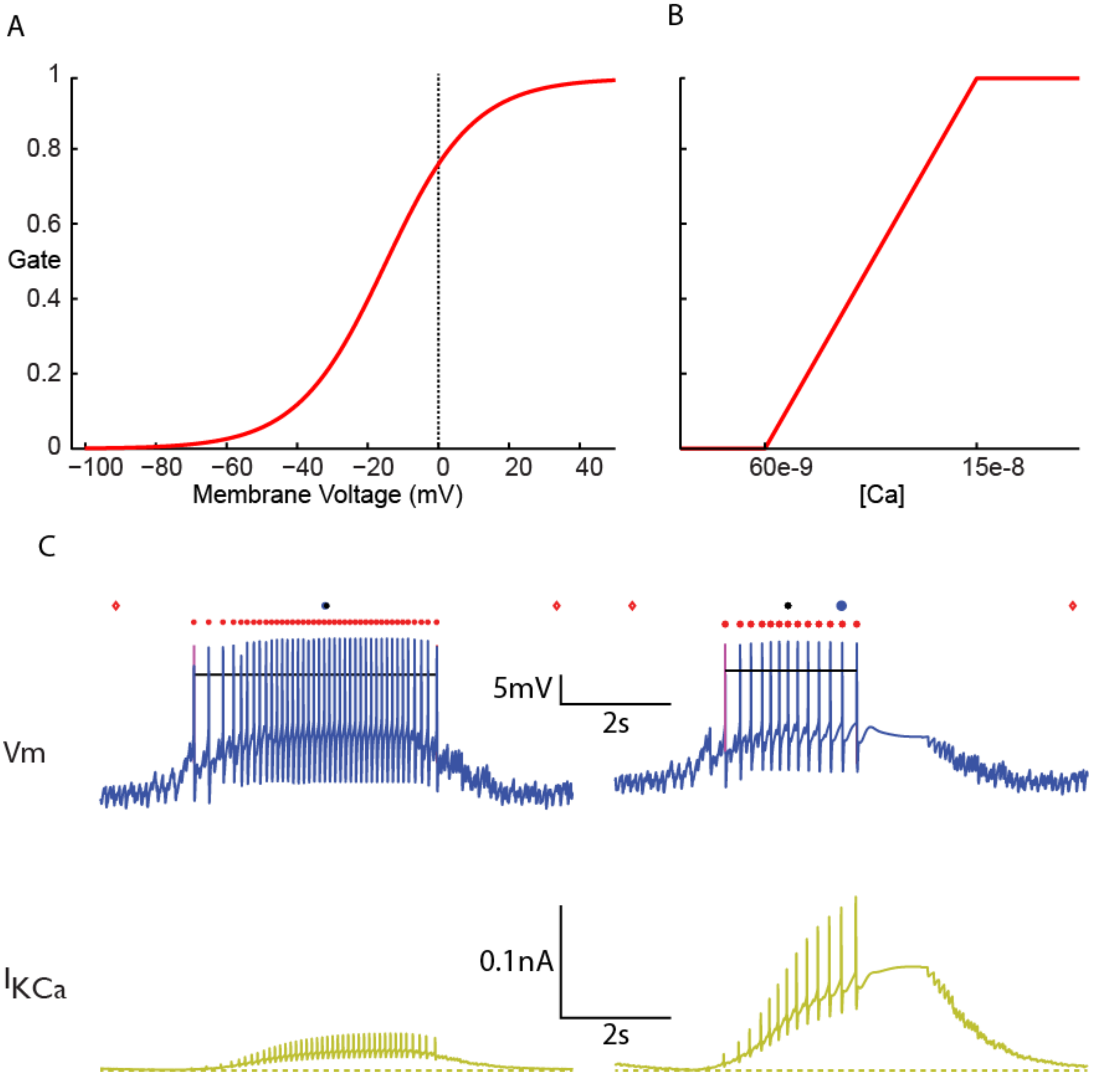

Figure 2.6 Calcium-sensitive potassium conductance

A. Activation gate variable for new calcium sensitive potassium channel based on the leech K2 channel model with minor modifications including a positive shift of higher half activation voltage and a minor adjustment to the slope to correspond to those previously reported in (Opdyke and Calabrese, 1995).

B. Calcium sensitive gate for new calcium sensitive potassium channel.

C. Soma compartment membrane voltage and current through the new channel in two model instances. The current builds through the burst. High levels of the current will result in a radical advance of the middle spike, and thus phase, as well as a reduction in spike frequency and duty cycle. The detected spikes (red dots) and the phase reference (red diamond), duty cycle (black line through spikes), phase target (blue circle) and measured phase (black circle) are shown.

Chapter 3: Correlated Conductance Parameters in Leech Heart Motor Neurons Contribute to Motor Pattern Formation

Abstract

Neurons can have widely differing intrinsic membrane properties, in particular the density of specific conductances, but how these contribute to characteristic neuronal activity or pattern formation is not well understood. To explore the relationship between conductances, and in particular how they influence the activity of motor neurons in the well characterized leech heartbeat system, we developed a new multi-compartmental Hodgkin-Huxley style leech heart motor neuron model. To do so, we evolved a population of model instances, which differed in the density of specific conductances, capable of achieving specific output activity targets given an associated input pattern. We then examined the sensitivity of measures of output activity to conductances and how the model instances responded to hyperpolarizing current injections. We found that the strengths of many conductances, including those with differing dynamics, had strong partial correlations and that these relationships appeared to be linked by their influence on heart motor neuron activity. Conductances that had positive correlations opposed one another and had the opposite effects on activity metrics when perturbed whereas conductances that had negative correlations could compensate for one another and had similar effects on activity metrics.

Introduction

Many critically important behaviors are controlled by neuronal networks called Central Pattern Generators (CPGs) (Marder and Calabrese, 1996). CPGs underlie many canonical movement patterns which are critical for life, such as respiration (Ramirez, 2011), locomotion (Kiehn, 2006, Kiehn et al., 2010, Kiehn, 2011, Lamb and Calabrese, 2011, Mullins et al., 2011), and circulation, the system on which we focus here. The successful production of these movement patterns requires coordinated muscle activity. Motor neurons driven by these CPG networks have generally been considered followers of the CPG output. More recently, studies have found that motor neurons, in particular leech heart motor neurons, themselves contribute to the production of their output patterns (Garcia et al., 2008, Wright and Calabrese, 2011a, b). While inputs from premotor interneurons of a leech heart CPG are responsible for the majority of the motor neuron output, motor neurons do not simply follow their input: intrinsic properties appear to play an important role (Garcia et al., 2008), although only a few have been specifically studied (Wright and Calabrese, 2011a, b).

There is a growing consensus in the field that neurons have widely different underlying parameters, especially those associated with intrinsic membrane properties, even while maintaining their identity and characteristic activity (Prinz et al., 2004, Goaillard et al., 2009, Grashow et al., 2009, Tobin et al., 2009, Hudson et al., 2010, Hudson and Prinz, 2010, Marder, 2011). Intrinsic membrane properties, especially those determined by the maximal conductances ($\bar{g}$) of pools of voltage-gated ion channels, can show in the identifiable neurons of invertebrate nervous systems considerable (up to five fold) animal-to-animal variability, which has been particularly well documented in the crustacean stomatogastric nervous system (STNS) (Prinz et al., 2004, Goaillard et al., 2009). In the STNS the levels of mRNA that code for these channels have similarly been found to be highly variable (Schulz et al., 2007, Tobin et al., 2009). Nevertheless, networks of neurons and even individual neurons can produce tightly regulated activity patterns despite having these widely different underlying parameters. Such animal-to-animal variability in maximal conductances has also been shown for synaptic strengths in the leech heartbeat system (Norris et al., 2007a, Roffman et al., 2012). In all these cases, the wide range in values observed could simply be because measured parameters, i.e. the maximal conductance of synapses or ionic currents, do not meaningfully influence the characteristic activity of those neurons, or pairs or sets of these properties could jointly maintain characteristic activity. In particular, the maximal conductances of voltage gated currents that oppose or compensate for one another may be co-regulated or counter-regulated, respectively. In such cases, we should find correlations between these parameters, likely linked by their influence on characteristic activity. Beyond the putative existence of such correlations in the motor neurons we are investigating, it is important to determine how cellular parameters affect the input-output transformation of these neurons. How are leech heart motor neurons coordinated by their inputs, what do they contribute to the patterns they produce, and in particular what role do active membrane conductances play in producing a coordinated motor pattern? Accordingly, we sought a motor neuron model that accurately produced their biological activity and recapitulated the animal-to animal variability of biological neurons.

Leech heartbeat system

We investigated the heart (HE) motor neurons that innervate the tubular hearts of the leech. The leech heartbeat system has been described in great detail previously (Kristan et al., 2005, Norris et al., 2006, Norris et al., 2007b, a, Norris et al., 2011, Wenning et al., 2011), so we briefly outline the relevant features of its organization here. The bilateral heart tubes are driven by the ipsilateral member of the pairs of leech heart (HE) motor neurons in ganglia 3 through 18 (HE(3)-HE(18)) of the 21 midbody segmental ganglia (Maranto and Calabrese, 1984, Kristan et al., 2005). These motor neurons are controlled by barrages of inhibitory synaptic input from a core CPG consisting of 7 pairs of interneurons located in midbody ganglia 1-7 of the animal. The motor neurons in ganglia 8 through 14 receive input from the four ipsilateral premotor interneurons of this core CPG, so the temporal pattern of spikes each receives from each ipsilateral premotor interneuron is identical, except for conduction delays, in particular for the two pairs we specifically focus on, HE(8) and HE(12) (Figure 3.1A). The heart motor neurons in ganglia 3 through 7 receive input from only a subset of the premotor interneurons, as shown in Figure 3.1A, as well as input from a pair of unidentified interneurons (not shown), and those in 15 through 18 receive additional input from the rear interneurons (Wenning et al., 2011). The CPG produces a bilaterally asymmetric pattern, with the premotor interneurons on one side coordinated nearly synchronously while the opposite side is coordinated in a peristaltic rear-to-front progression. These two patterns are imposed on the motor neurons, which produce the corresponding patterns, by the interneurons on each side sculpting the tonic activity of ipsilateral motor neuron into bursts with inhibitory synaptic input. Thus each side of the whole heartbeat system expresses one of two coordination modes of activity at any point in time (Figure 3.1B): either nearly synchronous activity (referred to as the synchronous mode) which gives rise to near synchronous contractions in the ipsilateral heart tube, or a rear-to-front progression of activity, which gives rise to a corresponding peristalsis in the ipsilateral heart tube (referred to as the peristaltic mode) (Thompson and Stent, 1976, Wenning et al., 2004). The core CPG, and thus the heartbeat system as a whole, alternates between one state (left/peristaltic right/synchronous), where the entire left side of the network is producing the peristaltic pattern and the right side is producing the synchronous pattern, and the reciprocal state (left/synchronous right/peristaltic), with the transitions between these states occurring precipitously every 20-40 beats (Gramoll et al., 1994, Lu et al., 1999). Since each motor neuron alternately produces both activity modes, each motor neuron has to produce both input-output transformations, with the pattern produced depending on the temporal pattern of its input. Not only do the switches between modes occur every few minutes, but measurements of synaptic weights show no difference between modes (Norris et al., 2007a), so each motor neuron must produce both patterns without any change in its synaptic weights.

To develop a new model of HE motor neurons, we took advantage of a unique complete input-output data set. Norris et al. (Norris et al., 2007b) recorded simultaneously from all interneurons which synapse onto the midbody heart motor neurons as well as from two motor neurons (HE(8) and HE(12)) themselves during both the peristaltic and synchronous modes, giving us a complete temporal pattern of input and output for 12 animals, one of which was used for this investigation (Figure 3.1). Furthermore, the strength of these synapses was measured in the same preparation after recording these temporal patterns (see Figure 3.1C). Measures of the motor neuron activity, in particular phase, duty cycle, and spike frequency, can be used as targets associated with a specific input pattern. The combination of the synaptic strengths with the temporal patterns of spikes from each premotor interneuron gave us a complete input pattern that, when combined with corresponding output targets, allows us to focus on the intrinsic properties of the motor neurons we seek to model. It is important to emphasize here that the only difference between the input to the HE(8) and the HE(12) motor neurons is the synaptic weights of their four inputs in each of the coordination modes, although there is a small offset in spike timing of 80ms due to conduction delay. The requirement that each model motor neuron must be capable of producing both the peristaltic and the synchronous output patterns appropriate to its segment and the individual animal dataset give us the ability to constrain our models with electrophysiological targets specific to both the peristaltic and synchronous input patterns with which they are simulated.

Previous modeling work has created model leech heart motor neurons which qualitatively captured some of the activity pattern features of those found in the living system, but had difficulty achieving the appropriate phase within a reasonable window (Garcia et al., 2008, Wright and Calabrese, 2011a, b). This heart motor neuron model simplified the morphological complexity into a single isopotential compartment and contained an incomplete complement of membrane conductances. We built upon these modeling efforts and developed a multi-compartmental leech heart motor neuron model which compromised between capturing morphological complexity and reducing computational complexity and included all active conductances believed to be present in the living system. This model was parameterized by the maximal conductance densities of the active membrane conductances and the electrical coupling as described in the Methods. Each instance of the model had a unique set of specific values for each of these maximal conductance densities. Rather than hand tune or attempt a deterministic multi-target optimization algorithm, we used an evolutionary algorithm to find model instances which achieved our target ranges on our fitness metrics. Evolutionary algorithms, including the specific algorithm we used (Smolinski et al., 2008, Smolinski and Prinz, 2009b), have been shown to be efficient at identifying good model instances, although they are typically stochastic and not guaranteed to be successful (Vanier and Bower, 1999, Tobin et al., 2006, Hendrickson et al., 2011a). To generate and evaluate these model instances, we used an input-output dataset from a single animal and the corresponding targets on each of our metrics. Because we had input-output data for both HE(8) and HE(12) heart motor neurons, we were also able to examine possible differences between them to generate predictions of general properties of leech heart motor neurons.

Figure 3.1 Front leech heart motor neuron circuit and input/output pattern

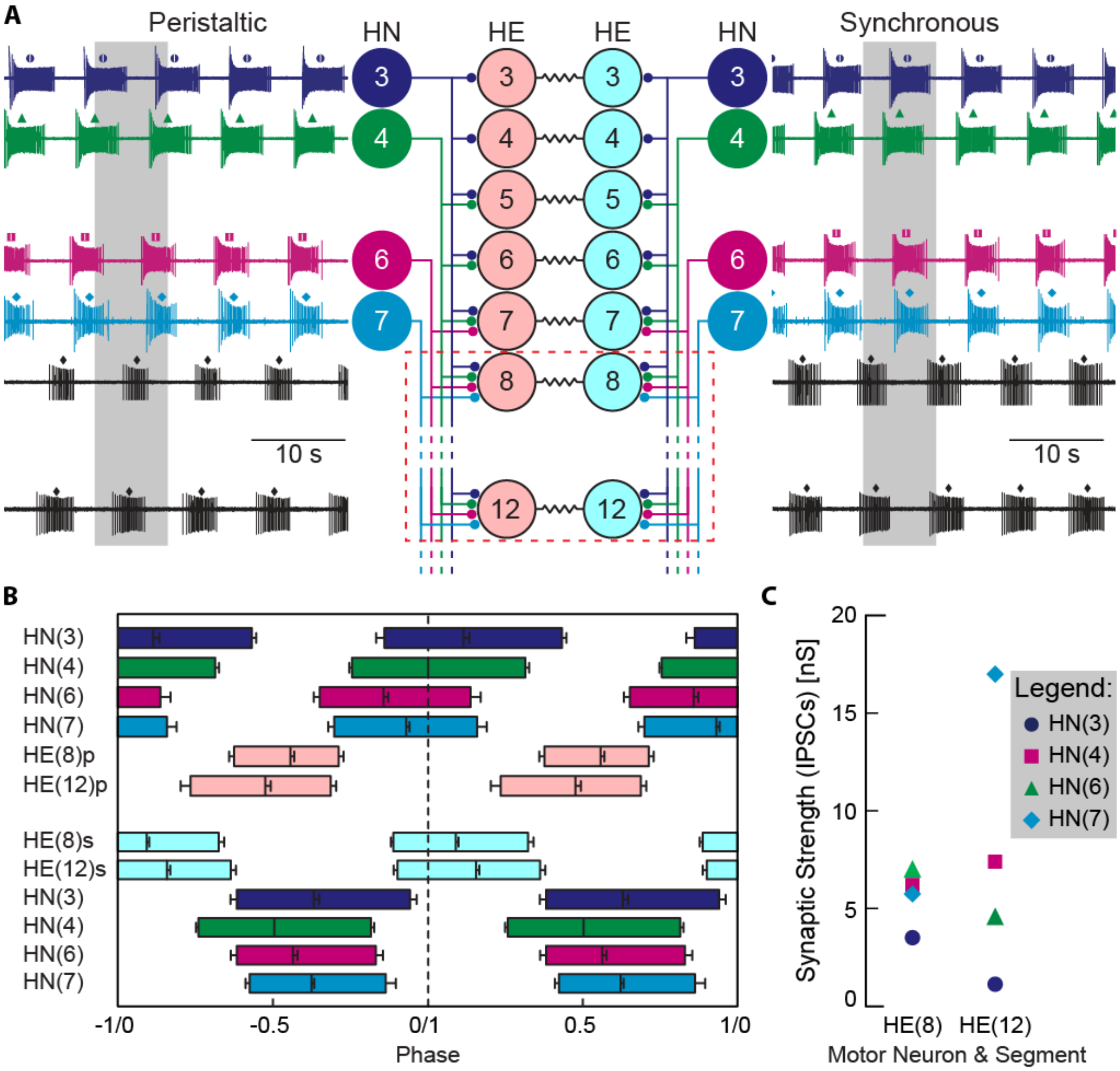

Figure 3.1 Front leech heart motor neuron circuit and input/output pattern

A. Simplified circuit diagram for heart (HE) motor neurons depicting the premotor heart (HN) interneurons (ganglia of origin indicated) and the synapses from the former to the latter. Adjacent to each neuron is a representative extracellular recording with the middle spike indicated by a small symbol above each burst. One period is indicated by the grey background bar. Connectivity between interneurons is not shown (for detail, see (Hill et al., 2002, 2003, Roffman et al., 2012)). Note that ipsilateral midbody motor neurons (e.g., HE(8) and HE(12) above, highlighted with the red broken line) receive the same complement of inputs.

B. Relative phasing of first, middle and last spikes in heart motor neurons and interneurons recorded from a single animal, a portion of which is shown in panel A, as reported by Norris (Norris et al., 2007b) and used previously in earlier modeling efforts (Wright and Calabrese, 2011a, b). Error bars indicate standard deviations. The peristaltic pattern exhibits a strong rear-to-front phase progression in both the interneurons and motor neurons, whereas the synchronous pattern exhibits a minimal phase progression. Note that the HE(8) synchronous (s) and peristaltic (p) motor neuron bursts are nearly perfectly out of phase, unlike the HE(12)p and HE(12)s motor neuron bursts which partially overlap.

C. Relative synaptic strength of synapses onto heart motor neurons calculated from spike-triggered averaged IPSCs. Adapted with permission from (Norris et al., 2007b).

Methods

We developed a multi-compartmental leech heart motor neuron model parameterized by the maximal conductance ($\bar{g}$) densities of voltage-gated membrane currents and the electrical synapse between the two neurons of each pair (Figure 3.2). We then used a multi-objective evolutionary algorithm to generate a large number of model instances, each defined by the specific parameter values. Each model instance was simultaneously simulated as four neurons in two pairs with the same parameter values, the heart motor neurons in ganglia 8 and 12 (HE(8) and HE(12)), and the resulting membrane voltage traces were evaluated with the quantitative fitness metrics detailed below. We then examined the distribution of model instances in parameter space, the sensitivity of fitness metrics to parameter perturbation, and the response to injected current of quantitatively good (i.e., within target ranges on our fitness metrics) model instances.

Simulation and Analysis Framework

All model instances were implemented in the general neural simulation system (GENESIS) version 2.3 (Bower et al., 1998), and were simulated with a time step of 0.05ms using the Crank-Nicolson (Crank and Nicolson, 1947) method of the Hines solver for all objects except the electrical coupling, which was solved with the exponential Euler solver. The resulting soma compartment membrane voltage was recorded with a time step of 0.5ms and then analyzed with a suite of custom MATLAB® functions to detect bursts and compute the fitness of each model instance (see Figure 3.3). The fitness values for all model instances in each generation were passed to a multi-objective evolutionary algorithm (Smolinski et al., 2008, Smolinski and Prinz, 2009a, b), which was implemented in C++ and unchanged except for being adapted to interact with our simulations. These three components were coordinated with Bash shell scripts. Although our framework could run on a desktop computer, we took advantage of its inherently parallel structure, which ensured that each model instance could be simulated and analyzed entirely in isolation, and conducted our evolutions on a high performance computing cluster (Ellipse, Emory IT, ~1024 nodes). The model and associated input/output files will be uploaded to ModelDB upon publication.

Figure 3.2 Heart motor neuron model

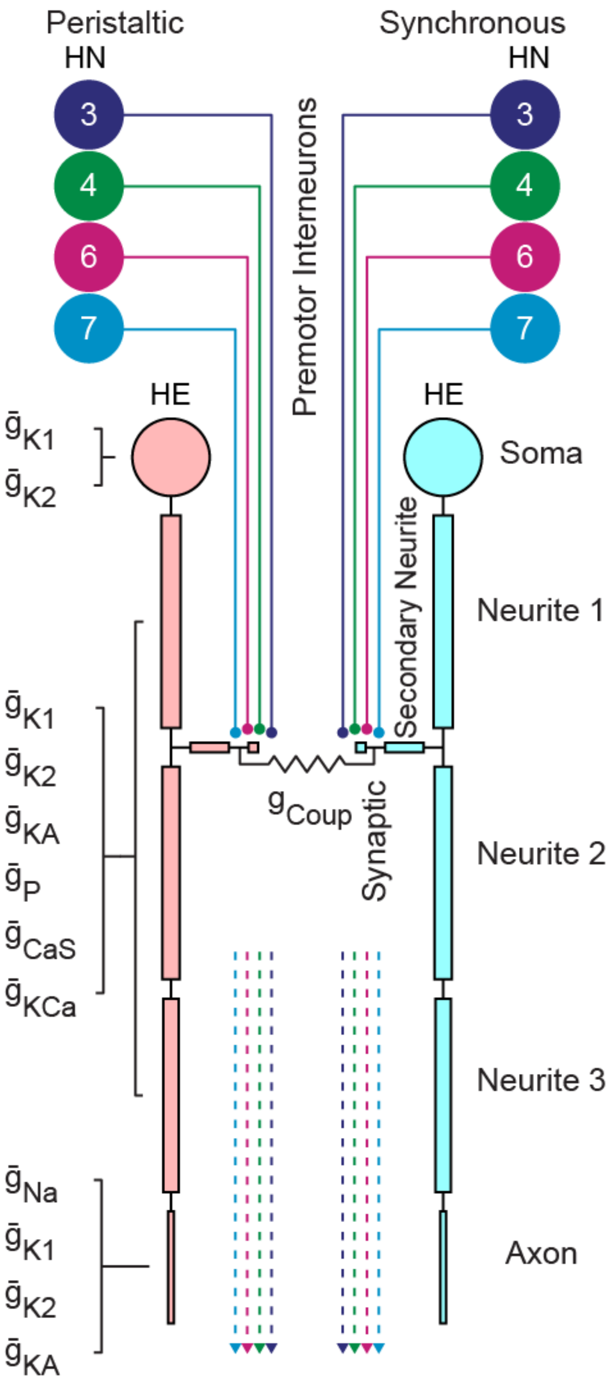

Figure 3.2 Heart motor neuron model

A pair of electrically coupled 7-compartment model heart motor neurons with their inhibitory inputs shown. The inputs to each model motor neuron were the prerecorded input spike times from the premotor interneurons (delayed based on the motor neuron pair's ganglion of origin), and the relative strength of the synapses. The soma, neurite and axon compartments contained active conductances in addition to the passive membrane capacitance and leak conductance, whereas the secondary neurite and synaptic compartments were only passive. The soma compartment contained a gK1 and gK2; the neurite compartments (Neurite 1, Neurite 2, Neurite 3) each contained gK1, gK2, gKA, gP, gCaS, and gKCa; and the axon compartment contained gNa, gK1, gK2, and gKA. The synaptic compartment contained synaptic elements and was electrically coupled (gcoup) to the contralateral heart motor neuron. An instance of the abstract model was defined by specific values for the maximal conductance ($\bar{g}$) density of each conductance shown above.

Figure 3.3 Fitness metrics used to quantitatively evaluate model output

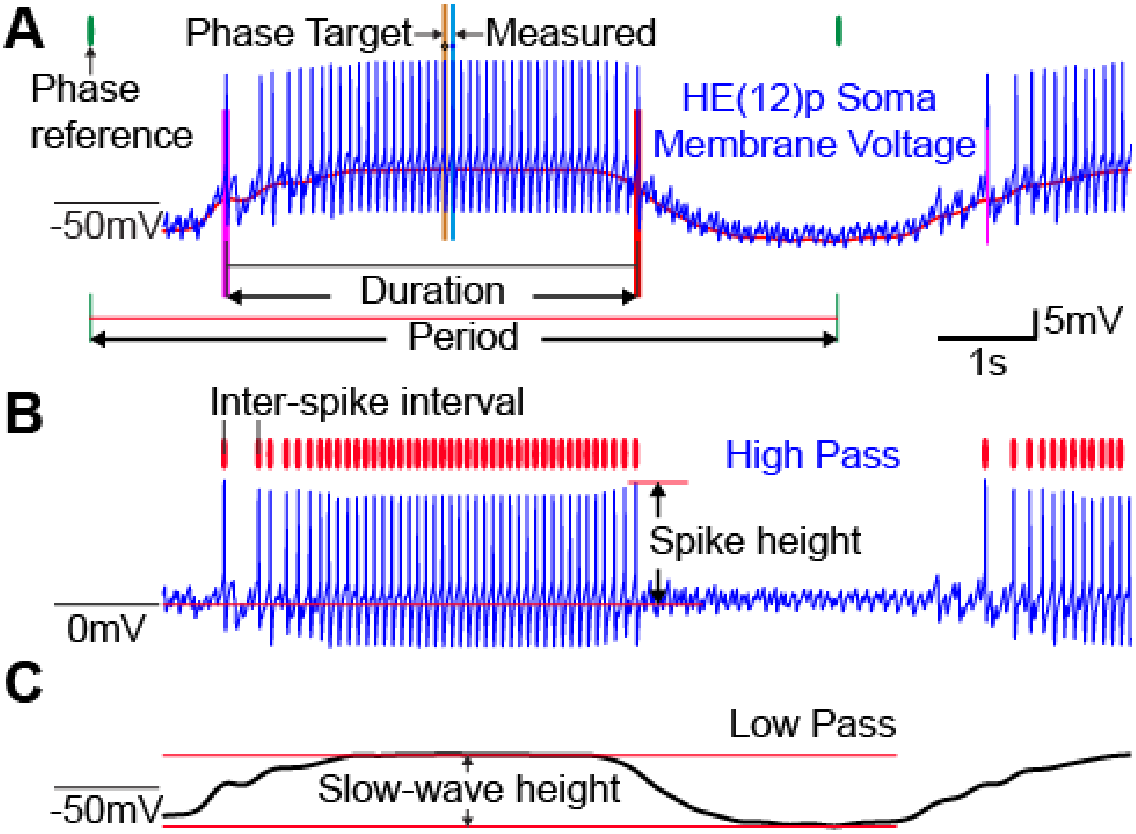

Figure 3.3 Fitness metrics used to quantitatively evaluate model output

The soma compartment membrane voltage was split into low pass and high pass components, spikes were identified, and 5 fitness metrics were calculated: phase, duty cycle, mean intraburst spike frequency, mean spike height, and slow-wave height.

A. The unfiltered soma compartment membrane voltage (blue trace) with the first spike (fuchsia vertical line) and last spike (red vertical line), phase reference (green vertical lines), phase target (black circle and ochre line), and measured phase (blue dot and topaz line), burst duration (black horizontal line), and period (red horizontal line) indicated. The low-pass trace shown in panel C is in red behind the primary trace. The relative phase of the middle spike was calculated with reference to the middle spike of the reference HN(4)p interneuron as shown in Figure 3.1. The duty cycle was calculated from the phase of the last spike minus the phase of the first spike. All phases were measured with reference to the HN(4)p middle spike.

B. High-pass filtered soma compartment membrane voltage (blue trace) with identified spikes (red vertical lines) and spike height indicated. Spike frequency is the inverse of the inter-spike interval within the identified burst. The spike height was defined as the value of the high pass trace at the peak of each spike within the burst. Both the spike height and spike frequency were averaged within each burst.

C. Low-pass filtered soma compartment membrane voltage (black trace) with slow-wave height defined as filtered voltage difference at the middle spike relative to the minimum voltage in the inter-burst region.

Heart motor neuron model

The heart motor neuron model constructed here using GENESIS 2.3 (Bower et al., 1998) consists of 7 isopotential compartments whose physical dimensions approximate the surface area found in adult leech heart motor neurons as estimated from confocal reconstructions and previously published morphology (Tolbert and Calabrese, 1985) as shown in Figure 3.2. In heart motor neurons, a single main neurite tapers from the soma through the ganglion and out into the periphery as an axon. From the main neurite in the ganglion emerge many secondary neurites that branch extensively and form the input regions of the neuron. We approximated the main neurite and axon using four distinct cylindrical compartments with diminishing diameters whose lengths were set to a maximum of 1/10 the passive electrotonic length constant. The most distal compartment represented the spike initiation zone and axon and is here called the axon compartment. Although there exist no experimental data specifying the exact spike initiation zone, it must be sufficiently distant so that spikes are relatively small when recorded in the soma, and we adjusted the total length of the neurite and axon compartments to achieve an attenuated spike height. The complex structure of the arbor of secondary neurites emerging from the main neurite was approximated by two linked compartments: a passive secondary neurite compartment linked between neurite compartments 1 and 2, and a distal synaptic compartment. Each compartment was linked through an axial resistance determined by its diameter and length to its parent compartment. We thus had a spherical soma compartment (diameter = 40μm), three neurite compartments (neurite 1 diameter = 10μm, length =

115µm; neurite 2 diameter = 9µm, length = 110µm; neurite 3 diameter = 8µm, length = 100µm), an axon compartment (diameter=3µm, length= 58µm), a secondary neurite compartment (diameter = 5µm, length = 20µm), and a synaptic compartment (diameter = 5µm, length = 5µm), see Table 1. The passive parameters were set to a specific membrane resistance of 1.1Ωm2, a leak reversal potential of -40mV, a specific axial resistance of 0.25Ω/m, and a specific capacitance of 0.02 F/m2, resulting in input resistances measured in the soma of ~70MΩ, which is within the input resistance range observed in the living system (Opdyke and Calabrese, 1995).

We then distributed both established conductances and a new calcium-sensitive potassium conductance according to our best estimate of their distribution while still minimizing the number of model parameters by only placing conductances where they were believed to be located and by constraining the neurite compartments to have the same conductance density (Opdyke and Calabrese, 1995, Tobin et al., 2006, Garcia et al., 2008). Each isopotential compartment was modeled in the Hodgkin-Huxley formalism with:

$$C\frac{dV_m}{dt} = -(I_{Na} + I_P + I_{KA} + I_{K1} + I_{K2} + I_{KCA} + I_{CaS} + I_{syn} + I_{coup} + I_{leak} + I_{axial} + I_{inj})$$

Where all active conductances were modeled as Hodgkin-Huxley style membrane conductances with the general formula:

$$I_{Na} = \overline{g}_{Na} m_{Na}^3 h_{Na} (V_m - E_{Na})$$

The specific formula for each membrane conductance is given in Table 2. Both m and h follow the form:

$$\frac{dm}{dt} = \alpha_m(V_m)(1-m) - \beta(V_m)(m)$$

Genesis 2.3 uses pre-calculated tables for α and β during the simulation, where both α and β were calculated from steady state (see Figure 3.4) and time constant curves by:

$$\tau(V_m) = \frac{1}{\alpha(V_m) + \beta(V_m)}$$

And

$$m_\infty(V_m) = \frac{\alpha(V_m)}{\alpha(V_m) + \beta(V_m)}$$

Where those curves (e.g., Figure 3.4) were specified for each conductance by curves given by:

$$m_\infty(C,D) = \frac{1}{1+e^{C(V_m-D)}}$$

And

$$\tau_m(A,B,C,D) = A + \frac{B}{1+e^{C(V_m-D)}}$$

Except for τhNa, for which h is given by:

$$\tau_{hNa}(A,B,C,D) = A + \frac{B}{1+e^{C(V_m - D)}} + \frac{0.01}{e^{300(V_m - 0.017)}}$$

Where A is the baseline value, B scale factor, C is the slope and D is the midpoint of the hyperbolic tangent curve. See Table 3 for the specific values of A, B, C and D for each conductance.

In addition to the established leech conductance models for gK1, gK2, gKA, gCaS, and gNa we incorporated, we added a calcium sensitive potassium conductance model based on the gK2 conductance with a right-shifted half activation, slower dynamics, and a saturating linear calcium gate (see Tables 2 and 3) to approximate previously published electrophysiological data (Opdyke and Calabrese, 1995, Ivanov and Calabrese, 2003). To activate the calcium gate of this channel, we added a calcium conductance feeding a calcium pool with a simple exponential decay to baseline (τ= 1.5s) linked to the gate. Earlier heart motor neuron models did not include gKCa or gCaS, even though gKCa and gCaS were known to be present (Opdyke and Calabrese, 1995). We included gKCa and gCaS not only to better replicate what is found in the living system, but because preliminary modeling suggested that they were capable of altering burst characteristics.

Electrophysiological experiments have provided evidence for the rough distribution of established currents with respect to the compartments used to model these motor neurons. The spikes are small when recorded in the soma, indicating that they are initiated in some distal compartment and are not regenerated or sustained by fast sodium conductances in compartments close to the soma, and thus the axon compartment is the only one which contains a fast sodium conductance, gNa. The axon compartment also contains potassium conductances that underlie spike generation and pacing, gK1, gK2, and gKA. In the model, the neurite compartments act as an integrating region, combining the inhibitory input from the premotor interneurons and its membrane properties to suppress or drive spiking in the adjacent axon compartment. The 3 neurite compartments each contained all active conductances except gNa: the purely voltage gated potassium conductances gK1, gK2, and gKA, a calcium and voltage gated potassium conductance, gKCa, a slowly inactivating calcium conductance, gCaS, and a persistent sodium conductance, gP. Since these motor neurons were known to express high levels of outward currents as measured from the soma (Opdyke and Calabrese, 1995), the model soma compartment contains the two potassium conductances likely to be active during normal activity, gK1 and gK2. These conductances represent the product of the maximal conductance density of each and the surface area of the compartment in which they were contained. The synaptic compartment and the secondary neurite which connects it to the first neurite compartment were both modeled as passive compartments, but the synaptic compartment contained 4 spike-mediated synapse modules, described in detail below, one for each ipsilateral premotor heart interneuron. The synaptic compartment also contained an electrical junction connecting to the contralateral heart motor neuron, gCoup. The electrical junction current flow was filtered by a simple rc filter with a time constant of 0.02s applied to the synaptic compartment voltage of each HE neuron of the pair:

$$V'_{m[\mathrm{t}]} = \alpha\, V_{m[\mathrm{t}-1]} + (1+\alpha)\, V'_{m[\mathrm{t}-1]}$$
$$\text{where } \alpha = e^{\frac{\Delta t}{\tau}} \text{ for timestep } \Delta t$$

To keep the number of parameters allowed to vary in the evolutionary algorithm to a minimum, the three neurite compartments had the same conductance densities. Each instance of this heart motor neuron model was thus defined by 13 specific maximal conductance density values: the soma ḡK1, soma ḡK2, neurite ḡK1, neurite ḡK2, neurite ḡKA, neurite ḡP, neurite ḡCaS, neurite ḡKCa, gCoup, axon ḡNa, axon ḡK1, axon ḡK2, and axon ḡKA (see table 1).

An instance of the heart motor neuron model was hand tuned as a passive model to achieve experimentally determined membrane properties, specifically the time constant and input resistance as determined by a current step injected into the soma compartment. The active membrane conductances were then distributed to the appropriate compartments and their maximal conductances tuned so as to achieve a qualitatively good soma membrane voltage waveform comprising a duty cycle, spike frequency, spike height and slow wave height in the biological range. The initial hand tuned model generated above did not achieve the target phase within the same tight constraints used in the evolutionary algorithm, but did achieve the target range for the other fitness metrics. The evolutionary algorithm was allowed to explore parameter values from 0.1 to 4.9 times those hand tuned values (step size of 0.1) with the exception of gCoup, which was limited to less than 3 times the baseline value and used a step size of 0.06, because the initial model value was already at the upper end of what had been observed experimentally, see Table 1 for the maximum allowed value.

Members of each pair of HE neurons, one pair per ganglion, were electrically coupled via gCoup. The input pattern contained a temporal pattern (i.e., the spike times for all 8 premotor interneurons, 4 in each coordination mode) and a synaptic weight profile for each pair of heart motor neurons, and was associated with corresponding target values on the fitness metrics described below.

Input/output dataset

We chose an input/output dataset from input/output datasets extensively described in previous reports (Norris et al., 2006, Norris et al., 2007b, Wright and Calabrese, 2011b). Briefly, these datasets consisted of simultaneous extracellular (loose cell-attached patch) recordings from all ipsilateral premotor heart interneurons (HN(3), HN(4), HN(6), and HN(7)) in addition to HE(8) and HE(12) motor neurons, a portion of which is shown in Figure 3.1. These extracellular recordings were long enough to include both the peristaltic and synchronous modes. The interneuron to motor neuron synaptic weights were subsequently measured by dSEVC (discontinuous single electrode voltage clamp) of the heart motor neurons while still recording from the 4 ipsilateral interneurons. From 12 individual animals thus analyzed, we chose 1 input/output dataset with which to develop and examine this model. The two coordination modes were aligned to produce a complete bilateral input spike time pattern with experimentally observed phasing between the two sides (0.51) (Norris et al., 2006) and were constructed by aligning the 12 synchronous and 12 peristaltic bursts. When used in our simulations, this input pattern was preceded by a 15s silent period to allow model parameters to settle and to ensure that models were tonically active in the absence of synaptic input, extending the total simulation time to 105s. From each motor neuron we calculated fitness metrics by analyzing the 10 bursts which were both preceded and followed by synaptic input for both neurons in each pair. The output targets for phase, duty cycle and spike frequency were those metrics measured in the recorded output pattern and then averaged across the bursts. Slow-wave height and spike height require unclamped intracellular recordings which were not available for every motor neuron, so these targets were taken from established average values from leech heart motor neurons recorded in other experiments. In aggregate, the input/output dataset consisted of spike times and synaptic weight profiles for the 4 premotor interneurons in each coordination mode and fitness targets for the spike height (15mV), slow-wave height (10mV), spike frequency (7.37Hz), peristaltic phase (HE(8):0.56, HE(12):0.48), peristaltic duty cycle (HE(8):0.34, HE(12):0.46), synchronous phase (HE(8):0.08, HE(12):0.11), and synchronous duty cycle (HE(8):0.44, HE(12):0.46.

Inhibitory input synapse model

The inhibitory input synapse model was based on a previously described spike-mediated synapse model (Garcia et al., 2008, Wright and Calabrese, 2011b) with modifications to more closely match the observed conductance waveform of synaptic events in heart motor neurons. This synapse model consisted of two spike-triggered double exponentials, one with a shorter fall time (τ_{fall}= 12.5ms, τ_{rise}=4ms) and the other with a longer fall time (τ_{fall}=150ms, τ_{rise}=4ms), with the slower component's maximum conductance set to 0.33 times the faster component ($\bar{g}_{slow} = 0.33\ \bar{g}_{fast}$), resulting in a combined waveform which approximated the shape of inhibitory post-synaptic currents (IPSCs) observed in the living system, which has both spike mediated and graded components (Norris et al., 2007a). Thus for each spike we have the normalized spike-triggered waveform given by:

$$f_{Syn}(t) = \left(\frac{e^{\frac{-t}{\tau_{fall}}} - e^{\frac{-t}{\tau_{rise_1}}}}{e^{\frac{-t_{peak_1}}{\tau_{fall}}} - e^{\frac{-t_{peak_1}}{\tau_{rise_1}}}} + 0.33 \frac{e^{\frac{-t}{\tau_{fall}}} - e^{\frac{-t}{\tau_{rise_1}}}}{e^{\frac{-t_{peak_2}}{\tau_{fall}}} - e^{\frac{-t_{peak_2}}{\tau_{rise_1}}}} \right),$$

$$\text{where } t_{peak_n} = \frac{\tau_{fall}\tau_{rise_n} \ln\left(\frac{\tau_{fall}}{\tau_{rise_n}}\right)}{\tau_{fall} - \tau_{rise_n}}$$

The synaptic reversal potential was set to -62.5mV as in prior models (Garcia et al., 2008, Wright and Calabrese, 2011a, b) and as measured in the living system (Angstadt and Calabrese, 1991).The maximal conductances were initially the unscaled relative strengths reported in (Norris et al., 2007a) but were adjusted with scaling factor (σ) to produce a combined inhibitory input that more closely matched that observed in the living system and was capable of sculpting heart motor neuron bursts in our hand-tuned model as in previous models (Garcia et al., 2008). Furthermore, in the living system the inhibitory synapses from HN onto HE neurons exhibit intraburst synaptic plasticity: IPSCs are initially quite small and then increase to a plateau level before declining towards the end of each presynaptic burst (Norris et al., 2007a). This plasticity is believed to be due to presynaptic Ca^{2+} accumulation as spike-mediated synapses in the leech heartbeat system are known to be modulated by presynaptic Ca^{2+} entry through LVA Ca channels driven by the slow wave of presynaptic membrane voltage in heart interneurons (Ivanov and Calabrese, 2003). Both presynaptic membrane voltage and free Ca^{2+}levels are experimentally inaccessible at present, so we approximated modulation by presynaptic background calcium with a pre-calculated modulation waveform that approximated this rising and falling behavior with an exponential rise from a factor of 0.01 to 1 for 90% of the burst duration and then an exponential decay for the final 10%, similar to previous heart motor neuron models (Garcia et al., 2008, Wright and Calabrese, 2011a, b). For each presynaptic burst (l) starting at time t_0 we have the waveform given by:

$$M_{\mathrm{HN}(\#),\mathrm{l}}(\mathrm{t}) = \begin{cases} 1 - 0.99e^{\frac{-(t-t_{s0})}{\tau}} & t \leq 90\% burstlength \\ 0.01 + 0.99e^{\frac{-(t-t_{s0})}{\tau}} & t > 90\% burstlength \end{cases}$$

For each prerecorded input (each HN spike train), we calculated the appropriate rise- and fall-time constants from the average time for the first and final 5 spikes of each burst, for rise- and fall-time constants, respectively, for each premotor interneuron. The synaptic conductance waveforms summate and were weighted by the relative synaptic weight measured in the living system for each HE neuron HN neuron pair, $\bar{g}_{Syn[\mathrm{HN}(\#),\mathrm{HE}(\#)]}$, the modulation waveform $M_{\mathrm{HN}(\#)}(t)$, and the scaling factor σ and were combined for each HE motor neuron modeled giving:

$$I_{Syn[\mathrm{HE}(\#)]}\left(t,V_m\right)=\sigma\left(V_m-E_{syn}\right)\sum_{HN(\#)}M_{\mathrm{HN}(\#)}(t)\bar{g}_{Syn[\mathrm{HN}(\#),\mathrm{HE}(\#)]}\sum_{n}f_{Syn}(t-t_n)$$

Thus the complete input pattern delivered to each model instance consisted of a modulation waveform and a train of spikes for each premotor interneuron. These were delayed with a fixed conduction delay of 20ms per segment (the delay from ganglion 8 to 12 was thus 80ms).

Figure 3.4 Steady state activation and inactivation curves for voltage-gated conductances

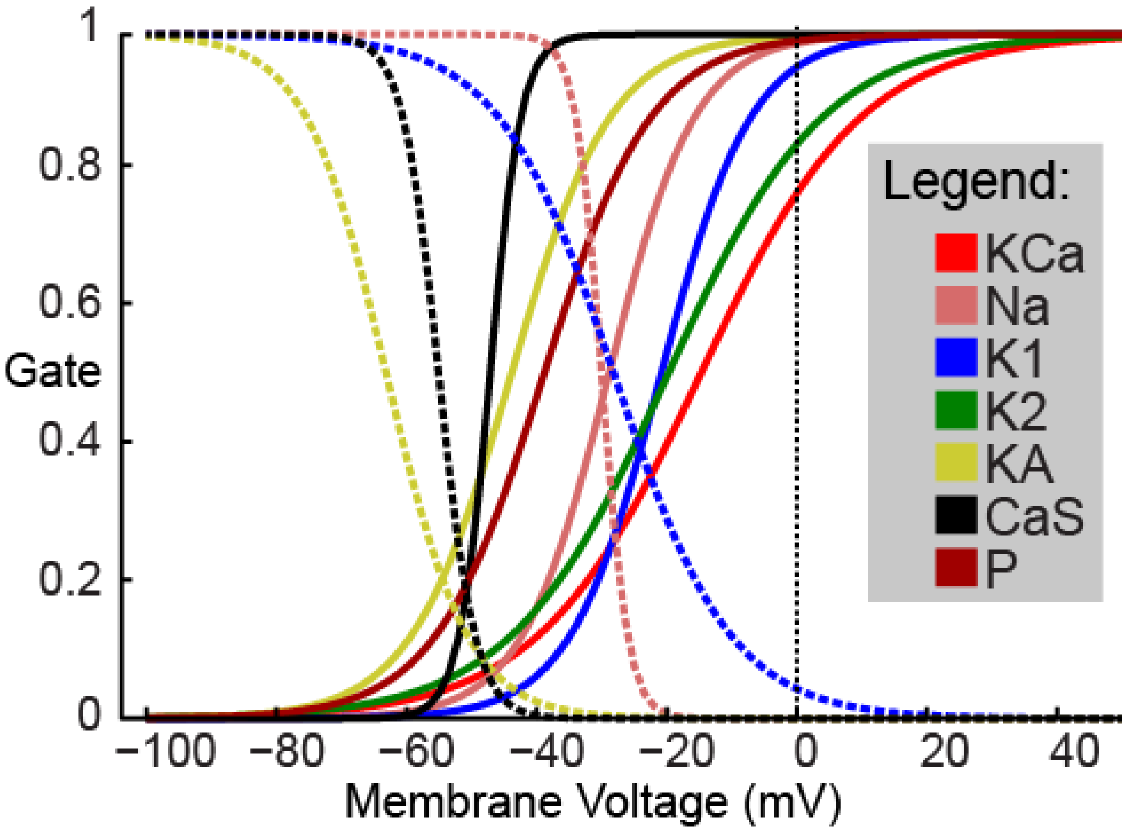

Figure 3.4 Steady state activation and inactivation curves for voltage-gated conductances

The activation and inactivation gating variables for each of the 7 active membrane conductances used are shown. Solid lines represent activation curves and the dotted lines represent inactivation curves. All conductances except the calcium sensitive potassium conductance have been used in previous heartbeat system models

(Hill et al., 2002, Garcia et al., 2008)

Fitness metrics:

Our fitness metrics comprised measures of output attributes that correspond to canonical characteristics of heart motor neuron activity and the overall fictive motor pattern produced. Thus, to evaluate each model instance quantitatively, we used 5 metrics for each neuron being evaluated: phase, duty cycle, intraburst-spike frequency, slow-wave amplitude, and spike height (see Figure 3.3). Each of these metrics was calculated for every burst of each motor neuron simulated and the resulting values for each burst were then averaged across all bursts for each motor neuron. Because the neural activity we were examining was rhythmic and we aimed to describe the relative phase relationships among the various constituent neurons of the system, we had to select a phase reference, an event within each cycle to define as 0 phase. We used the HN(4) interneuron in the peristaltic mode for this phase reference as in previous reports, e.g. (Maranto and Calabrese, 1984, Norris et al., 2007b). The period of each cycle was defined as the time between the middle spikes, with the middle spike defined as the median-spike time of subsequent bursts of the HN(4) interneuron in the peristaltic mode as in (Norris et al., 2007b). The phase of each neuron was defined by the timing of the middle spike of its burst relative to the associated middle spike of the HE(4) interneuron in the peristaltic mode divided by the associated period of the same. The duty cycle of each neuron was defined as the time between the first and last spikes of each burst divided by the associated period. Intraburst spike frequency was calculated for all interspike intervals within detected bursts, thus excluding spurious spikes between detected bursts, and was averaged within each burst to produce that burst's mean spike frequency. The soma compartment membrane voltage was split into high- and low-pass components using a low-pass filter (1001 point zero-phase FIR filter with a -10dB cutoff at 1.794Hz) such that the high-pass component was the remainder when the low-pass component was subtracted from the original waveform. The slow-wave height was the value of the low-pass filtered soma compartment membrane voltage at the trough of the inhibited portion of the cycle minus the value at the middle spike of the burst. Finally, the spike height was the value of the high-pass filtered soma compartment membrane voltage at the peak of each spike within a burst and, as with spike frequency, was averaged within each burst. These 20 values, 5 for each of the 4 simulated neurons, were combined to form 11 metrics that represent the performance of the pairs of HE(8) and HE(12) motor neurons by breaking them into two groups: first, the phase and duty cycle for each of the 4 motor neurons, and second, the basic fitness metrics (the mean intraburst spike frequency, slow wave amplitude, and spike height) which did not differ greatly between each of the 4 motor neurons in each simulation and were averaged across the 4 motor neurons. All model instances had to achieve the target range on the basic fitness metrics to be considered functional. The multi-objective evolutionary algorithm selected the best models independently on each of these metrics, so by combining redundant fitness metrics we avoided overemphasis on model instances which only achieved the target value for one of the basic fitness metrics. If a model instance produced an excellent spike frequency, but was otherwise poor, it would be represented in four fitness metrics if they were not collapsed into one. Since we cared most about phase and duty cycle, and unlike the basic fitness metrics these varied greatly between the 4 motor neurons in each simulation, we did not want such overrepresentation. The target and error threshold for each fitness metric are given in Table 3.4

Burst isolation

Our fitness metrics presume the identification of bursts, and this had to be accomplished in an automated fashion so that an unsupervised algorithm, such as the multi-objective evolutionary algorithm, could be used. We defined bursts as a group of 5 or more sequential spikes between which the interspike interval (ISI) was always less than the minimum interburst interval (IBI). For this investigation, the burst detection algorithm initially set the minimum IBI to 1s. Unfortunately, many model instances did not have clearly defined bursts—instead of a clear separation between bursts evident in the cessation of spiking activity for more than 1s, these model instances merely exhibited a reduction in spike frequency. Although these model instances were almost uniformly deficient on many metrics, we still had to calculate their fitness where possible. In order to calculate the fitness metrics, however, bursts first had to be identified. To do so, the minimum IBI was reduced by a factor of 0.25 until the number of bursts detected matched the number expected for the corresponding input pattern or, failing that, the minimum IBI fell below 50ms (i.e. below the minimum ISI typically found during normal activity in the living system). When bursts could not be isolated, or where spikes were not detected, the model instance was considered to be bad or failed. Model instances which produced bursts that could be isolated were considered to be at least quasi-functional (our fitness metrics could at least be calculated), even if most model instances did not produce output within the target ranges.

Multi-objective evolutionary algorithm (MOEA)

Model instances were generated and selected by a multi-objective evolutionary algorithm (MOEA) previously used to produce crustacean stomatogastric neuron model instances (Smolinski et al., 2008, Smolinski and Prinz, 2009a, b). Briefly, the first generation was randomized and subsequent generations were bred from exemplars selected independently on each individual fitness metric, with a small amount of random mutation. For example, a model that had an excellent HE(8) peristaltic mode phase (i.e., the best of the present and past generations), but which was unsatisfactory on all other fitness metrics, contributed to the subsequent generation. Since we did not need to create a weighting between the fitness metrics due to the structure of the MOEA, we obviated the complexity and bias that this may produce at the cost of possibly carrying along some poor model instances. The influence of this potential problem was generally negligible because models which were amongst the best on at least one metric were, by definition, satisfactory in some way. Due to the sparse sampling of parameter space (approximately 1e6 models simulated out of the roughly 7e21 model instances that would be required for a brute force approach with the same granularity) and dependence on the random seed for the initial generation, breeding, and mutations, we initiated and combined model instances from a series of 5 evolutions. Model instances which were previously simulated, either in a previous generation or evolution, were not resimulated or reanalyzed, so as to optimize usage of computational resources, but were still treated as if they were by the evolutionary algorithm by reading the previously calculated fitness values.

Partial Correlations

We evaluated the linear correlational relationships between parameters by examining the partial correlations (ρ) between each pair of parameters (Fisher, 1924). Examining the partial correlation allowed us to evaluate the relationship between parameters while controlling with a general linear model (LM) for the remaining parameters. I.e., for parameters X and Y and remaining parameters Z, we calculated the Pearson's r between residuals X' and Y', that is $r(X', Y')$, where $X'=X-LM(X,Z)$ and $Y'=Y-LM(Y,Z)$, alternatively expressed as $r((X, Y)|Z)$, the correlation between X and Y given Z. We set the p threshold conservatively with a Bonferroni correction for multiple comparisons to 3.2e-4 and dropped parameters which had at least one p value above this threshold. We then recalculated ρ for the remaining parameters that had all p values below the threshold, leaving us with neurite $\bar{g}$K1, $\bar{g}$K2, $\bar{g}$KA, $\bar{g}$P, $\bar{g}$CaS and axonal $\bar{g}$KA, $\bar{g}$K2, and $\bar{g}$Na. The four parameters which were dropped from this comparison, soma $\bar{g}$K1, soma $\bar{g}$K2, gCoup and neurite $\bar{g}$KCa, only had one moderate or stronger partial correlation (where $|\rho|>0.5$), that between $\bar{g}$CaS and $\bar{g}$KCa. Dropping these four parameters did not substantively influence the recalculation of ρ for the remaining parameters.

Parameter Variation:

We initially defined three sets of model instances: set A, which met all HE(12) and basic metrics targets, set B, which met all HE(8) and basic metrics targets, and set C, which met all our fitness targets. This latter set C thus contains the 431 model instances which were successful as both HE(8) and HE(12) motor neurons. Since there were too many model instances in sets A and B, approximately 39,000 and 4,500, respectively, to perform parameter variation on all model instances in these groups, we selected a randomly chosen subset of set A and set B with 500 model instances for each. The two subsets were selected to ensure that all sets were mutually exclusive, so subset A contained only models which failed on at least one HE(8) metric and subset B contains models which failed on at least one HE(12) metric. Thus, no model instance appeared in more than one subset and 1431 model instances were examined with parameter variation. Each neurite and axon conductance parameter, plus g_{Coup}, were systematically varied by ± 50% and ±25%, and then evaluated on our fitness metrics.

Ramp Current Injection

We injected a 5s triangular ramp of current into the soma compartment of the same subsets used for parameter variation (subset A, subset B, set C). After a 10s baseline with no current injected, a 2.5s long ramp from 0nA to -0.5nA and then a 2.5s long ramp from -0.5nA to 0nA was injected. This was done in the absence of input from the premotor interneurons but with coupling present. We examined and then calculated the change in spike frequency with respect to injected current as well as the last spike time of the downward portion and first spike time of the upward portion relative to time of maximum injected current. We then normalized the resulting F/I curves to the maximal spike frequency observed to better visualize the difference between the downward and upward portion of the ramp injection and calculated the best fit line for the first and second half of each ramp with robust least squares (bisquare weighting) regression. We then analyzed how the first and last spikes differed between the three subsets with a one-way MANOVA and followed up with Bonferroni post-hoc tests.

Table 3.1 Dimensions and upper bounds of conductance densities allowed in the MOEA

Compartment	Length (µm)	Diameter (µm)	Na (S/m^2)	P (S/m^2)	CaS (S/m^2)	K1 (S/m^2)	K2 (S/m^2)	KA (S/m^2)	KCa (S/m^2)	Coup (nS)
Soma	40	40				25	25			
Neurite 1	115	10		9.5	0.5	375	375	50	50	
Neurite 2	110	9		9.5	0.5	375	375	50	50	
Neurite 3	100	8		9.5	0.5	375	375	50	50	
Secondary Neurite	20	5								
Synaptic	5	5								10
Axon	58	3	3500			500	500	750		

Conductance densities are in Siemens per square meter (S/m^2) except for Coup, which is the upper bound of the static conductance for the electrical coupling in nS.

Table 3.2 Hodgkin-Huxley style membrane conductance formulae

Conductance	Formula
Leak	$I_{leak} = g_{leak_j}\,(V_m - E_{leak})$
Na	$I_{Na} = \overline{g}_{Na} m_{Na}^{3} h_{Na} (V_m - E_{Na})$
P	$I_P = \overline{g}_P m_P (V_m - E_{Na})$
CaS	$I_{CaS} = \overline{g}_{CaS} m_{CaS}^{2} h_{CaS} (V_m - E_{Ca})$
K1	$I_{K1} = \overline{g}_{K1} m_{K1}^{2} h_{K1} (V_m - E_K)$
K2	$I_{K2} = \overline{g}_{K2} m_{K2}^{2} (V_m - E_K)$
KA	$I_{KA} = \overline{g}_{KA} m_{KA}^{3} h_{KA} (V_m - E_K)$
KCa	$I_{KCa} = \overline{g}_{KCa} \Gamma_{KCa} m_{KCa}^{2} (V_m - E_K)$ $\Gamma_{K_{Ca}} = \begin{cases} 0, & if\,[Ca] < [Ca]_{\min} \\ \frac{1}{[Ca]_{\max} - [Ca]_0}\left([Ca] - [Ca]_0\right), & if\,[Ca]_{\min} \le [Ca] \le [Ca]_{\max} \\ 1, & if\,[Ca] > [Ca]_{\max} \end{cases}$ $Where\ [Ca]_{\min} = 60e-9,\ [Ca]_{\max} = 15e-8$

Table 3.3 Voltage-gated conductance model parameter values

Name	E_{rev}	m_∞		h_∞		m_T				h_T			
		C (1/mV) (slope)	D (mV) ($V_{1/2}$)	C (1/mV) (slope)	D (mV) ($V_{1/2}$)	A (s) (T_{min})	B (s) (T_{max})	C (1/mV) (slope)	D (mV) ($V_{1/2}$)	A (s) (T_{min})	B (s) (T_{max})	C (1/mV) (slope)	D (mV) ($V_{1/2}$)
Na	45	-150	-29	500	-30	0.0001	0			0.004	0.006	-150	-28
P	45	-120	-39			0.01	0.2	400	-57				
CaS	135	-420	-47.2	360	-55	0.005	0.134	-400	-48.7	0.2	8	-250	-43
K1	70	-143	-21	111	-28	0.001	0.011	150	-16	0.5	0.2	-143	-13
K2	70	-83	-20			0.057	0.043	200	-35				
KA	70	-130	-44	160	-63	0.005	0.011	200	-30	0.026	0.0085	-300	-55
KCa	70	-80	-15			0.2	0						

Table 3.4 Targets, error thresholds and the mean, minimum, maximum, and standard deviation of set C fitness values for each fitness metric

Fitness metric	Target	Max Error	Mean	Min	Max	Std
HE(8)p phase	0.556	0.03	0.5288	0.526	0.5369	0.002
HE(8)p duty	0.337	0.1	0.3948	0.3602	0.4161	0.0094
HE(8)s phase	0.077	0.03	0.1054	0.0995	0.107	0.0013
HE(8)s duty	0.436	0.1	0.4752	0.4503	0.4932	0.0085
HE(12)p phase	0.475	0.03	0.482	0.4714	0.4961	0.0042
HE(12)p duty	0.452	0.1	0.5341	0.4814	0.552	0.0132
HE(12)s phase	0.143	0.03	0.1162	0.113	0.1227	0.0021
HE(12)s duty	0.462	0.1	0.5421	0.506	0.5586	0.0084
Spike frequency (Hz)	7.3682	7	9.6344	5.7768	14.365	1.8715
Spike height (mV)	15	7.5	19.0846	13.0818	22.4996	2.0668
Slow wave height (mV)	10	5	11.6903	7.6234	14.8884	1.1506

Results

Can we produce key functional characteristics of living heart motor neurons in a model?

In this study, we successfully created large sets of model instances which replicated, within reasonable tolerances, important functional characteristics of HE(8) and HE(12) motor neurons in the leech heartbeat system: the phase, duty cycle, spike frequency, soma spike height and soma slow-wave height (see Figure 3.3 and Figure 3.5). Out of the total of about 700,000 model instances which were simulated across the multiple evolutions, only about 66% produced bursts that could be analyzed, so the range of parameter values we covered was large enough to include regions of parameter space which do not support functional model instances. There were many model instances that achieved all metrics for a given motor neuron (HE(8) or HE(12)) but for only one of the two input modes (peristaltic or synchronous) but not both. These instances cannot be considered functional because the living motor neurons produced both output patterns used as targets (Norris et al., 2011). Of the ~500,000 quasi-functional instances that could be analyzed, 8% were functional HE(12) model instances (set A), just under 1% were functional HE(8) models (set B), and about 0.06% were within the target range for all metrics (set C). Approximately 10% of good HE(8) model instances were able to achieve all target ranges, whereas only 1% of good HE(12) model instances did so. These observations suggest that the ability of the model to produce the desired HE(8) activity put more stringent constraints on parameters than did the HE(12) activity, but that if a model instance could achieve the desired HE(8) activity then it was also likely to achieve the desired HE(12) activity.

The model instances in set C were by definition quantitatively able to replicate the pattern observed in the living system. Furthermore, the soma membrane voltage waveform qualitatively resembled that recorded from HE motor neurons in the living system. We thus produced a varied set of model instances that appear to be a good representation of HE motor neurons with which to investigate the distribution of and relationship between maximal conductance parameters.

Figure 3.5 Proportions of model instances, depicted as Venn diagrams, falling within target ranges of fitness metrics.

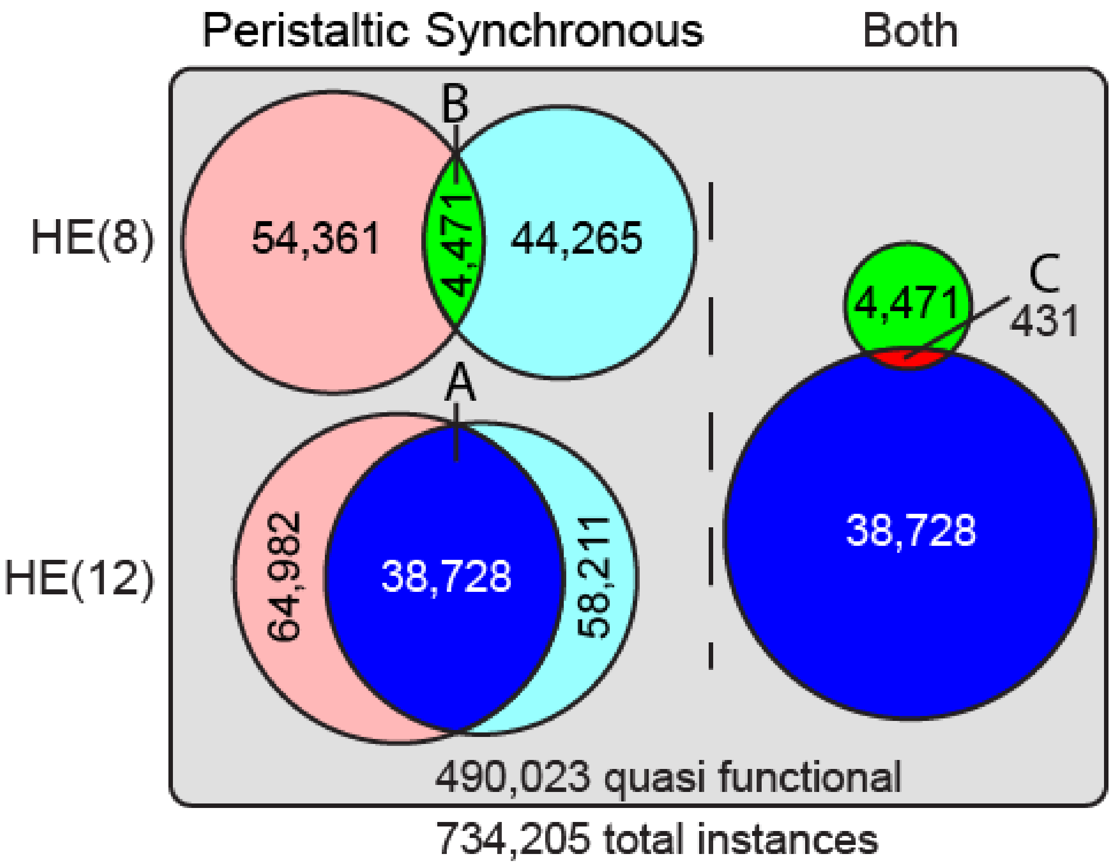

Figure 3.5 Proportions of model instances, depicted as Venn diagrams, falling within target ranges of fitness metrics.

Out of a total of 734,205 model instances which were simulated, 490,023 were at least quasi-functional. The left hand column of Venn diagrams shows the model instances which were capable of producing not only basic fitness metrics (average spike frequency, spike height, slow-wave height) but also the proper phase for the peristaltic or synchronous mode in the indicated heart motor neuron. For example, there were 54,361 models which produced a phase and duty cycle within an acceptable deviation from the target for the HE(8) motor neuron with the peristaltic input pattern, but only 4,471 of these also produced the correct activity with the synchronous input pattern. 431 instances produced output which was within the target range for all metrics, i.e. they produced the target output with all four input patterns: HE(8)p, HE(8)s, HE(12)p and HE(12)s. Three sets were used in subsequent analyses based on the targets they achieved in addition to the basic metrics: set A (blue), the instances which achieved output within the target range for the HE(12) metrics; set B (green), HE(8) metrics; and set C (red), the intersection of sets A and B.

What are the roles of the conductances?

The voltage-gated ionic currents, along with passive leak current, synaptic input, coupling, axial current and capacitive current, interact through their influence and dependence on the membrane voltage in complex ways. Figure 3.6 shows examples of neurite current flows for two instances of a HE(12) motor neuron from set C, where Figure 3.6A is a typical model instance and Figure 3.6B is an extreme case which is dominated by I_P and I_{K2} with all other active currents small. The dominant feature of our model is the rhythmic barrages of inhibitory synaptic currents that punctuate the normal tonic activity of the model motor. As we can see from inspection of the individual ionic currents, the currents contributed to the model neuron's activity pattern as generally expected, but I_{KA} in the neurite was present throughout the burst and during inhibition rather than just between spikes. We examined the currents during three regions of the cycle: during the inhibited portion, during the burst, and during the transitions between inhibition and bursting.

During inhibition, I_{CaS}, I_{K1}, and I_{KCa} were not activated, but I_p, I_{K2}, and I_{KA} were present. The primary influence these currents had was shifting the baseline membrane voltage according to the size of I_P relative to I_{K2} and I_{KA}. In the exemplary model instances shown in Figure 3.6, the slow-wave was smaller in the case shown where I_p was predominantly opposed by I_{K2}, and I_p remained more activated during inhibition than I_{K2}. In the case where I_p was predominantly opposed by I_{KA}, the slow-wave was larger. The baseline currents, especially the balance between I_{K2} or I_{KA} and I_P, were critical for these model instances to spike tonically when they were not inhibited and thus to form recognizable bursts. If there was insufficient I_P, or if it was opposed by too much I_{K2} or I_{KA}, then the model instance was not sufficiently excitable to spike tonically without extrinsic current. During bursts the model instances reached a stable tonic level of activity, although there was a small amount of spike frequency adaptation as I_{KCa} and I_{K2} increased throughout the burst. The relative proportions of those baseline currents in the absence of inhibition strongly influenced the spike frequency, the duty cycle, and, to a lesser extent, the phase, as revealed more clearly in the sensitivity analysis below. The spike shape, especially the undershoot, was substantially determined by the faster currents I_{KA} and I_{K1}, and model instances with low levels of those currents had less substantial undershoots.

At the beginning and end of inhibitory barrages, we saw the voltage-sensitive dynamics of these currents come into play. At the end of an inhibitory barrage, I_{KCa} was almost totally absent, but I_{KA} and I_{K2} quickly began to activate more fully, as did I_P. I_P quickly rose to its baseline level, as did I_{KA}, whereas I_{K2} took slightly longer to reach its baseline level, resulting in an earlier first spike in Figure 3.6B. The net result of the remaining synaptic inhibition and the further activation of these outward currents was a buildup in spike frequency rather than an immediate jump to the maximal tonic spike frequency. At the onset of an inhibitory barrage, I_{KCa} had reached a steady baseline and contributed to lowering the spike frequency. The outward currents, especially I_{K2}, began to deactivate, which could prolong spiking. As we see in Figure 3.6B, the combination of deactivation and a reduced driving force resulted in less opposition to I_P and an additional spike, thus prolonging the burst. The dynamics of the currents as inhibition ends and begins had a primary effect on the first and last few spikes, respectively, and thus also the duty cycle. However, their influence on the first and last few seconds of spikes could also shift the phase of the burst. Although a few spikes at the beginning and end predominantly influenced the duty cycle, the phase tolerance was approximately 2 interspike intervals for the average spike frequency of model instances in set C (1.37 to 3.4 spikes, mean of 2.28), so it did not take many spikes to shift the phase outside the target range. We further explored the difference between the onset and termination of inhibition between model-instance sets with injected hyperpolarizing current ramps below.

Figure 3.6 Membrane currents and soma membrane potential in the neurite 2 compartment of two model instances

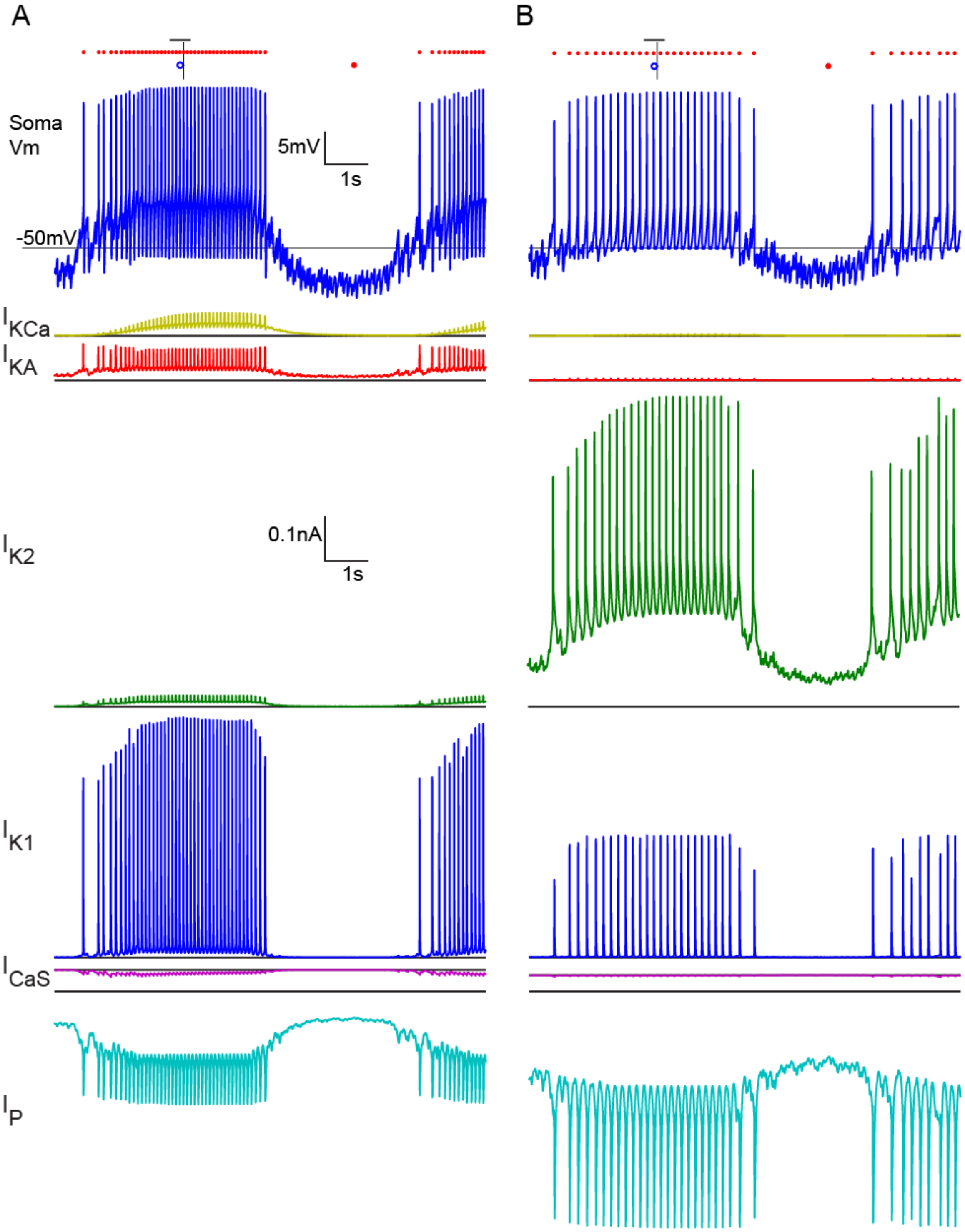

Figure 3.6

All actively gated currents (I_{K1}, I_{K2}, I_{KA}, I_P, I_{CaS}, I_{KCa}) in the neurite 2 compartment from two representative HE(12)p model instances. Traces are offset for clarity and the solid black line indicates the zero reference for the corresponding trace. On the soma voltage trace, small red circles indicate identified spikes, large red dots indicate the phase reference, blue circles indicates target phase, the short vertical black lines indicate measured phase and the horizontal black line indicates the target range.

A. Representative model instance from set C with low $\bar{g}_{K2}$ and $\bar{g}_P$ but $\bar{g}_{KA}$ in the middle of the allowable range selected.

B. Extreme model instance selected from set C with high $\bar{g}_{K2}$, near maximum $\bar{g}_P$ for set C, and low $\bar{g}_{KA}$.

How are the maximal conductances distributed in parameter space?

We next turned our attention to how the model instances were distributed in parameter space, or how the parameter values for successful model instances were related to each other given that the maximal conductances showed a large range of values. We found it difficult to directly visualize the potential interactions between parameters when considering the distribution of model instances represented as points in the full 13 dimensional parameter space, so we considered each pair of conductances one at a time. To do so, we examined the 2d projection of the acceptable model instances from sets A, B and C, which contained model instances that achieved the target range on the basic fitness metrics, as well as for HE(12) (Set A), HE(8) (Set B), and both HE(8) & HE(12) (Set C) fitness metrics, respectively (Figure 3.5). In Figure 3.7 we show overlaid scatter plots for three sets with set A in blue under set B in green under set C in red for each pair of conductance parameters. Starting first with the gross trends which were apparent upon inspection, we saw that neurite $\bar{g}_P$ was strongly limited in range in all three sets of model instances to a small window about the value used in the base model. When hand tuning our base model, we found that model activity was highly sensitive to neurite $\bar{g}_P$. When neurite $\bar{g}_P$ was too high, the model instance could not be sufficiently inhibited to terminate firing and when it was too low the model instance would rarely spike, let alone form bursts. Next, we found that neurite $\bar{g}_{K2}$ tended towards the lower portion of its allowable range, although the restriction was stronger in sets B and C than in set A. As we saw in (Figure 3.6), neurite $\bar{g}_{K2}$ could oppose the effect of neurite $\bar{g}_P$, and the influence of neurite $\bar{g}_{K2}$ on firing was generally opposite that of neurite $\bar{g}_P$, although our fitness metrics were less sensitive to perturbation of neurite $\bar{g}_{K2}$ than neurite $\bar{g}_P$. When $\bar{g}_{K2}$ was too large, the model instance ceased spiking and when it was small, the model instance's activity was not sculpted into identifiable bursts.

When we considered the axonal conductances, we found that the range of $\bar{g}_{Na}$ was somewhat limited. It could not be too small simply because model instances with very small values of $\bar{g}_{Na}$ could not produce spikes. The remaining axon conductances were not limited, but there was a tendency towards lower values for axon $\bar{g}_{K2}$ that is more obvious in Figure 3.12, Figure 3.13 and Figure 3.14. When we examined the electrical coupling in the synaptic compartment, which passed current between the two HE motor neurons in each ganglion, we found an interesting difference between the sets of model instances. In set A, the range of g_{Coup} did not appear to be restricted and there were model instances distributed across the full range of values, whereas in set B, and thus in set C as well, g_{Coup} was restricted to smaller values generally below the hand-tuned value. Larger values of g_{Coup} reduced the phase difference between the coupled neurons as also observed in previous work (Garcia et al., 2008, Wright and Calabrese, 2011b), consistent with the sensitivity results below, and the side-to-side phase difference between the targets for HE(12) motor neurons (0.33) was smaller than that for HE(8) motor neurons (0.48).

Next, we considered the interaction between parameters apparent upon inspection of the plots in Figure 3.7. First, neurite $\bar{g}_P$ and $\bar{g}_{K2}$ appeared to be correlated, which is consistent with what was evident when we inspected the currents in individual model instances in Figure 3.6. The slow wave components of I_P and I_{K2} opposed one another, which mostly mitigated the effects of one another on membrane voltage and excitability. However, even if they perfectly cancelled one another, which they did not, such increases in overall membrane conductance could result in partial shunting, reducing the size of spikes and synaptic inputs as they spread through the affected compartments.

Finally, we come to $\bar{g}_{KCa}$ and $\bar{g}_{CaS}$, which were only present in the neurite compartments. The distribution of model instances for $\bar{g}_{CaS}$ and $\bar{g}_{KCa}$ was a non-linear relationship that demonstrates a clear example of why a population approach is well suited to modeling neurons—an average parameter value would likely fall outside of the area of support, an example of a failure of averaging (Golowasch et al., 2002).

Figure 3.7 Effect of parameter interaction on fitness set

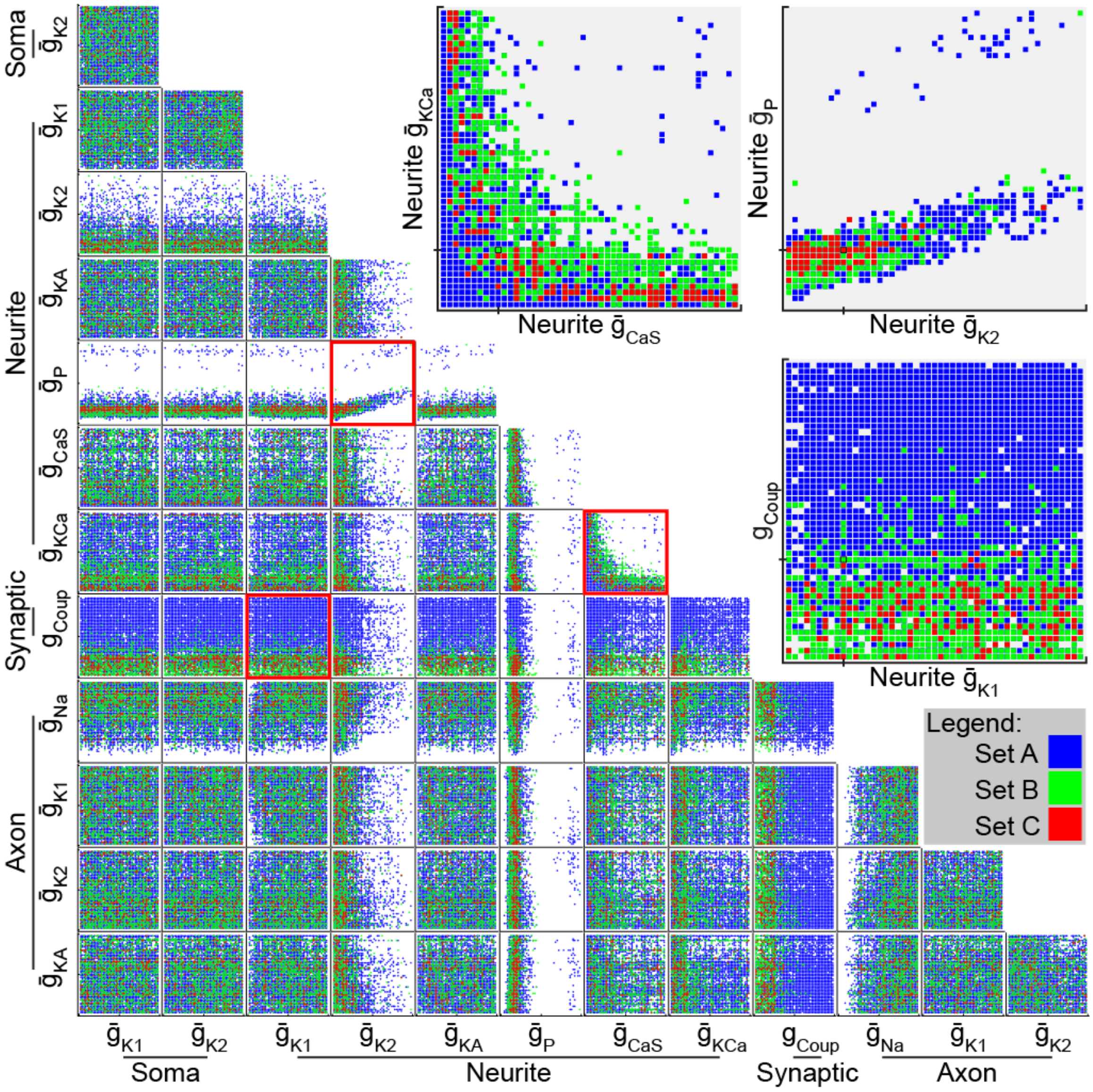

Figure 3.7 Effect of parameter interaction on fitness set

Functional model instances projected onto 2-D parameter space for each pair of parameters are shown for sets A (blue), B (green), and C (red). Each subplot is a layered scatter plot of set C over set B over set A of the parameter values of functional model instances for each pair of parameters. Each point may represent many models. Axes are from the minimum to maximum allowable value for the parameter indicated. No clear relationship between pairs of parameters was obvious upon inspection in most cases, but some did present interesting structures. The highlighted subplots show three particularly interesting relationships that are apparent upon inspection (shown as insets above right): $\bar{g}_{K2}$ appears correlated with $\bar{g}_P$ and is somewhat restricted in its distribution; $\bar{g}_{KCa}$ and $\bar{g}_{CaS}$ appear to form a non-linear relationship; and electrical coupling ($\bar{g}_{coup}$) is generally restricted to lower values in HE(8) motor neurons (set B) than in HE(12) motor neurons (set A). Black tick marks on the axes and boxes on highlighted subplots indicate the baseline model's parameter value.

Figure 3.8 Partial Correlation (ρ) matrix for a subset of parameters

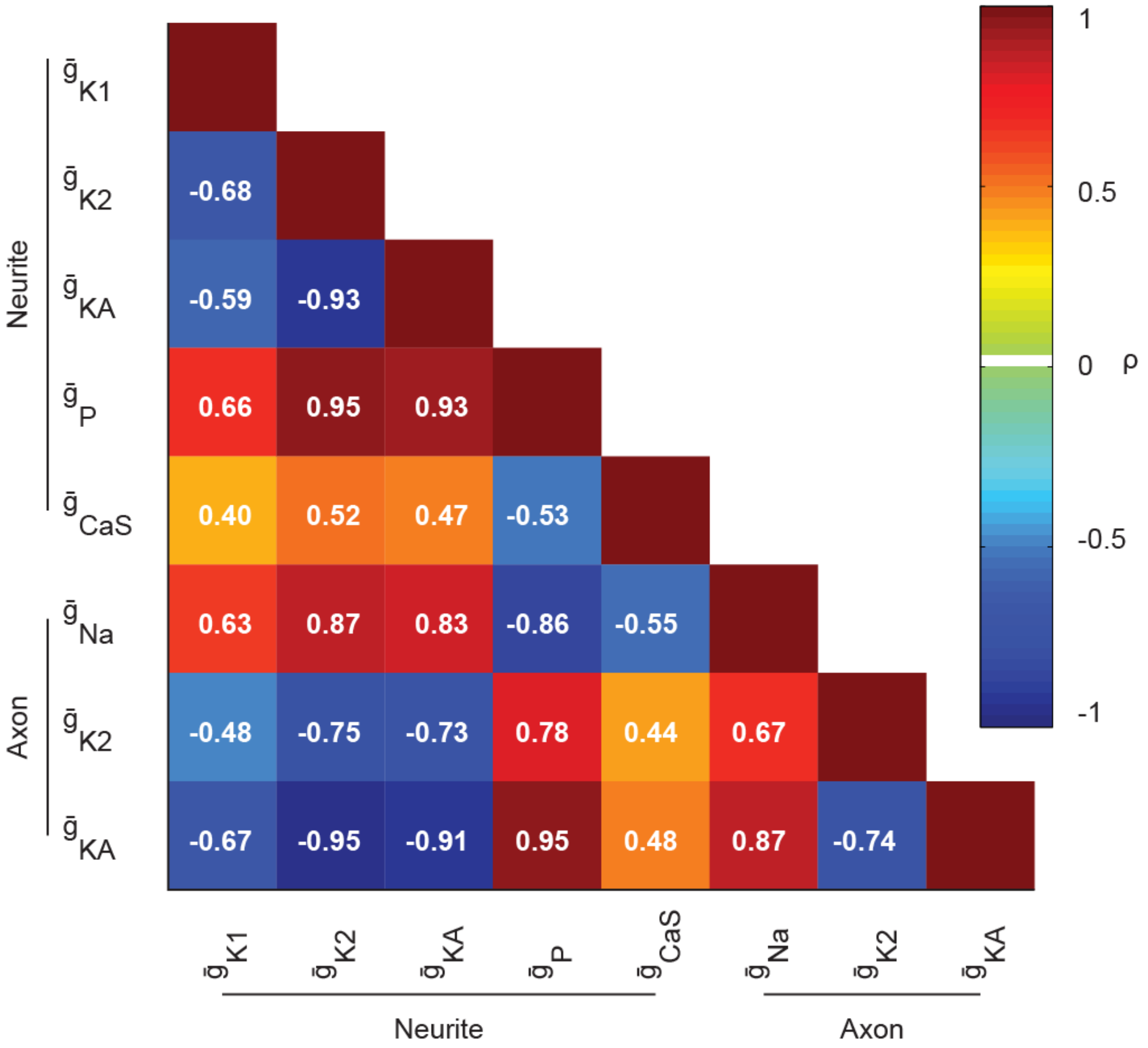

Figure 3.8 Partial Correlation (ρ) matrix for a subset of parameters

Warmer colors indicate positive and colder colors negative partial correlations. In general, pairs of conductances which oppose each other were positively correlated and pairs that could compensate for each other were negatively correlated. Numbers shown are calculated ρ. All partial correlation shown were significant ($p<0.00032$).

How are currents correlated?

The partial correlations, the correlations between parameters after compensating for the remaining parameters with a linear model, were then examined for set C. Figure 3.8 shows these partial correlations for a subset of parameters which were used in the final calculation because they had significant p values ($p<0.00032$). Neurite $\bar{g}_{K2}$ was correlated with neurite $\bar{g}_{p}$, as expected from our inspection of Figure 3.7, but neurite $\bar{g}_{KA,}$ axon $\bar{g}_{K2}$ and axon $\bar{g}_{KA}$ were also correlated with neurite $\bar{g}_{p}$, which was not clear in Figure 3.7, but the relationship between neurite $\bar{g}_{KA}$ and neurite $\bar{g}_{p}$ is illustrated by the currents shown in Figure 3.6. This correlation was somewhat unexpected because, unlike $\bar{g}_{P}$ and $\bar{g}_{K2}$, $\bar{g}_{KA}$ inactivates and is generally considered to be responsible for delaying spikes. However, we did observe a baseline window current during bursts, and to a lesser extent during inhibition, in the neurite compartments. The faster potassium current, neurite $\bar{g}_{K1}$, was also correlated with neurite $\bar{g}_{P}$, although this was far weaker and was not present for the axon $\bar{g}_{K1}$. Furthermore, there were similar, but weaker, correlations between neurite $\bar{g}_{K1}$, $\bar{g}_{K2}$, and $\bar{g}_{KA}$ with axon $\bar{g}_{Na}$ and even weaker with neurite $\bar{g}_{CaS}$. We see a similar pattern with the axon $\bar{g}_{K2}$, and $\bar{g}_{KA}$ correlated with $\bar{g}_{Na}$ as well as with neurite $\bar{g}_{CaS}$, although again the correlations with $\bar{g}_{CaS}$ were very weak. On the other hand, the outward neurite and axon $\bar{g}_{K2}$, $\bar{g}_{KA}$, and $\bar{g}_{K1}$ conductances were negatively correlated with one another, although these correlations were strongest between $\bar{g}_{K2}$ and $\bar{g}_{KA}$ for both axon and neurite. We see the same pattern with the inward currents, where $\bar{g}_{P}$ and $\bar{g}_{Na}$ and $\bar{g}_{CaS}$ were negatively correlated with one another, although the correlations with $\bar{g}_{CaS}$ were very weak. Thus the general pattern we observe is that the outward conductance parameters were positively correlated with the inward conductance parameters, whereas the inward conductances were negatively correlated with one another, and similarly the outward conductances were negatively correlated with one another. This pattern of partial correlations held for set A and set B (data not shown), but the partial correlation values were greatly diminished for those sets.

How did the parameters influence the fitness metrics?

To explore the influence of parameters on fitness metrics, we perturbed model instances by ± 25% and ± 50% for each neurite and axon parameter, plus coupling. As it was not feasible to simulate approximately 2 million perturbed model instances in sets A, B and C, we randomly selected 500 model instances each from sets A and B as described in Methods, in addition to all of set C. Only data for set C is shown in Figure 3.9 and Figure 3.10, but data were consistent across the subsets. Most of the results were consistent with our general expectation that increases in outward conductances should reduce spike frequency and reduce the duty cycle whereas the opposite should be the case for inward conductances. Manipulation of neurite $\bar{g}_{CaS}$, however, followed the pattern of outward conductances because an increase in $\bar{g}_{CaS}$ led to increased I_{KCa}. Spike frequency was most sensitive to perturbations of $\bar{g}_P$, consistent with our experience when hand tuning the initial model and with the observation that the range of $\bar{g}_P$ in good model instances is limited. Duty cycle followed the pattern observed with spike frequency, with increases in outward currents reducing the duty cycle and increases in inward currents increasing it.

We found some unexpected results when we considered the influence of maximal conductance density parameter perturbations on phase. In the peristaltic mode, an increase in neurite $\bar{g}_P$ resulted in a phase delay and a decrease in $\bar{g}_P$ resulted in a phase advance, and this was consistent for both HE(8)p and HE(12)p motor neurons (Figure 3.9). In the synchronous mode, however, we observed a phase advance for HE(12) and a phase delay for HE(8) as a result of reducing $\bar{g}_P$ and a minimal effect of increasing $\bar{g}_P$. This result was somewhat confounded by the many model instances which failed when $\bar{g}_P$ was reduced by 50% and the extreme excitability induced by increases in $\bar{g}_P$ requiring a reduction of the minimum interburst interval to isolate bursts, thus dropping some spikes. However, we found the corresponding reverse pattern when we examined the effect of perturbing neurite $\bar{g}_{KA}$ or neurite $\bar{g}_{K2}$, (Figure 3.10). In the peristaltic mode, a decrease in neurite $\bar{g}_{KA}$ or $\bar{g}_{K2}$ resulted in a small phase advance and an increase in these conductances resulted in a larger phase delay. In the synchronous mode, an increase in neurite $\bar{g}_{KA}$ or $\bar{g}_{K2}$ resulted in a phase delay in HE(8) and a phase advance in HE(12) motor neurons, consistently in opposition to what was observed for neurite $\bar{g}_P$. We also observed a difference between the influence of axon $\bar{g}_{KA}$ and neurite $\bar{g}_{KA}$. I_{KA}'s canonical role is to regulate spike frequency, primarily through being active after spikes before inactivating enough to allow another spike to be initiated. In the present model, we saw a result consistent with I_{KA}‘s canonical role when we increased the axon $\bar{g}_{Ka}$, where such an increase resulted in a decreased spike frequency. When we increased the neurite $\bar{g}_{KA,}$ however, we saw a smaller effect on spike frequency, as shown in Figure 3.10, but a greater influence on phase.

Figure 3.9 Phase, duty cycle and spike frequency sensitivity to neurite $\bar{g}_P$ parameter perturbation.

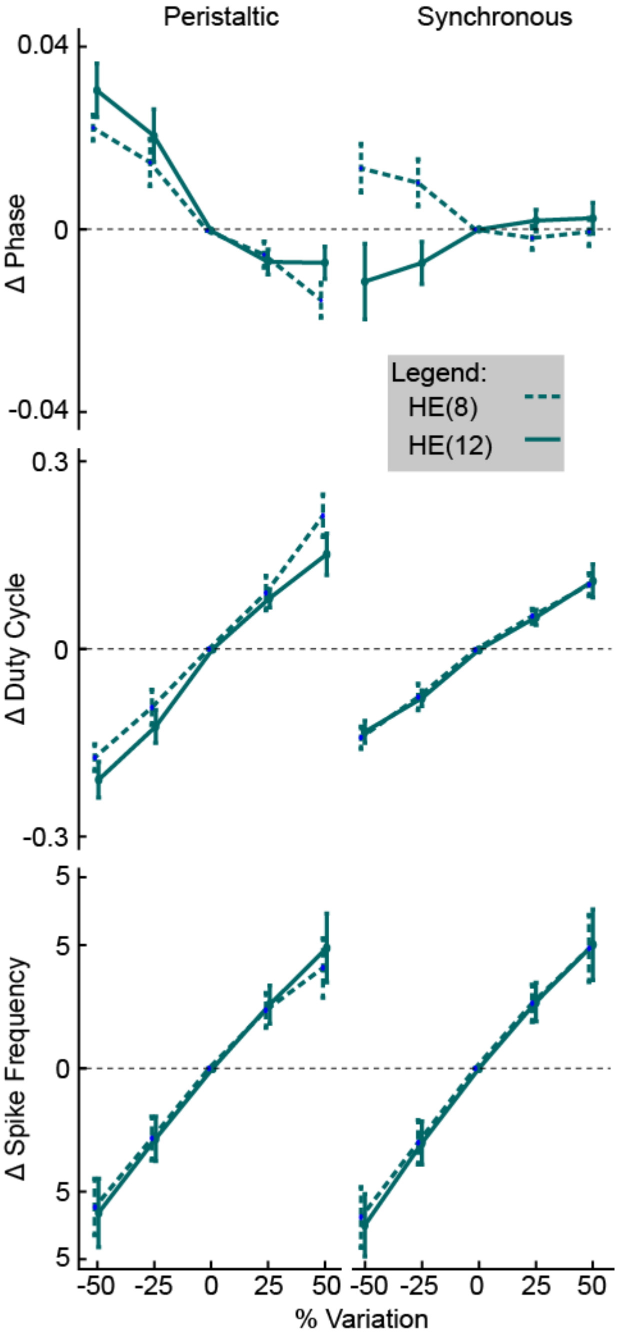

Figure 3.9 Phase, duty cycle and spike frequency sensitivity to neurite $\bar{g}P$ parameter perturbation.

Maximal conductance parameters were perturbed by ± 50% and 25% of their initial value for all model instances in set C. The resulting changes in phase, duty cycle and average spike frequency are plotted above for each mode of HE(8) and HE(12) motor neurons. Data shown as mean ± std.

Figure 3.10 Phase, duty cycle and spike frequency sensitivity to neurite $\bar{g}_{KA}$ and $\bar{g}_{K2}$ parameter perturbation

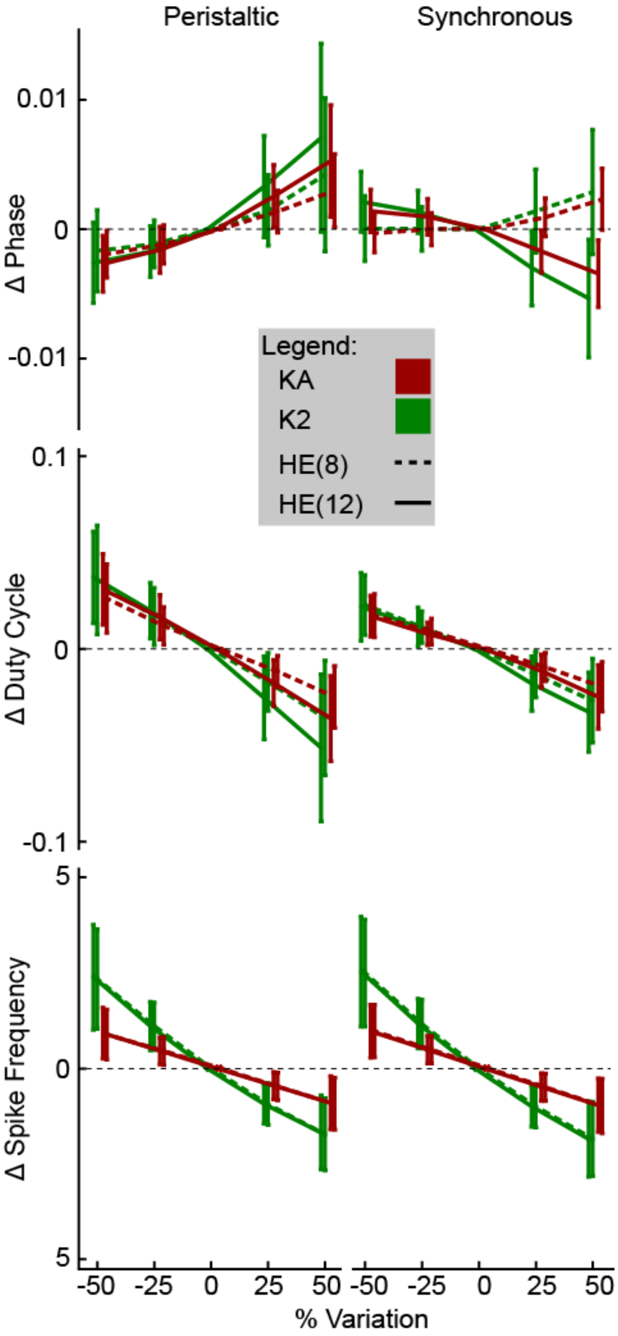

Figure 3.10 Phase, duty cycle and spike frequency sensitivity to neurite $\bar{g}_{KA}$ and $\bar{g}_{K2}$ parameter perturbation

Maximal conductance parameters were perturbed by ± 50% and 25% of their initial value for all model instances in set C. The resulting changes in phase, duty cycle and average spike frequency are plotted above for each mode of HE(8) and HE(12) motor neurons. Data shown as mean ± std.

How do the sets differ in response to current injection?

We then explored how the model instances differed between the sets A, B, and C with respect to their intrinsic properties. To do so, we used the same subsets as were used for parameter perturbations, subsets A, subset B and set C, and examined their activity during injections of hyperpolarizing current ramps that serve as a rough approximation of the inhibitory synaptic input. We measured the spike frequency vs. injected current and the time of the last spike during the down ramp and the first spike during the up ramp of triangular hyperpolarizing current. Even though the model instances produced a wide range of spike frequencies (from 5.78Hz to 14.37Hz, mean of 9.63Hz for set C), we observed that during the down ramp, when the hyperpolarizing current is increasing, the spike frequency was consistently lower than on the up ramp (see Figure 3.15), when the hyperpolarizing current was reducing. This was the case for all three subsets, but set C appeared more tightly constrained than subset A or subset B, having a lower spike frequency on the down ramp (weighted R2 and σ from the robust regression were: subset A down (0.639, 0.1367), subset B down (0.775, 0.1262), subset C down (0.865, 0.0884)). We then examined the last and first spikes relative to the trough of hyperpolarizing current to measure their excitability and ability to spike during hyperpolarization and recover from hyperpolarization due to current injection, and determine how the three groups differed; see Figure 3.11. The model instances from subsets A and B were more widely distributed, consistent with what was observed for the F/I relationships. When examined statistically, we found that there was a significant difference between sets in the last and first spike times ($F(6, 2782) = 624.171$, $p <$

0.0005; Pillai's trace = 1.148, partial η2 = 0.574). The set C model instances continued to fire longer than either subset A or B model instances (Bonferroni, p<0.0005), and subset B continued to fire longer than set A (Bonferroni, p<0.0005). On the up ramp, set C resumed spiking earlier than either set A or set B (Bonferroni, p<0.0005), but subset A and subset B did not differ significantly (p=0.111). These results suggest that the ability to fire early when inhibition is waning and to continue to fire later when inhibition is building make a model instance adaptable to different input patterns (e.g., HE(8) vs. HE12).

Figure 3.11 Last and first spike time during F/I ramp injection.

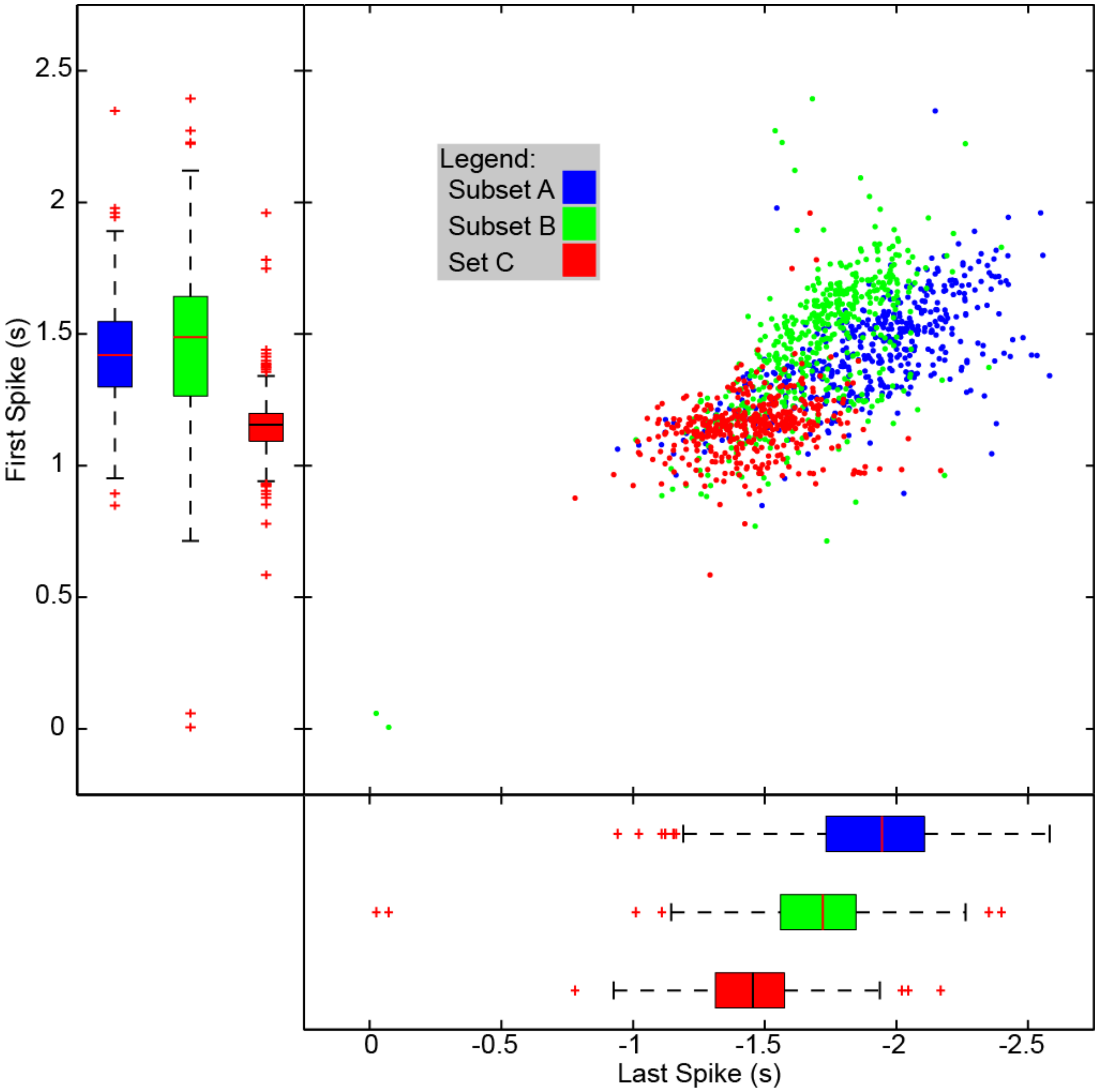

Figure 3.11 Last and first spike time during F/I ramp injection.

First spike vs. last spike relative to the peak hyperpolarizing current injection is shown as scatter and box plots for model instances from subsets A B and set C. Median, 75th and 25th percentile indicated by the center line and edges, respectively, for each box. Red crosses indicate outliers. Model instances were probed with a 5s triangular ramp current from 0 to -0.5nA and back to 0 injected into the soma compartment. There was a statistically significant difference in last and first spike time for the FI protocol based on set, $F(6, 2782) = 624.171$, $p < 0.0005$; Pillai's trace = 1.148, partial $\eta^2 = 0.574$. Post hoc tests (Bonferroni) showed a significant difference between set C and subset A ($p<0.0005$) as well as between set C and subset B ($p<0.0005$) for the first spike time, but not between subsets A and B ($p=0.111$). There was a significant difference between all sets/subsets for the last spike time ($p<0.0005$).

Discussion

The broader goal of our research was to understand how neuronal networks can generate coordinated motor patterns and thus coordinated movements, and, specifically, how the leech heartbeat central pattern generator coordinates segmentally repeated motor neurons into the fictive heartbeat motor pattern. Furthermore, we sought to understand better how the intrinsic properties of motor neuron contribute to this input-output transformation. The heartbeat CPG rhythmically inhibits the heart motor neurons, and previous research has shown that, although the majority of the motor neuron output pattern is dictated by this input from the CPG, the heart motor neurons are believed to contribute to pattern formation (Wright and Calabrese, 2011a, b). We thus set out to develop a heart motor neuron model that more fully captured the complexity of the living system than did previous models, and we successfully developed the first model of HE motor neurons that was capable of quantitatively achieving the target ranges on our fitness metrics, including the phasing observed in the living system.

To develop a more realistic heart motor neuron model, we first constructed a baseline hand-tuned multi-compartmental model and then used a multi-objective evolutionary algorithm to generate model instances (variations of this model) that had differing maximal conductance parameters, but all other properties of each model instance remained the same between instances. These model instances were evolved to achieve target ranges on fitness metrics which captured key output measures or electrophysiological characteristics recorded in the living system. In so doing, the algorithm produced model instances which were capable of quantitatively achieving appropriate target phases and soma membrane voltage waveforms that qualitatively resembled those recorded in the living system.

We focused on how the conductance densities contributed to the fitness of model instances because previous modeling studies implicated intrinsic membrane properties in motor neuron phasing (Garcia et al., 2008, Wright and Calabrese, 2011a, b). We found that strong partial correlations between many key conductance densities, in particular between neurite $\bar{g}_{KA}$, $\bar{g}_{K2}$, $\bar{g}_{P}$ and axon $\bar{g}_{KA}$, $\bar{g}_{K2}$, $\bar{g}_{Na}$. Parameters that had strong partial correlations, either positive or negative, appear to be linked by their influence on each of the fitness metrics we used to select good model instances. Conductances that opposed one another had the opposite effects on fitness metrics when perturbed while conductances that could compensate for one another had similar effects.

Selection of fitness metrics

We chose a restricted subset of possible fitness metrics – phase, duty cycle, average spike frequency, spike height, and slow-wave height – with which to evaluate our model and to evolve model instances. Phase and duty cycle are fundamental metrics when describing rhythmically active processes. Furthermore, phase and duty cycle, along with spike frequency, specify the output of these motor neurons–the timing, duration, and intensity of the activity that controls the heart muscle fibers they innervate. The average spike frequency, height, and slow-wave height are important metrics that capture the gestalt of heart motor neurons. In the living system, heart motor neurons are not only identified by their location and soma dimensions, but also by their characteristic activity: appropriately phased bursts of relatively small spikes with moderate spike frequency and a marked reduction in soma membrane voltage during inhibition. Thus, the metrics used in the present study represent the minimal complement necessary to accurately evaluate a heart motor neuron model.

Parameter correlation and regulation

When we examined the resulting model instances we found several interesting relationships between the maximal conductance parameters we allowed to vary in the evolutionary algorithm. Inward and outward currents that opposed one another were generally positively correlated, whereas those which could compensate for the loss of one another were negatively correlated. These relationships held across compartments. These results validate our intuition that conductances which are broadly in opposition, specifically the persistent inward sodium and the outward potassium conductances, could be ratiometrically increased (coregulated) without substantially altering activity. Conversely, outward currents which could partially compensate for one another were counter-regulated while broadly maintaining a characteristic output pattern. In our model, the inward and outward currents had positive partial correlations and thus we would expect them to be co-regulated in the living system provided that the proportions are considered as a larger group than individual pairs of conductances. On the other hand, many of the conductances we found to be correlated have very different dynamics, so it was somewhat surprising to see such strong positive and negative correlations until we considered their influence on the fitness metrics. For example, the target range allowed for phase is small, and achieving it appears to require a coordinated balance between parameters. If we consider a model instance slightly outside of the target range, then shifting into the target range would require coordinated changes to several parameters that individually and in combination shift the phase in the desired direction while not shifting the activity outside of the acceptable range on any other fitness metric. For many models, perturbations of individual parameters helped achieve one target while shifting away from another. Even though the allowable ranges for spike frequency and duty cycle were larger, as were the observed ranges for those metrics in the living system, these metrics are the most sensitive to parameter perturbation, so they could also be driving the observed correlations. The influence on spike frequency in particular appears to be related to the baseline current during the burst, and the conductances with larger baseline currents were more strongly correlated. The prediction that these conductances are correlated and that this is through their influence on the metrics we used to define the model instance sets is supported by a recent investigation in the pyloric CPG of the crustacean stomatogastric ganglion (Zhao and Golowasch, 2012). In that study, a dynamic clamp was used to vary three currents, I_A, I_h, and a compound current, I_{HTK}, and many of the activity attributes measured were influenced by all three currents investigated, with the influence of combinations reflecting compensatory effects between the currents.

One unexpected aspect of our results is that I_{KCa} appeared to be limited, either through low to moderate values of $\bar{g}_{CaS}$ or $\bar{g}_{KCa}$. This relationship is likely due to the interaction between $\bar{g}_{CaS}$ and $\bar{g}_{KCa}$ and their influences on the fitness of model instances. The direct effects of $\bar{g}_{CaS}$ were relatively small compared with $\bar{g}_{P}$, and $\bar{g}_{CaS}$ is not limited in range. Even though the direct effects of $\bar{g}_{CaS}$ were small, it is of critical importance because the accumulation of Ca^{2+} in each neurite compartment's calcium pool gates I_{KCa} which, if present at sufficient levels, has an adverse influence on our fitness metrics. I_{CaS} was linked to g_{KCa}'s calcium gate through a simple calcium pool model within each neurite compartment. High levels of both $\bar{g}_{KCa}$ and $\bar{g}_{CaS}$ resulted in a high level of I_{KCa}, which can prematurely terminate bursts, radically advance phase, reduce the duty cycle, and substantially reduce the spike frequency, all of which result in fitness values outside of the target range. When examined in our sensitivity analysis, increases in $\bar{g}_{KCa}$ advanced the phase whereas decreases delayed the phase, although the effect was small. The previous single compartmental model's synchronous phase was delayed relative to the living system (Garcia et al., 2008), so the phase advance resulting from I_{KCa} should have helped achieve the target synchronous phase. However, our results showed that I_{KCa} must be limited. Even so, I_{KCa} may help achieve the F/I results, as the down ramp of the injected hyperpolarizing current resulted in a lower spike frequency than the up ramp when the model instance resumes firing, although the dynamics of all the conductances in the neurite, axon and soma compartments will have to be carefully explored in future research to fully elucidate their relative contributions.

Another parameter which appeared to be tightly restricted is $\bar{g}_{P}$. The distribution of good model instances in parameter space and the extreme sensitivity of the fitness metrics to perturbation of $\bar{g}_{P}$ indicate that this conductance is important. This result is not surprising because neurite $\bar{g}_P$ drives the membrane voltage in the axon compartment, via its direct influence in the neurite compartments, into a range where spikes are initiated in the spike initiation zone in the neighboring axon compartment. The opposition of $\bar{g}_P$ by $\bar{g}_{KA}$ and $\bar{g}_{K2}$ appears to be a primary driving factor in the correlational relationships we found, and this relationship is likely due to the baseline currents in the neurite compartments.

In contrast to the previous heart motor neuron model, which predicted that a gradient of electrical coupling that increased towards the rear of the animal would be necessary to achieve the intersegmental phase relationships observed in the living system (Garcia et al., 2008, Wright and Calabrese, 2011a), we found that a coupling gradient is not necessary for proper pattern formation. Coupling conductance values in the range that supports sets B and C would work just as well for set A, so there was no requirement for a gradient. Furthermore, the coupling in sets B and C appeared to be constrained to the range observed in the living system. We did find that the coupling can influence phase by bringing the phases of the two heart motor neurons in each pair closer, but this effect was small. As such, an increasing gradient from the front to the rear of the animal could help achieve the progressively closer phases between the peristaltic and synchronous heart motor neurons, as predicted by prior modeling work, but our results do not indicate that this is required and thus it is unlikely to be a primary feature of heart motor neurons in the living system.

Neural Identity and the consequences of variability

In nervous systems with unambiguously identifiable neurons, such as the leech, in which we can often identify specific neurons by their physical attributes including location, size and morphology, but ultimately by their characteristic activity. We found that attributes of this characteristic activity, as measured by our fitness metrics, are influenced by the conductance densities we allowed to vary between model instances. When we perturbed individual parameters, although some of the fitness metrics might improve (i.e., move closer to their target value) others would move away from the target value. Such a perturbation would typically result in values outside of the target range on at least one metric. The maintenance of multiple attributes of characteristic activity, and thus neural type, requires coordinated changes to multiple conductances that oppose or can compensate for one another, manifesting as partial correlations in our analysis. In systems where the mRNA that codes for the ion channels that underlie membrane conductances has been measured, some correlations have been found to be neural-type specific. For example, in the STNS, the copy number of mRNA coding for hyperpolarization activated non-specific cation current (*IH*, I_h), a transient potassium current (*shal,* I_A), two delayed rectifier potassium currents (*Shaw* and *shab*, I_{Kd}), and a calcium sensitive potassium current (*BKKCa*, I_{KCa}) are correlated with one another in combinations and proportions specific to each neuron type (Schulz et al., 2007). Furthermore, IH and *shal* are significantly correlated with activity features such as phase mean interspike interval (Schulz et al., 2006, Schulz et al., 2007, Goaillard et al., 2009) and models of the STNS have shown that linear conductance correlations appear to help maintain such activity features as spike and burst phase, spike frequency and count, and other measures of neuronal type (Hudson and Prinz, 2010, Soofi et al., 2012). Even though such correlations can maintain activity features, the cellular cascades responsible are not necessarily dependent, as one might initially expect (MacLean et al., 2003, MacLean et al., 2005).

The input patterns and output targets we used were drawn from characteristic activity patterns under standard conditions. When other input patterns were used in small pilot evolutions, the small number of resulting model instances appeared to follow the same patterns observed in the present data set. The input pattern used here had a middle of the road HE(8)-HE(12) phase progression and was otherwise typical, so we do not believe our results would substantially change given a different input/output data set, but follow-up experiments will have to directly address this question.

In non-standard circumstances — such as the application of drugs, neuromodulation, or perturbation of other cellular parameters — the consequences of intrinsic parameter variability can come to the fore, manifesting as varying responses to perturbation. For example, temperature can affect membrane conductances differently (Hille, 2001). Simplistically, we can consider the case of two conductances which are strong, but oppose one another, and are exposed to a shift in temperature. If this shift differentially affects these conductances, then the activity pattern it produces can be radically altered or even terminated. For example, if $\bar{g}$P were to be influenced by modulation or temperature out of proportion to $\bar{g}$K2, then the result would tend toward extremes, either the cessation of spiking activity or spiking through periods of inhibition. Such a differential response to perturbation is exactly what is believed to underlie the results of recent investigations into the effect of temperature on the crustacean stomatogastric ganglion (Tang et al., 2012, Rinberg et al., 2013). The differential response of conductances to perturbation is also of concern when we consider the influence of neuromodulators or drugs. Neuromodulators and drugs influence subsets of conductances, but their effects on neural activity is influenced by the extant conductances (ion channels in the cellular membrane) in each neuron. As such, the intrinsic variability of intrinsic properties could lead neurons that appear similar to respond differently to these factors. Recent experimental work in the crab cardiac ganglion has shown disruption of conductances with pharmacological blockers results in differential response between cells, even within a single cell type in an individual animal, and a disruption of normal activity at the network level (Ransdell et al., 2013).

General conclusion

We developed the first model of heart motor neurons that was capable of producing a quantitatively accurate activity pattern and used it to elucidate relationships between parameters that are necessary to maintain the production of this activity pattern. No model will ever perfectly capture the entirety of what it represents–all models are, in some way, limited. In the case of models of neurons, we accept many reductions and simplifications in order to focus on the particular characteristics we are interested in–for example, we collapse regions of the neuron into isopotential compartments and approximate populations of discrete ion channels with Hodgkin-

Huxley style differential equation based models, to name just a few common reductions. Even so, we can produce models with striking predictive power that not only accurately represent specific neurons but also elucidate basic mechanisms controlling activity that apply to them and to neurons in general. In this paper, we have taken advantage of some of the unique characteristics of the leech heartbeat system as well as a population based modeling approach to further elucidate the electrophysiology of motor neurons. The model we have developed provides a large population of model instances with which to perform virtual experimentation, including those involving the manipulation of properties and parameters not experimentally accessible in the living system. Furthermore, the approach we have taken easily generalizes to other neuron types or even small neuronal networks.

Figure 3.12 Supplemental Parameter histogram for set A

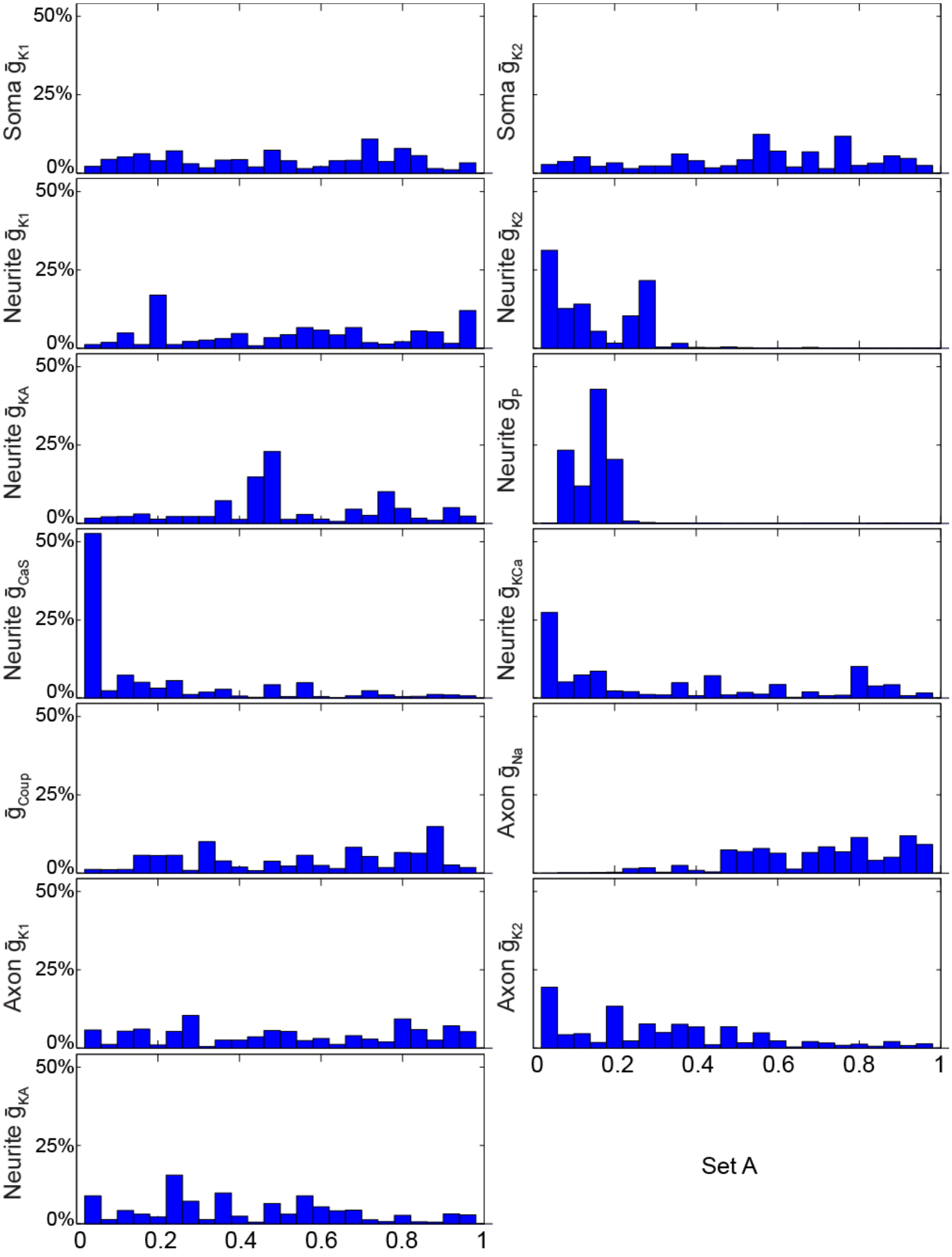

..

Figure 3.12 Supplemental Parameter histogram for set A

Counts are normalized to the total number of model instances in set A. Bin size is 0.04.

Figure 3.13 Supplemental Parameter histogram for set B

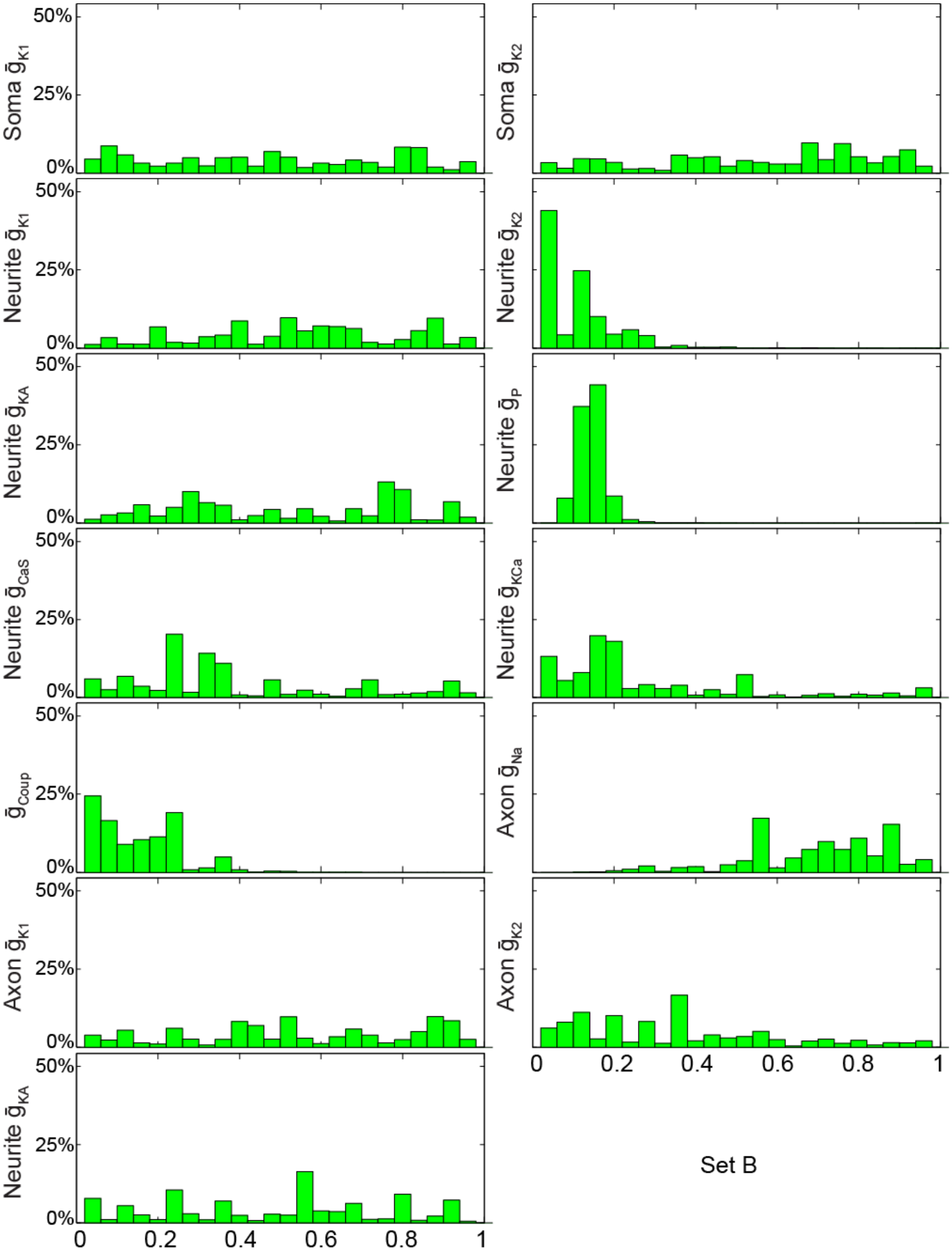

Figure 3.13 Supplemental Parameter histogram for set B

Counts are normalized to the total number of model instances in set B. Bin size is 0.04.

Figure 3.14 Supplemental Parameter histogram for set C

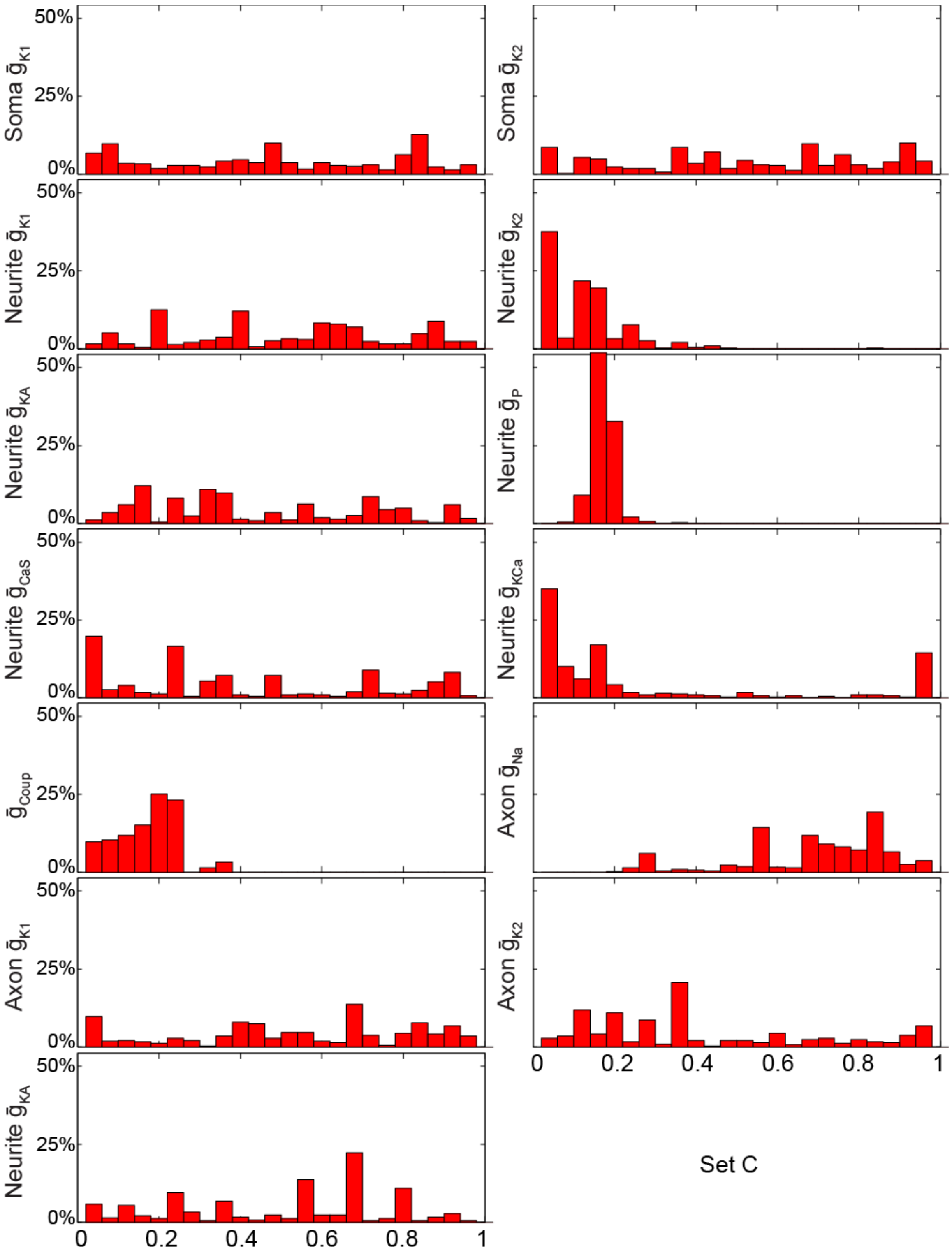

Figure 3.14 Supplemental Parameter histogram for set C

Counts are normalized to the total number of model instances in set C. Bin size is 0.04.

Figure 3.15 Supplemental Normalized spike frequency vs. injected current

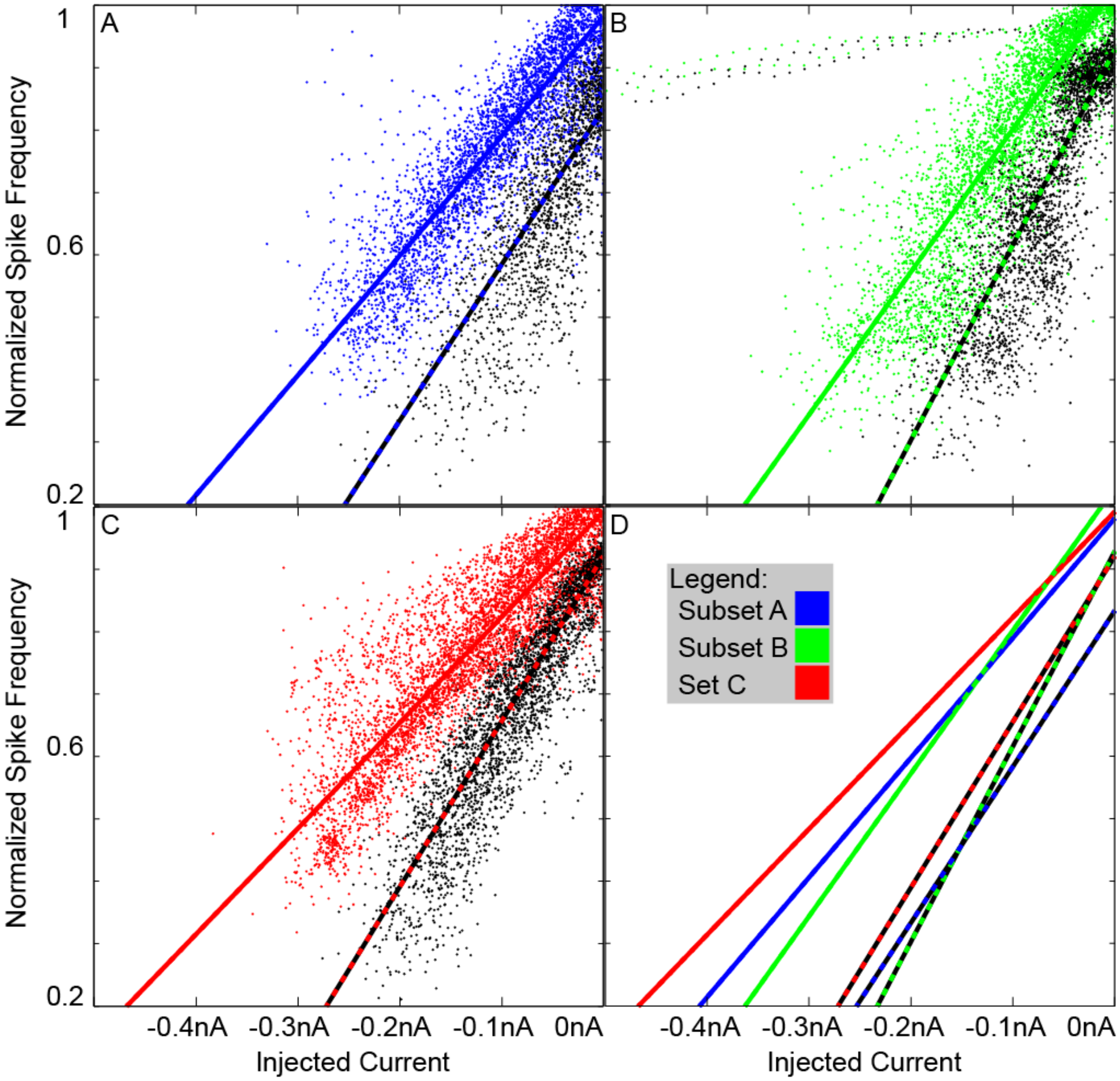

Figure 3.15 Supplemental Normalized spike frequency vs. injected current

Model instances in subset A, subset B, and set C were probed with a 5s triangular ramp current from 0 to -0.5nA and back to 0 injected into the soma compartment. Spike frequency is normalized to maximum spike frequency during ramp protocol. Panels A, B, C contain the data for subset A, subset B and set C, respectively. Black dots and the dashed regression lines represent spikes from the first half (downward portion) of the ramp and colored dots and solid regression lines represent spikes from the second half (upward portion). Panel C compares the regression lines from the three groups. Regression lines are calculated with robust least squares regression (bisquare weighting). Weighted R^2 and σ for the regression lines were: subset A downward (0.639, 0.1367), subset A upward (0.848, 0.0999), subset B downward (0.775, 0.1262), subset B upward (0.878, 0.0969), subset C downward (0.865, 0.0884), subset C upward (0.837, 0.0999).

Chapter 4: General discussion

The broader goal of this dissertation was to contribute to our research towards a deeper understanding of how neuronal networks can coordinate muscle activity, and specifically how the leech heartbeat central pattern generator controls coordinated constrictions of the hearts. Leech hearts are coordinated by heart motor neurons, which are superficially simple cells – they are tonically active in the absence of synaptic input from the heartbeat CPG and their bursts are sculpted by inhibitory input from the CPG. For such supposedly simple cells, constructing accurate models of their behavior turned out to be surprisingly difficult. While we know that the heartbeat CPG effects coordinated heart constrictions through the ensemble of 32 heart motor neurons, and although the majority of the motor neuron output pattern is dictated by the CPG, the intrinsic properties of a HE motor neuron appear to play a meaningful role in its input-output transformation (Wright and Calabrese, 2011a, b). Towards this end we constructed an updated model of HE motor neurons.

Why take the population approach?

The goal of neural modeling is to capture, as much as is both possible and necessary for the question at hand, the physiology of neurons., Since our best evidence indicates that a salient feature of biological neurons is underlying parameter variability (ion channel density, morphology, etc.), we should seek to capture variability in our models. The present model sought to achieve this through the use of a population of model instances that differed in their membrane conductance densities but were otherwise identical. Although this does increase the complexity of analysis and requires additional computation to generate these model instances, they became useful tools for conducting computational experiments. For example, our sensitivity analysis showed general trends, yet we also had counter examples which did not respond in a manner consistent with that trend. These instances can now be investigated in detail to ascertain the underlying reasons for why they responded as they did. The population approach also allowed us to consider how the parameters we allowed to vary might be related, or even regulated, to maintain proper function in the living system. Our results were generally consistent with our intuition, in that outward currents reduced excitability and inward currents enhanced it, but the extent to which conductances with substantially different dynamics were able to compensate for one another was surprising, as discussed more fully in chapter 3.

Future directions

With the new quantitatively accurate model of the HE motor neurons, experiments similar to those described in (Wright and Calabrese, 2011b) should be conducted with updated synaptic waveforms. In those previous experiments the model synaptic waveform was delivered to the soma of isolated pairs, but the resulting HE phasing did not match that observed in the recording from the living animal. Furthermore, we can use the dynamic clamp to inject the same model conductances used in the present HE model to validate the sensitivity predictions. The model was very sensitive to the I_P current, so it would make a good candidate. Preliminary experiments, both with the dynamic clamp and with an earlier set of model instances, investigated

I_{CaS}, as its dynamics suggest that it could have a meaningful influence on the phase of the burst. Those modeling experiments used an additional g_{CaS} that was uncoupled to the calcium shell, approximating what would result from the dynamic clamp, and found that increasing g_{CaS} advances the phase by increasing spike frequency towards the front of the burst. This is in disagreement with what we find when we examine the sensitivity analysis from the more recent experiments in which g_{CaS} was increased without decoupling the additional conductance from the calcium shell. The contradictory results are explained by the additional gating of g_{KCa} when g_{CaS} is increased. The present set of model instances provides a testbed for experiments, some of which can parallel work in the living system.

To make the next generation model

To develop the next generation of the HE motor neuron model, several approaches seem possible and could be implemented either in parallel or independently as there is little interdependency between them. For example, the model calcium sensitive potassium current (I_{KCa}) was constructed based upon limited data, so a more focused development and refinement is warranted. Additional electrophysiological experiments specifically targeted towards refining or replacing the present I_{KCa} model could allow for yet more accurate models of HE neurons. Furthermore, there is the added complexity of the calcium pool model that gates the I_{KCa} model in each compartment. The data used to define this pool was very limited, and this further complicates the accurate development of a model for I_{KCa}. Previous work in the lab used optical techniques to estimate and track calcium levels in HN interneurons, but not in the heart motor neurons. Using the improved optical sensors now available and applying them to HE motor neurons would produce data to more clearly define the calcium pool model. When calcium is replaced in the superfusate when measuring the spike frequency during a current injection ramp protocol, the spike frequency increases compared with the control, which is believed to be due to the lack of calcium gating of g_{KCa}. When the equivalent experiment was performed using the present model, the change in spike frequency was more modest and negligible in the case of models with minimal g_{KCa}, as one would expect. This further suggests that the g_{KCa} model can be improved to better capture the activation and calcium gate dynamics of the living system, the measurement of which will be challenging.

Our fitness metrics represent the minimal complement to analyze and define a model HE motor neuron. Most significantly missing is the spike frequency profile. A burst in the HE neurons in the living system starts at low frequency, ramps up to a higher frequency, and then back down to a low frequency near the end of the burst. Our model replicates some of this behavior, but not to the extent observed in the living system. Recent experimental data suggests that the spike frequency is important, and if the spike frequency is below a threshold the corresponding heart segment will not constrict. There are other metrics which could be applied, specifically those defining spike shape characteristics. For example, we did not measure (and thus did not constrain) the undershoot or spike width when developing our model, although we did consider them qualitatively while hand tuning the initial model instance. These spike shape characteristics may not be meaningful from the point of view of the hearts, additional metrics could certainly help construct a quantitatively better model. However, additional metrics would almost certainly require allowing additional parameters to vary, in particular the individual conductance parameters (Hendrickson et al., 2011b). As our conductance models were developed from voltage clamp data, which is prone to the space clamp problem, and were optimized and refined through single compartmental modeling, it is possible that some of their characteristics veered slightly off from that required for multicompartmental modeling. However, with the metrics we used the present model was successful, and it seems unlikely that our model was substantially off from what is necessary to better capture the features of the heart motor neurons of the living system.

We developed the present model directly as a compartmentally reduced model rather than attempting to construct a massive, detailed model and then reduce it to a more tractable number of compartments. The primary neurite and axon is a simple structure and our representation is the likely end result of such an approach. The many secondary neurites in the living system are collapsed into a single representative structure comprised of two compartments. Starting with a complex collection of secondary neurites would have required additional detail regarding the distribution of synapses with the HN interneurons as well as the electrical coupling with the contralateral HE motor neuron, but this is a tractable problem. We can easily differentially label the two HE motor neurons, as was done to determine the compartment dimensions used in the present model, and thus identify likely sites for electrical coupling

Better estimate of conductance distributions

We distributed the conductance densities based on our best estimates from electrophysiological data, but we did not have specific knowledge of the exact distribution. This is in many ways limited by the lack of an effective method to measure these distributions, however many innovative optical sensors have developed which would allow better estimates of the distribution of ion concentration changed during spikes. Novel approaches with optical [Na] sensors and protocols, such as those detailed in (Ross et al., 2013), for example, may provide more complete information regarding the distribution of fast and persistent sodium conductances. Furthermore, advances in optical [Ca] sensors have enabled higher precision measurements of calcium flux during individual spikes (Grewe et al., 2010), and this would help better estimate the distribution of calcium conductances in these cells.

The hearts

Each HE motor neuron innervates the ipsilateral heart in its own segment. The hearts themselves are excitable and are capable of endogenous constrictions in the absence of the excitatory input from the HE motor neurons (Maranto and Calabrese, 1984). This output pattern has a slower period and lacks the coordination of the pattern induced by the HE motor neurons. Thus, the functional heartbeat pattern is dictated by the input from the HE motor neurons and in that sense neurogenic. Even so, much as the motor neurons contribute in subtle, but meaningful ways to the pattern they produce, so too do the heart tubes. The experimental accessibility of the leech heartbeat system allows for simultaneous recording not only of the core CPG and the HE motor neurons simultaneously, but also of the heart tubes through a variety of modalities. The flow pattern had been imaged in whole, intact animals (Wenning et al., 2004, Wenning et al., 2011) and the constrictions had been recorded in reduced preparations with force transducers (Maranto and Calabrese, 1984), or even directly with electrodes (Maranto and Calabrese, 1984, Jellies and Kueh, 2012). Ongoing experiments using minimally dissected animals are now combining imaging (blood flow), force transducer (heart constrictions) and extracellular recordings (HE motor neurons) to build a more complete picture of how the heart tubes respond to HE motor neuron input, and ultimately how that relates to the activity of the core CPG. This presents a wonderful opportunity to investigate a behavior controlled by a CPG all the way from the neural basis to the actual behavior. Preliminary results suggest that the spike frequency of the HE motor neurons need to reach a yet to be determined threshold for the heart to constrict. It would be informative to examine the response of the muscle to artificially prolonged or foreshortened bursts to ascertain if the entire burst duration, at least that above the spike frequency threshold, matters, or if only an initial portion matters and the muscle at least partially escapes from neural control.

General Conclusions

The new model presented here has helped to elucidate how leech heart motor neurons produce their characteristic activity patterns. In particular, this model, the first of heart motor neurons that was capable of producing a quantitatively accurate activity pattern, showed that the balance between conductance parameters underlies the intrinsic properties of leech heart motor neurons. These maximal conductance parameter values were highly variable between model instances that were nevertheless capable of realizing a tightly constrained input-output transformation. The relationships between these parameter values, especially those between parameters which our data indicated were able to compensate for or oppose one another, maintain intrinsic properties that appear critical for the normal function of leech heart motor neurons. Although the specific tuning would likely differ between classes of motor neurons, this mechanism of tuning may well underlie the function of other motor neurons. Many lines of research are already underway to investigate attributes of leech heart motor neuron activity that this dissertation did not deeply explore, including the details of how the input patterns interact with the intrinsic properties and how the hearts themselves respond to the output patterns. Eventually, a top to bottom model of the entire leech heartbeat system, from interneurons through the muscle tissue itself, could be developed, enabling investigation of whole-system responses to various perturbations.

As is all but inevitable in research, we are left with many questions. Some are old and some new, and in the case of the latter many are more complicated than the ones we set out to answer. In this dissertation, we investigated a supposedly straightforward class of neurons and found that not only is their contribution to the coordination of their activity critical to normal function, but the putative mechanisms underlying that contribution is likely to play an important role in similar classes of neurons, if not neurons in general. Thus we have made progress towards a more refined understanding of the great complexity of the neural basis of behavior through an investigation of the simple, humble leech heart motor neuron.

Chapter 5: References

Achard P, De Schutter E (2006) Complex parameter landscape for a complex neuron model. PLoS computational biology 2:e94.

Angstadt JD, Calabrese RL (1991) Calcium currents and graded synaptic transmission between heart interneurons of the leech. The Journal of neuroscience : the official journal of the Society for Neuroscience 11:746-759.

Bernardo Perez-Etchegoyen C, Alvarez RJ, Rodriguez MJ, Szczupak L (2012) The activity of leech motoneurons during motor patterns is regulated by intrinsic properties and synaptic inputs. J Comp Physiol A Neuroethol Sens Neural Behav Physiol 198:239-251.

Bower JM, Beeman D, Wylde AM (1998) The book of GENESIS: exploring realistic neural models with the GEneral NEural SImulation System: Telos New York, NY.

Calabrese RL (1977) The neural control of alternate heartbeat coordination states in the leech, Hirudo medicinalis. Journal of comparative physiology 122:111-143.

Clarac F, Pearlstein E (2007) Invertebrate preparations and their contribution to neurobiology in the second half of the 20th century. Brain research reviews 54:113 - 161.

Crank J, Nicolson P (1947) A practical method for numerical evaluation of solutions of partial differential equations of the heat-conduction type. vol. 43, pp 50-67: Cambridge Univ Press.

Fisher RA (1924) The distribution of the partial correlation coefficient. Metron 3:329-332.

Garcia PS, Wright TM, Cunningham IR, Calabrese RL (2008) Using a model to assess the role of the spatiotemporal pattern of inhibitory input and intrasegmental electrical coupling in the intersegmental and side-to-side coordination of motor neurons by the leech heartbeat central pattern generator. J Neurophysiol 100:1354-1371.

Goaillard JM, Taylor AL, Schulz DJ, Marder E (2009) Functional consequences of animal-to-animal variation in circuit parameters. Nat Neurosci 12:1424-1430.

Golowasch J, Goldman MS, Abbott LF, Marder E (2002) Failure of averaging in the construction of a conductance-based neuron model. J Neurophysiol 87:1129-1131.

Gramoll S, Schmidt J, Calabrese R (1994) Switching in the activity state of an interneuron that controls coordination of the hearts in the medicinal leech (Hirudo medicinalis). The Journal of experimental biology 186:157 - 171.

Grashow R, Brookings T, Marder E (2009) Reliable neuromodulation from circuits with variable underlying structure. Proceedings of the National Academy of Sciences of the United States of America 106:11742-11746.

Grewe BF, Langer D, Kasper H, Kampa BM, Helmchen F (2010) High-speed in vivo calcium imaging reveals neuronal network activity with near-millisecond precision. Nat Meth 7:399-405.

Hendrickson EB, Edgerton JR, Jaeger D (2011a) The capabilities and limitations of conductance-based compartmental neuron models with reduced branched or unbranched morphologies and active dendrites. J Comput Neurosci 30:301-321.

Hendrickson EB, Edgerton JR, Jaeger D (2011b) The use of automated parameter searches to improve ion channel kinetics for neural modeling. J Comput Neurosci 31:329-346.

Hill A, Masino M, Calabrese R (2002) Model of intersegmental coordination in the leech heartbeat neuronal network. Journal of neurophysiology 87:1586 - 1602.

Hill A, Masino M, Calabrese R (2003) Intersegmental coordination of rhythmic motor patterns. Journal of neurophysiology 90:531 - 538.

Hille B (2001) Ion channels of excitable membranes. Sunderland, MA: Sinauer.

Hudson AE, Archila S, Prinz AA (2010) Identifiable cells in the crustacean stomatogastric ganglion. Physiology 25:311-318.

Hudson AE, Prinz AA (2010) Conductance ratios and cellular identity. PLoS computational biology 6:e1000838.

Ivanov AI, Calabrese RL (2000) Intracellular Ca2+ dynamics during spontaneous and evoked activity of leech heart interneurons: low-threshold Ca currents and graded synaptic transmission. The Journal of neuroscience : the official journal of the Society for Neuroscience 20:4930-4943.

Ivanov AI, Calabrese RL (2003) Modulation of spike-mediated synaptic transmission by presynaptic background Ca2+ in leech heart interneurons. The Journal of neuroscience : the official journal of the Society for Neuroscience 23:1206-1218.

Jellies J, Kueh D (2012) Centrally patterned rhythmic activity integrated by a peripheral circuit linking multiple oscillators. J Comp Physiol A Neuroethol Sens Neural Behav Physiol 198:567-582.

Kandarian B, Sethi J, Wu A, Baker M, Yazdani N, Kym E, Sanchez A, Edsall L, Gaasterland T, Macagno E (2012) The medicinal leech genome encodes 21 innexin genes: different combinations are expressed by identified central neurons. Development genes and evolution 222:29-44.

Kiehn O (2006) Locomotor circuits in the mammalian spinal cord. Annu Rev Neurosci 29:279-306.

Kiehn O (2011) Development and functional organization of spinal locomotor circuits. Curr Opin Neurobiol 21:100-109.

Kiehn O, Dougherty KJ, Hagglund M, Borgius L, Talpalar A, Restrepo CE (2010) Probing spinal circuits controlling walking in mammals. Biochemical and biophysical research communications 396:11-18.

Kiehn O, Kjaerulff O, Tresch MC, Harris-Warrick RM (2000) Contributions of intrinsic motor neuron properties to the production of rhythmic motor output in the mammalian spinal cord. Brain research bulletin 53:649-659.

Krahl B, Zerbst-Boroffka I (1983) Blood pressure in the leech Hirudo medicinalis. Journal of experimental biology 107:163-168.

Kristan W, Calabrese R, Friesen W (2005) Neuronal control of leech behavior. Progress in neurobiology 76:279 - 327.

Kuffler SN, J., Martin AR (1984) From Neuron to Brain. Sunderland, MA: Sinauer Associates.

Lamb D, Calabrese R (2011) Neural circuits controlling behavior and autonomic functions in medicinal leeches. Neural Systems & Circuits 1:13.

Lu J, Gramoll S, Schmidt J, Calabrese RL (1999) Motor pattern switching in the heartbeat pattern generator of the medicinal leech: membrane properties and lack of synaptic interaction in switch interneurons. J Comp Physiol A 184:311-324.

MacLean JN, Zhang Y, Goeritz ML, Casey R, Oliva R, Guckenheimer J, Harris-Warrick RM (2005) Activity-independent coregulation of IA and Ih in rhythmically active neurons. J Neurophysiol 94:3601-3617.

MacLean JN, Zhang Y, Johnson BR, Harris-Warrick RM (2003) Activity-independent homeostasis in rhythmically active neurons. Neuron 37:109-120.

Maranto AR, Calabrese RL (1984) Neural control of the hearts in the leech, Hirudo medicinalis. Journal of Comparative Physiology A 154:367-380.

Marder E (2011) Variability, compensation, and modulation in neurons and circuits. Proceedings of the National Academy of Sciences of the United States of America 108 Suppl 3:15542-15548.

Marder E, Bucher D, Schulz DJ, Taylor AL (2005) Invertebrate central pattern generation moves along. Current biology : CB 15:R685-699.

Marder E, Calabrese R (1996) Principles of rhythmic motor pattern generation. Physiological reviews 76:687 - 717.

Mullins OJ, Hackett JT, Buchanan JT, Friesen WO (2011) Neuronal control of swimming behavior: comparison of vertebrate and invertebrate model systems. Prog Neurobiol 93:244-269.

Norris BJ, Weaver AL, Morris LG, Wenning A, Garcia PA, Calabrese RL (2006) A central pattern generator producing alternative outputs: temporal pattern of premotor activity. J Neurophysiol 96:309-326.

Norris BJ, Weaver AL, Wenning A, Garcia PS, Calabrese RL (2007a) A central pattern generator producing alternative outputs: pattern, strength, and dynamics of premotor synaptic input to leech heart motor neurons. J Neurophysiol 98:2992-3005.

Norris BJ, Weaver AL, Wenning A, Garcia PS, Calabrese RL (2007b) A central pattern generator producing alternative outputs: phase relations of leech heart motor neurons with respect to premotor synaptic input. J Neurophysiol 98:2983-2991.

Norris BJ, Wenning A, Wright TM, Calabrese RL (2011) Constancy and variability in the output of a central pattern generator. The Journal of neuroscience : the official journal of the Society for Neuroscience 31:4663-4674.

Opdyke CA, Calabrese RL (1995) Outward currents in heart motor neurons of the medicinal leech. J Neurophysiol 74:2524-2537.

Prinz AA, Bucher D, Marder E (2004) Similar network activity from disparate circuit parameters. Nat Neurosci 7:1345-1352.

Ramirez JM (2011) The human pre-Botzinger complex identified. Brain : a journal of neurology 134:8-10.

Ransdell JL, Nair SS, Schulz DJ (2013) Neurons within the Same Network Independently Achieve Conserved Output by Differentially Balancing Variable Conductance

Magnitudes. The Journal of neuroscience : the official journal of the Society for Neuroscience 33:9950-9956.

Rinberg A, Taylor AL, Marder E (2013) The effects of temperature on the stability of a neuronal oscillator. PLoS computational biology 9:e1002857.

Roffman RC, Norris BJ, Calabrese RL (2012) Animal-to-animal variability of connection strength in the leech heartbeat central pattern generator. J Neurophysiol 107:1681-1693.

Ross W, Fleidervish I, Lasser-Ross N (2013) Imaging sodium in axons and dendrites. Cold Spring Harbor protocols 2013.

Sattelle DB, Buckingham SD (2006) Invertebrate studies and their ongoing contributions to neuroscience. Invertebrate neuroscience : IN 6:1-3.

Schulz DJ, Goaillard JM, Marder E (2006) Variable channel expression in identified single and electrically coupled neurons in different animals. Nat Neurosci 9:356-362.

Schulz DJ, Goaillard JM, Marder EE (2007) Quantitative expression profiling of identified neurons reveals cell-specific constraints on highly variable levels of gene expression. Proceedings of the National Academy of Sciences of the United States of America 104:13187-13191.

Smolinski TG, Prinz AA (2009a) Computational intelligence in modeling of biological neurons: A case study of an invertebrate pacemaker neuron. pp 2964-2970: IEEE.

Smolinski TG, Prinz AA (2009b) Multi-objective evolutionary algorithms for model neuron parameter value selection matching biological behavior under different simulation scenarios. BMC Neuroscience 10.

Smolinski TG, Prinz AA, Zurada JM (2008) Hybridization of rough sets and multi-objective evolutionary algorithms for classificatory signal decomposition. Rough computing: Theories, technologies, and applications 204-227.

Soofi W, Archila S, Prinz AA (2012) Co-variation of ionic conductances supports phase maintenance in stomatogastric neurons. J Comput Neurosci 33:77-95.

Tang LS, Taylor AL, Rinberg A, Marder E (2012) Robustness of a rhythmic circuit to short- and long-term temperature changes. The Journal of neuroscience : the official journal of the Society for Neuroscience 32:10075-10085.

Taylor AL, Goaillard JM, Marder E (2009) How multiple conductances determine electrophysiological properties in a multicompartment model. The Journal of neuroscience : the official journal of the Society for Neuroscience 29:5573-5586.

Thompson WJ, Stent GS (1976) Neuronal control of heartbeat in the medicinal leech. Journal of comparative physiology 111:309-333.

Tobin AE, Cruz-Bermudez ND, Marder E, Schulz DJ (2009) Correlations in ion channel mRNA in rhythmically active neurons. PloS one 4:e6742.

Tobin AE, Van Hooser SD, Calabrese RL (2006) Creation and reduction of a morphologically detailed model of a leech heart interneuron. J Neurophysiol 96:2107-2120.

Tolbert LP, Calabrese RL (1985) Anatomical analysis of contacts between identified neurons that control heartbeat in the leech Hirudo medicinalis. Cell and tissue research 242:257-267.

Tresch MC, Kiehn O (2000) Motor coordination without action potentials in the mammalian spinal cord. Nat Neurosci 3:593-599.

Vanier MC, Bower JM (1999) A comparative survey of automated parameter-search methods for compartmental neural models. J Comput Neurosci 7:149-171.

Weaver AL, Roffman RC, Norris BJ, Calabrese RL (2010) A role for compromise: synaptic inhibition and electrical coupling interact to control phasing in the leech heartbeat CpG. Front Behav Neurosci 4.

Wenning A, BJ N, RC S, RL C (2008) Two additional pairs of premotor heart interneurons in the leech heartbeat CPG: the more the merrier. Society for Neuroscience Annual Meeting.

Wenning A, Cymbalyuk G, Calabrese R (2004) Heartbeat control in leeches. I. Constriction pattern and neural modulation of blood pressure in intact animals. J Neurophysiol 91:382 - 396.

Wenning A, Norris BJ, Doloc-Mihu A, Calabrese RL (2011) Bringing up the rear: new premotor interneurons add regional complexity to a segmentally distributed motor pattern. J Neurophysiol 106:2201-2215.

Wright TM, Jr., Calabrese RL (2011a) Contribution of motoneuron intrinsic properties to fictive motor pattern generation. J Neurophysiol 106:538-553.

Wright TM, Jr., Calabrese RL (2011b) Patterns of presynaptic activity and synaptic strength interact to produce motor output. The Journal of neuroscience : the official journal of the Society for Neuroscience 31:17555-17571.

Zhao S, Golowasch J (2012) Ionic current correlations underlie the global tuning of large numbers of neuronal activity attributes. The Journal of neuroscience : the official journal of the Society for Neuroscience 32:13380-13388.